SymGF:
A Symbolic Tool for Quantum Transport Theory

Feng, Zi Min
Center for the Physics of Materials
Department of Physics
McGill University
Montreal, Quebec
2011

A Thesis submitted to the
Faculty of Graduate Studies and Research
in partial fulfillment of the requirements for the degree of
Doctor of Philosophy

CONTENTS

List of Figures

List of Tables

Abstract

In this thesis, I report the development and application of a symbolic derivation tool named “SymGF” - standing for Symbolic Green’s Function, that can automatically and analytically derive quantum transport expressions and the associated Keldysh nonequilibrium Green’s functions (NEGF). Quantum transport happens in open systems consisting of a scattering region coupled to external electrodes. When there are strong electron-electron interactions in the scattering region, analytical derivations of the Green’s functions can be very tedious and error prone[6]. Running on a personal computer, SymGF derives the necessary analytical formulas at a level of correlation specified by the user, using the equation of motion (EOM) method. The input to SymGF are the second quantized form the device Hamiltonian, the (anti)commutators of the operators that appear in the Hamiltonian, and a truncation rule for the correlators which determines the accuracy of the final outcome. The output of SymGF are the analytical expressions of transport properties such as electric current and conductance in terms of various Green’s functions; as well as the Green’s functions themselves in terms of the unperturbed non-interacting Green’s functions that can be obtained straightforwardly.

For systems where electron-electron interaction can be neglected, the transport problems can be easily solved and SymGF is not necessary - even though

SymGF gives the same answer; but for interacting systems SymGF drastically reduces the mathematical burden of analytical derivations. We have tested SymGF for several transport problems involving Kondo resonances where analytical derivations were done by humans: exactly the same results were obtained by SymGF but in a tiny fraction of time. We have applied SymGF to new and very hard problems that resist analytical derivations by hand, including quantum transport in a double quantum dot system[7]; transport through a single quantum dot in parallel to a direct lead-to-lead tunneling. Finally, at the post-analysis level, we have combined SymGF with an *ab initio* numerical modeling method to calculate quantum transport features involving atomistic degrees of freedom.

Résumé

Dans cette thèse, je présente le développement et les applications d'un outil de calcul symbolique connu sous le nom de "SymGF" (*Symbolic Green's Functions*) qui permet d'obtenir des expressions analytiques pour le transport quantique et les fonctions de Green de Keldysh pour les systèmes hors équilibre (FGHE). Le transport quantique survient dans les systèmes ouverts constitués d'une région diffusante couplée à des électrodes externes. Lorsque les interactions électrons-électrons sont importantes dans cette région, la dérivation analytique des fonctions de Green peut devenir fastidieuse et propice aux erreurs. Par contre, à l'aide d'un ordinateur personnel, la méthode SymGF permet d'obtenir rapidement les formules analytiques nécessaires, en utilisant les équations du mouvement (EOM) du système, à un niveau de corrélation spécifié par l'utilisateur. Les entrées nécessaires à la méthode SymGF sont l'Hamiltonien en seconde quantification du système, les relations d'anti-commutation des opérateurs impliqués et les règles de coupure pour les fonctions de corrélation, ce qui détermine la précision du résultat final. Les sorties sont les expressions analytiques des propriétés de transport tels que le courant électrique et la conductance en fonction des différentes fonctions de Green en plus de l'expression de ces dernières en fonction des fonctions de Green du système non perturbé et sans interactions, pouvant être calculées directement.

Pour les systèmes où les interactions électrons-électrons peuvent être négligés, le transport peut être étudié plus facilement et la méthode SymGF n'est plus nécessaire, même si elle reste toujours aussi juste. Par contre, pour les systèmes avec interactions, elle permet de réduire drastiquement les difficultés mathématiques reliées à la dérivation analytique. Nous l'avons testée pour plusieurs situations impliquant des résonances de Kondo, où les dérivations analytiques avaient déjà été effectuées, et les résultats furent reproduis parfaitement en une fraction du temps. Nous avons aussi appliqué cette méthode à de nouveaux problèmes très compliqués qui résistaient toujours au traitement analytique; tels le transport quantique dans un double point quantique et le transport dans un point quantique en parallèle avec une simple jonction tunnel. Finalement, en vue d'analyses futures, nous avons combiné la méthode SymGF avec un méthode de simulation numérique *ab initio* afin de calculer les caractéristiques du transport quantique impliquant des degrés de liberté atomiques.

Statement of Originality

In this thesis I presented the developement of SymGF, the symbolic tool for transport theory based on the Keldysgh NEGF method, as well as its applications to various physical problems. My contribution to this work include:

- The implementation of SymGF based on Mathematica[8], the function of which contains the automatic derivation of equations of motion (EOMs) and solving the EOMs.
- Proposing two new algorithms of solving EOMs, namely, the graph aided solution and the extension of Gaussian elimination of regular matrices to block matrices. They are both implemented in SymGF.
- Extension of the established binomial inverse theorem to multi-term situation, which is needed for the analytical inversion of matrices in a specified form. It is implemented in SymGF.
- Extension of the established Plemelj formula to multi-pole situation, which is needed for the analytical solution of self-energies. It is also implemented in SymGF.
- Application of SymGF to the T-shaped double quantum dot transport

system to a higher order[7]. I have obtained unprecedented formulas of this system. Terms relating to Kondo resonance are directly identified. This result has been compared to experiments and quantitative agreements are achieved.

Acknowledgments

I thank my supervisor Professor Hong Guo who introduced to me this exciting field and whose expertise has guided me throughout my entire graduate study. And I thank Dr. Sun QingFeng whose idea of preconditioned iteration helped with the production of new results from SymGF. I would also like to thank Dr. Liu DongPing, Dr. Ji Wei and Dr. Hu Yibin, whose constructive discussions with me helped with the extension of SymGF. I'm grateful to PHD candidates Zhang Xiangwen and Lei Tao for their constructive discussions about the algorithms regarding to Gaussian elimination of equation of motion set.

1

Introduction

For the past four decades, the development of electronic devices has followed the Moore's law which observes a steady decrease of device feature size by roughly a factor of two every eighteen months. According to the *International Technology Roadmap for Semiconductors* (ITRS), 11 nano-meter transistor would be achieved by 2016[9]. This relentless device miniaturization has brought physical systems into a new realm where quantum transport phenomena become very important.

Experimentally, people have been investigating many configurations in quantum transport systems. Specifically the quantum dot system, since their potential use as quantum computers, received a lot attention during the past few years [10, 11, 12, 13, 14, 15, 16, 17]. Refs.[10, 11, 12, 13, 14] did triple dots, Refs.[15, 16, 17] did double dots. All the dots are coupled and are interacting. By doing these very interesting experiments, we have the conductance curves as the results. Still, it requires further theoretical work to understand those curves, as the reasons behind the curves can't be explained just with numerical computations. For example, the Kondo effect[18] has a physical picture elaborated in Fig.4.3. To do theory, one needs to derive formulas for a certain model. When strong interaction or strong correlation is present, deriving the corresponding formulas can be extremely difficult. This difficulty has prevented theoretical investigations of transport problems to a high order where interesting physics like Kondo effect can be revealed. It is in the hope of being able to investigate high order processes that we developed the computer program that automatically derives the formulas for quantum transport problem. This program is also the main subject of this thesis.

Conventionally, quantum transport problems can be modeled with a lead-device-lead structure[19] shown in Fig.1.1. The current is assumed to flow from one lead to the other, through the central scattering region (device). The lead in the model is non-interacting since, in reality, leads are made of good conductors where electron-electron interactions are largely screened. The lead in the model is assumed to be connected to an infinitely large reservoir of electrons in equilibrium so that its statistics doesn't change with respect to any changes in the device scattering region. The lead can have its own electronic structure, and its electrochemical potential μ can be tuned by an applied potential bias. A prototypical scattering region (also referred as device, central device, central region etc.) can be modeled by a quantum dot that has its own electronic structure. The quantum dot can be non-interacting or interacting. One usually further assumes that the interaction on the quantum dot, if any, does not affect

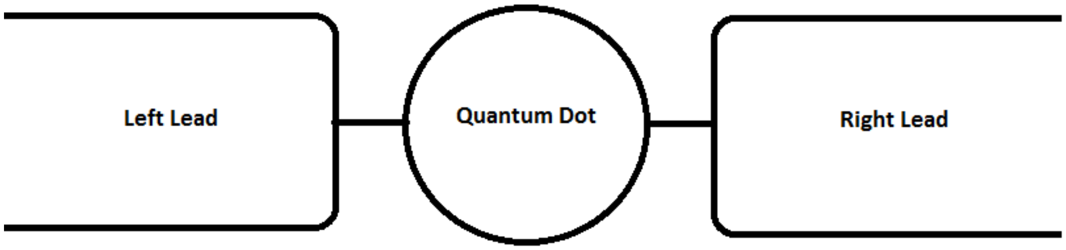

Figure 1.1: Schematic layout of a lead-device-lead system. A quantum dot is connected with two leads. The coupling between them is represented by a solid line.

the leads. Finally, in this model we have the coupling between the quantum dot and the leads. The coupling describes the probability amplitude of the electron hopping from the leads into the quantum dot and *vice versa*.

The transport system of Fig.1.1 can be described by the following general Hamiltonian:

$$\hat{H} = \sum_{\alpha k} \epsilon_{\alpha k} c^{\dagger}_{\alpha k} c_{\alpha k} + \sum_{n} \epsilon_n d^{\dagger}_n d_n + \sum_{mnlp} U_{mnlp} d^{\dagger}_m d^{\dagger}_n d_l d_p + \sum_{\alpha k n} t_{\alpha k n} c^{\dagger}_{\alpha k} d_n + h.c. \ , \tag{1.1}$$

where $c_{\alpha k}$ annihilates an electron in state k in lead-α, d_n annihilates an electron in state n in the quantunm dot, and $t_{\alpha k n}$ is the coupling constants. Since there is no observables corresponding to the operators $c_{\alpha k}$ and d_n, we don't write them as $\hat{c}_{\alpha k}$ or $\hat{d}_n$, to simplify our notation. An on-site interaction U_{mnlp} is assumed on the quantum dot, and this is the source of almost all the tedious and lengthy algebra. The central task of quantum transport theory is to solve for the electric current. The operator of current is defined as the rate of change of the total number of electrons of one of the leads (here we denote this lead as lead-α):

$$\hat{I}(t) = e\frac{d\hat{N}_\alpha}{dt} \tag{1.2}$$

where $\hat{N}_\alpha = \sum_k c^\dagger_{\alpha k} c_{\alpha k}$ is the number operator of the electrons in lead-α. The expectation of the current operator gives the current.

Theoretically, predicting nonlinear and nonequilibrium quantum transport properties of various nanostructures is a serious challenge, especially if strong electron-electron interaction is taken into account. There are two major ways to solve for electric current described by the Hamiltonian Eq.(1.1). One is the scattering matrix theory formalism (SMT)[20, 21] and the other the Keldysh nonequilibrium Green's function (NEGF) formalism[22]. SMT is more phenomenogical while NEGF is essentially exact except the adiabatic approximation that it used as its foundation. Both methods have been applied very successfully to a wide scope of problems in quantum transport problems[23]. SMT is usually applied to problems without interaction. Meanwhile, rich physics found in quantum dots such as spin blockade, Coulomb blockade and Kondo effect, etc., all hinge upon interactions between electrons. Also, due to the usually small number of electrons confined in a quantum dot, the interactions are usually strong and this prevents mean-field theory (MFT) from giving accurate results. Since NEGF is naturally applied in many-body physics, it is the method of choice in many theoretical works. In fact, it might be the most popular and powerful theoretical method. In the past decade, NEGF has also been combined with material theory such as the density functional theory (DFT), for quantitative and parameter-free calculations of nonequilibrium quantum transport in realistic nanoelectronic devices[24, 25, 26, 27].

In a NEGF analysis of transport in nanostructures, one starts from the second quantized form of the device Hamiltonian like Eq.(1.1) which is usually partitioned into terms corresponding to the central device, the device leads and the coupling between the scattering region and the leads[23]. The interactions can be included inside the device scattering region. The analysis proceeds by deriving various Green's functions from the Hamiltonian which are needed for calculating the transport properties such as the conductance, electric current and DOS. While NEGF has been widely used in the community of quantum transport theory, it can be a tedious mathematical procedure to derive the necessary Green's functions for interacting systems[23]. It would be useful if such procedure can be carried out symbolically by a computer. While tremendously successful in sub-atomic physics[28], symbolic computation in solid state physics is far less developed. A reason, perhaps, is due to the much wider range of problems (the Hamiltonian) each having its own solution method/approximation in solid state physics. Nevertheless, for quantum transport theory using NEGF, we believe it is possible to develop a symbolic technique that can be applied to solve difficult problems. It is the purpose of this thesis to develop it and apply it to some hard problems.

Our symbolic tool, called SymGF (standing for symbolic Green's functions), is developed with Mathematica[8]. There are three sets of input to SymGF: (i) the second quantized form of the device Hamiltonian, (ii) the commutators of the creation and annihilation operators, and (iii) the truncation rules for the correlators. Here, (ii) is necessary because SymGF needs to know whether the particles are Fermions or Bosons and if the various creation and annihilation operators belong to the same Hilbert space. Concerning (iii): SymGF uses the equation of motion (EOM) method[23, 29, 30, 31] to iteratively solve the Green's function, therefore for interacting systems (short range interaction model, where the on-site interaction does not affect the electronic structure of the leads or any other quantum dots) one needs to tell SymGF how to truncate the higher order correlators in order to close the set of EOMs[32]. With these three sets of inputs, SymGF symbolically derives the formula for current, conductance and various Green's functions in terms of the unperturbed Green's functions of the device scattering region. It also identifies expressions of the self-energy due to device leads. Afterward, numerical results and plots are obtained for the transport properties by evaluating the symbolic formula derived by SymGF.

For non-interacting systems in steady-state transport, one can easily derive the NEGF by hand and, of course, SymGF obtains exactly the same results. For interacting systems where there is no exact solution, we have tested SymGF on many problems by comparing its derived analytical expressions with published literature[33, 34, 35, 36, 37] and, again, exactly the same results were obtained. The power of SymGF is evident: for the rather complicated problem of Kondo resonance in a magnetic tunnel junction[33], SymGF derives all the Green's functions *analytically* in less than a minute on a desktop personal computer.

The rest of the thesis is organized as follows.

Chapter 2 reviews the derivation of current formula. Then we show how one can solve transport problems with equation of motion (EOM). Examples include a simple transport problem with non-interacting single quantum dot and a problem with an interacting single quantum dot as the central device.

Chapter 3 presents the development of SymGF. We start with the scope of this tool, then we elaborate on the algorithms SymGF uses. And after that we present some technical details that deals with the self-energies. A few problems where manual derivation is easy are presented in the end, as verifications of SymGF. Obviously SymGF has passed all these tests as it gave the identical results.

Chapter 4 presents the first real problem SymGF has solved - the double quantum dot transport problem at Kondo level. Results at this level is qualitatively different from results at Hartree-Fock level. With the formulas SymGF derived, we can directly check which term(s) contribute to the Kondo effect that aroused in the system. We also show that with appropriately chosen parameters, its numerical results is comparable to the experiments.

Chapter 5 presents the results for the interacting single quantum dot transport system with direct lead-lead contact. Results of both low and high order are shown, and we again see qualitative difference between them.

In **Chapter 6**, we seek the possibility of using SymGF to *ab initio* calculations with the example of NanoDCal[27].

In **Chapter 7** we briefly summarize this thesis.

Finally in the **Appendices** we present the formulas involved in various derivations presented in the main text.

2

Quantum Transport Theory with Non-Equilibrium Green's Function

In this chapter, we develop the basic formulation of quantum transport theory within the nonequilibrium Green's function (NEGF) formalism following the well documented theoretical approach of Ref.[23]. We start by deriving the formula for electric current in terms of various NEGFs. Two different device models will be considered. The first is that shown in Fig.1.1 that the two leads are separated by the quantum dot and have no direct contact. The second is where the two leads have a direct transport link connecting them (see Fig.2.1). Since these derivations are standard NEGF manipulations well documented in the literature[23], we shall only illustrate the main steps and refer interested readers to the original papers. We then illustrate the theoretical procedure by solving two very simple transport problems using the equation of motion (EOM) method.

2.1 Current Formula without Direct Lead-Lead Contact

Given the Hamiltonian Eq.(1.1) and the definition of the electric current Eq.(1.2), we proceed to deriving the current formula using the Heisenberg equation of motion method:

$$\frac{d\hat{N}_\alpha}{dt} = -i[\hat{N}_\alpha, \hat{H}] = -i\sum_{\alpha k} t_{\alpha k n} c^\dagger_{\alpha k} d_n + h.c.$$

where we have set $\hbar = 1$ for simplicity of notations. Then the current $I(t)$ is obtained by applying the current operator $\hat{I}(t)$ in Eq.(1.2) to the ground state of the total system governed by $\hat{H}$,

$$I(t) = -e\sum_{kn} t_{\alpha k n} G^<_{n,\alpha k}(t,t) + h.c. \qquad (2.1)$$

where we have defined the lesser Green's function

$$G^<_{n,\alpha k}(t,t') \equiv i\langle c^\dagger_{\alpha k}(t') d_n(t)\rangle.$$

and in Eq.(2.1) both time in $G^<_{n,\alpha k}(t_1,t_2)$ are at t ($t_1 = t_2 = t$). The corresponding time-ordered Green's function $G^t_{n,\alpha k}(t,t')$ can be written as

$$G^t_{n,\alpha k}(t,t') = \theta(t-t')G^>_{n,\alpha k}(t,t') + \theta(t'-t)G^<_{n,\alpha k}(t,t') \qquad (2.2)$$

where $G^>_{n,\alpha k}(t,t') = -i\langle c^\dagger_{\alpha k}(t') d_n(t)\rangle$. One of the conceptual tool that NEGF formulism uses to define the initial/final state is the complex time contour, where time comes from $-\infty$ to present, and when physical processes finish, goes back to $-\infty$[23]. It has been shown that Green's function defined on the complex time contours are formally the same as Green's functions defined on real time axis[23], which means replacing t (on real time axis) with τ (on time contour), we obtain the expression for nonequilibrium current. Furthermore, with EOM method it has been shown that[23]

$$G^t_{n,\alpha k}(\tau,\tau') = -i\langle T_c[d_n(\tau)c^\dagger_{\alpha k}(\tau')]\rangle = \sum_m \int d\tau_1 G_{nm}(\tau,\tau_1)t^*_{\alpha k m} g_{\alpha k}(\tau_1,\tau')$$

where the superscript t means it is a time-ordered Green's function and T_c represents the time ordering operator on the time contour and the integration of τ_1 is over the entire contour, and

$$\begin{aligned} G_{nm}(\tau,\tau') &= -i\langle T_c[d_n(\tau)d^\dagger_m(\tau')]\rangle \\ g_{\alpha k}(\tau,\tau') &= -i\langle T_c[c_{\alpha k}(\tau)c^\dagger_{\alpha k}(\tau')]\rangle. \end{aligned}$$

In order to do actual practical calculations, one usually transforms the integration over the complex time contour into an integration over real time axis, by using the analytical continuation theorem[23]. The result is:

$$G^<_{n,\alpha k}(t,t') = \sum_m \int dt_1 \left(G^r_{nm}(t,t_1)t^*_{\alpha k m} g^<_{\alpha k}(t_1,t') + G^<_{nm}(t,t_1)t^*_{\alpha k m} g^a_{\alpha k}(t_1,t')\right)$$

where superscript r and a indicates the retarded and advanced Green's function, respectively.

For steady state transport problems which is the concern of this thesis, only the difference in time, $t-t'$, appears in the formulation. Namely the two-time dependence of all the Green's functions $G(t,t')$ becomes $G(t-t')$. Therefore it is easier to work in the Fourier space by transforming $G(t-t') \to G(\omega)$.

Substituting the Fourier transformed $G^{<}_{n,\alpha k}(\omega)$ back into Eq.(2.1), we obtain

$$I_\alpha = -e \int \frac{d\omega}{2\pi} \operatorname{Tr}\left[(G^r(\omega) - G^a(\omega))\Sigma^{<}_\alpha(\omega) + G^{<}(\omega)\left(\Sigma^a_\alpha(\omega) - \Sigma^r_\alpha(\omega)\right)\right] \tag{2.3}$$

where we have defined the self-energies of the lead labeled by α as

$$\Sigma^x_{\alpha,mn}(t_1 - t_2) = \sum_k t^*_{k\alpha m} g^x_{k\alpha}(t_1 - t_2) t_{k\alpha n}$$

and their Fourier transform as:

$$\Sigma^x_{\alpha,mn}(t_1 - t_2) \to \Sigma^x_{\alpha,mn}(\omega)\ .$$

In this way, Eq.(2.3) gives the steady-state electric current flowing in lead-α. Since it does not contain convolution, it is computationally more favorable. This formula is valid as long as the two leads connect to the central scattering region and nothing else; it is not valid if the leads also connects to anything else, for example the case where left and right leads have direct coupling (see next section or Chapter 5).

When the external bias voltage is small, we expect a linear response from the system. In this case, we are more interested in calculating the conductance which can be obtained by the derivative of current with respect to the bias. The result is[38]:

$$G = \frac{e^2}{h} \int f'(\omega) \frac{2\Gamma_L(\omega)\Gamma_R(\omega)}{\Gamma_L(\omega) + \Gamma_R(\omega)} \operatorname{Im}[G^r(\omega)] \tag{2.4}$$

where Γ_α is the linewidth function of lead-α, defined as

$$\Gamma_\alpha \equiv \Sigma^r_\alpha(\omega) - \Sigma^a_\alpha(\omega)\ .$$

Since Eq.(2.4) comes from the current formula Eq.(2.3), they both have the same range of validity.

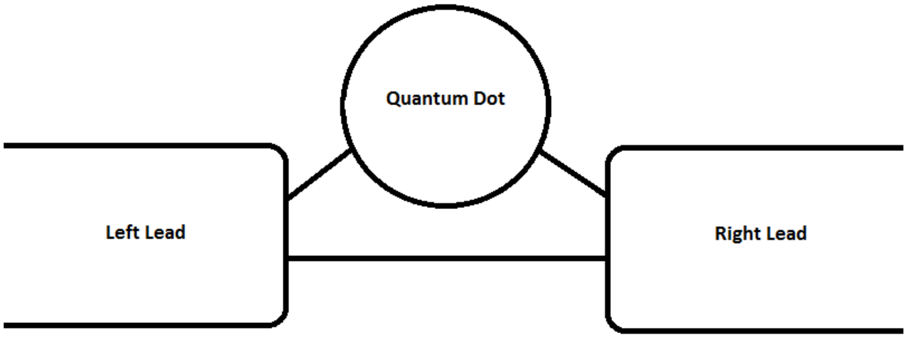

Figure 2.1: Schmetic layout of the transport system with direct lead-lead contact. A quantum dot is coupled to two leads, while there is also direct coupling between the two leads. Couplings are represented by a solid line.

2.2 Current Formula with Direct Lead-Lead Contact

The lead-device-lead model of Fig.1.1 is the most studied system, but there are more device structures being fabricated and investigated in recently years. For instance, there could be a direct contact between the two leads in parallel to the link through the quantum dot: the current formula changes as a result. Such situations occur in recent experiments where tunneling from a STM tip to a molecular quantum dot assembled on a substrate, is accompanied by direct tunneling from the same STM tip to the substrate[39, 40], like what's shown in Fig.2.1. The derivation of the current formula for the device model of Fig.2.1 is somewhat complicated and we put the details in the Appendix. Here we just present the results.

Let's consider the device model of Fig.2.1 where the quantum dot has a single non-degenerate energy level ϵ_σ, where σ indicates the spin. The system can be described by the following Hamiltonian:

$$\begin{aligned}\hat{H} = \sum_{\sigma} \epsilon\sigma d_\sigma^\dagger d_\sigma + U d_\uparrow^\dagger d_\uparrow d_\downarrow^\dagger d_\downarrow + \sum_{\alpha\sigma k} \epsilon_{\alpha\sigma k} c_{\alpha\sigma k}^\dagger c_{\alpha\sigma k} + \\ \left(\sum_{\alpha\sigma k} t_{\alpha k} c_{\alpha\sigma k}^\dagger d_\sigma + h.c\right) + \left(\sum_{\sigma k_1 k_2} v_{k_1 k_2} c_{L\sigma k_1}^\dagger c_{R\sigma k_2} + h.c.\right) \quad , \end{aligned} \tag{2.5}$$

where $d_\sigma^\dagger$ and d_σ are operators of the central dot. With the direct transport link between the two leads (see Fig.2.1), we write down the lead-lead coupling term $\sum_{\sigma k_1 k_2} v_{k_1 k_2} c_{L\sigma k_1}^\dagger c_{R\sigma k_2} + h.c.$. This extra link changes transport significantly and the current formula is different from Eq.(2.3) as expected.

To derive a new current formula for the device model of Fig.2.1, we define the number operator of the electrons with spin labeled by σ in the left lead as $\hat{N}_{L\sigma} = \sum_k c_{L\sigma k}^\dagger c_{L\sigma k}$. The current is then:

$$\hat{I}_\sigma = e\frac{d\hat{N}_{L\sigma}}{dt} \ . \tag{2.6}$$

Using the Heisenberg equation of motion to calculate the right hand side of Eq.(2.6) following a similar procedure as that in the last section, we obtain (with details summarized in Appendix A):

$$\begin{aligned}
I = & -e\int \frac{d\omega}{2\pi}\sum_{k_1k_2} v_{k_1k_2}G^{<}_{\sigma k_1k_2} + h.c \\
& -e\int \frac{d\omega}{2\pi}\sum_{k} t_{Lk}G^{<}_{L\sigma k} + h.c \\
= & -e\Bigg(\int \frac{d\omega}{2\pi}\Big(\sum_{k_1k'}\big(G^{r}_{R\sigma k_1k'}\Sigma^{<}_{k_1k'} + G^{<}_{R\sigma k_1k'}\Sigma^{a}_{k_1k'}\big) + \\
& \sum_{k_1}\big(G^{r}_{R\sigma k_1}\Sigma^{<}_{Lv\sigma k_1} + G^{<}_{R\sigma k_1}\Sigma^{a}_{Lv\sigma k_1}\big)\Big)\Bigg) + h.c \\
& -e\int \frac{d\omega}{2\pi}\sum_{k} t_{Lk}G^{<}_{L\sigma k} + h.c\ . \qquad (2.7)
\end{aligned}$$

There are five different Green's functions in the above expression and we need to evaluate them one by one.

First, we evaluate the third term of Eq.(2.7) $\sum_k G^{r}_{R\sigma k}\Sigma^{<}_{Lv\sigma k}$. As shown in Appendix A (Eq.(8.26)), it is

$$\begin{aligned}
\sum_k G^{r}_{R\sigma k}\Sigma^{<}_{Lv\sigma k} = & \sum_k 2\pi i G^{r}_{R\sigma k} f_L(\omega) v_{\omega,k} t^{*}_{L\omega} \\
= & \ 2\pi i f_L(\omega) t^{*}_{L\omega} G^{r}_{\sigma} \times \sum_k \Bigg(- i\pi t_{L\omega} v^{*}_{\omega,k} g^{r}_{R\sigma k} v_{\omega,k} + t_{Rk} g^{r}_{R\sigma k} v_{\omega,k} + \\
& \frac{i\pi^3 t_{L\omega} v^2_{\omega,\omega}}{1+\pi^2 v^2_{\omega,\omega}} v^{*}_{\omega,k} g^{r}_{R\sigma k} v_{\omega,k} - \frac{\pi^2 t_{R\omega} v_{\omega,\omega}}{1+\pi^2 v^2_{\omega,\omega}} v^{*}_{\omega,k} g^{r}_{R\sigma k} v_{\omega,k}\Bigg) \\
= & \ 2\pi i f_L(\omega) t^{*}_{L\omega} G^{r}_{\sigma} \times \Bigg(- \pi^2 t_{L\omega} v^2_{\omega,\omega} - i\pi t_{R\omega} v_{\omega,\omega} + \\
& \frac{\pi^4 t_{L\omega} v^4_{\omega,\omega}}{1+\pi^2 v^2_{\omega,\omega}} + \frac{i\pi^3 t_{R\omega} v_{\omega,\omega} v^2_{\omega,\omega}}{1+\pi^2 v^2_{\omega,\omega}}\Bigg) \qquad (2.8)
\end{aligned}$$

Now, the only unknown is the Green's function of the central quantum dot, namely the quantity G^{r}_{σ} in the above expression. It's derivation can be complicated and tedious if higher order correlations due to the interaction U is taken into account. Thus the next step would be to derive the quantity G^r_σ (in fact $G^<_\sigma$ as well). We however stop here since in the following chapters, they will be derived by SymGF. So, as far as this thesis is concerned, the above form is final for the purpose of the current formula.

Next, we evaluate the fourth term of Eq.(2.7) $\sum_k G^<_{R\sigma k}\Sigma^a_{Lv\sigma k}$ in Eq.(2.7). It is (see Eq.(8.27)):

$$\begin{aligned}\sum_k G^<_{R\sigma k}\Sigma^a_{Lv\sigma k} = {} & \frac{i\pi t^*_{L\omega}}{1+\pi^2 v^2_{\omega,\omega}} \times \\ & \Big(2\pi^2 t_{L\omega} G^r_\sigma (f_R(\omega) - f_L(\omega)) v^2_{\omega,\omega} - \pi^2 t_{L\omega} G^<_\sigma v^2_{\omega,\omega} - \\ & 2\pi i G^r_\sigma f_R(\omega) t_{R\omega} v_{\omega,\omega} + i\pi G^<_\sigma t_{R\omega} v_{\omega,\omega} + \\ & 2\pi^2 G^r_\sigma (f_R(\omega) - f_L(\omega)) v^2_{\omega,\omega} \times B\Big)\end{aligned}$$

where B is defined in Eq.(8.21).

Third, we evaluate the first term in Eq.(2.7) $\sum_{kk'} G^r_{R\sigma kk'}\Sigma^<_{kk'}$. It is (see Eq.(8.28)):

$$\begin{aligned}\sum_{kk'} G^r_{R\sigma kk'}\Sigma^<_{kk'} &= 2\pi i f_L(\omega) \sum_{kk'} G^r_{R\sigma kk'} v_{\omega,k} v^*_{\omega,k'} \\ &= 2\pi i f_L(\omega) \sum_k \frac{1}{1+\pi^2 v^2_{\omega,\omega}} \Big(g^r_{R\sigma k} v^*_{\omega,k} + \\ &\quad G^r_{R\sigma k}\left(-i\pi t^*_{R\omega} v^*_{\omega,\omega} - \pi^2 t^*_{L\omega} v^2_{\omega,\omega}\right)\Big) v_{\omega,k} \\ &= 2\pi i f_L(\omega) \frac{1}{1+\pi^2 v^2_{\omega,\omega}} \Big(- i\pi v^2_{\omega,\omega} + \\ &\quad \sum_k G^r_{R\sigma k} v_{\omega,k}\left(-i\pi t^*_{R\omega} v^*_{\omega,\omega} - \pi^2 t^*_{L\omega} v^2_{\omega,\omega}\right)\Big)\end{aligned}$$

where the summation $\sum_k G^r_{R\sigma k} v_{\omega,k}$ has been contained in the evaluation of Eq.(2.8).

Fourth, we evaluate the second term in Eq.(2.7) $\sum_{kk'} G^<_{R\sigma kk'}\Sigma^a_{R\sigma kk'}$. It is (see Eq.(8.29)):

$$\begin{aligned}
\sum_{kk'} G^<_{R\sigma kk'}\Sigma^a_{kk'} &= \sum_{kk'} G^<_{R\sigma kk'} i\pi v_{\omega,k} v^*_{\omega,k'} \\
&= \frac{i\pi}{1+\pi^2 v^2_{\omega,\omega}} \sum_{kk'} F(k,k') v^*_{\omega,k'} v_{\omega,k} \\
&= 2\pi^2 i f_R(\omega) v^2_{\omega,\omega} + 2\pi^2 \left(f_R(\omega) - f_L(\omega)\right) v^2_{\omega,\omega} \sum_k Z_k v_{\omega,k} + \\
&\quad 2\pi^2 t^*_{L\omega} \left(f_R(\omega) - f_L(\omega)\right) v^2_{\omega,\omega} \sum_k G^r_{R\sigma k} v_{\omega,k} + \\
&\quad 2\pi i f_R(\omega) v^*_{\omega,\omega} t^*_{R\omega} \sum_k G^r_{R\sigma k} v_{\omega,k} + i\pi v^*_{\omega,\omega} t^*_{R\omega} \sum_k G^<_{R\sigma k} v_{\omega,k} - \\
&\quad \pi^2 t^*_{L\omega} v^2_{\omega,\omega} \sum_k G^<_{R\sigma k} v_{\omega,k}
\end{aligned}$$

In the above expression, all the summations have been evaluated in previous terms except $\sum_k Z_k v_{\omega,k}$ which turns out to be (see Eq.(8.30) and Eq.(8.22)):

$$\begin{aligned}
\sum_k Z_k v_{\omega,k} = \Big(&- i\pi v^2_{\omega,\omega} - i\pi t^*_{R\omega} v^*_{\omega,\omega} \sum_k G^r_{R\sigma k} v_{\omega,k} - \\
&\pi^2 t^*_{L\omega} v^2_{\omega,\omega} \sum_k G^r_{R\sigma k} v_{\omega,k} \Big) \frac{1}{1+\pi^2 v^2_{\omega,\omega}} .
\end{aligned}$$

The last term of Eq.(2.7) is $\sum_k G^<_{L\sigma k} t^*_{Lk}$. It is found to be (see Eq.(8.31)):

$$\begin{aligned}
\sum_k G^<_{L\sigma k} t{*}_{Lk} &= 2\pi^2 G^r_\sigma t_{R\omega} t^*_{L\omega} v_{\omega,\omega} \left(f_L(\omega) - f_R(\omega)\right) - \pi^2 t_{R\omega} t^*_{L\omega} v_{\omega,\omega} G^<_\sigma + \\
&\quad 2\pi i f_L(\omega) t^2_{L\omega} G^r_\sigma + 2\pi^2 \left(f_L(\omega) - f_R(\omega)\right) v_{\omega,\omega} t^*_{L\omega} G^r_\sigma C + \\
&\quad i\pi t^2_{L\omega} G^<_\sigma + \pi^2 G^r_\sigma t_{R\omega} v^2_{\omega,\omega} \left(f_L(\omega) - f_R(\omega)\right) - \pi^2 t_{R\omega} v^2_{\omega,\omega} G^<_\sigma + \\
&\quad 2\pi i f_L(\omega) t_{L\omega} v^*_{\omega,\omega} G^r_\sigma + 2\pi^2 \left(f_L(\omega) - f_R(\omega)\right) v^2_{\omega,\omega} G^r_\sigma C + \\
&\quad i\pi t_{L\omega} v^*_{\omega,\omega} G^<_\sigma
\end{aligned}$$

where we have defined

$$C \equiv \left(-\pi^2 t_{R\omega} v_{\omega,\omega}^2 - i\pi v_{\omega,\omega}^* t_{L\omega} + \frac{\pi^4 v_{\omega,\omega}^4 t_{R\omega}}{1+\pi^2 v_{\omega,\omega}^2} + \frac{i\pi^3 v_{\omega,\omega}^2 v_{\omega,\omega}^* t_{L\omega}}{1+\pi^2 v_{\omega,\omega}^2} \right)$$

Putting these expressions back in the current formula Eq.(2.7), we express the current in terms of the Green's functions (G_σ^r and $G_\sigma^<$) of the central quantum dot [1]. The next step is to derive G_σ^r and $G_\sigma^<$ either by hand or by SymGF using the equation of motion method. We shall use SymGF to be introduced in the following chapters of the thesis.

2.3 The Equation of Motion Method

Among the methods that can be used to calculate the Green's function of the central quantum dot, we choose the equation of motion (EOM) method. This is because EOM is very systematic and easy to implement on a computer. It also gives very reasonable results if one goes to a high enough order of the EOM iterations.

To derive an EOM for the Green's function (or correlator) $\langle\langle A(t)B(t')\rangle\rangle \equiv \langle T[A(t)B(t')]\rangle$, we differentiate with respect to the time variable:

$$\frac{d}{dt}\langle\langle A(t)B(t')\rangle\rangle = \langle\{A(t),B(t)\}\rangle\delta(t-t') - i\langle\langle[A(t),H]B(t')\rangle\rangle$$

where H is the Hamiltonian and Heisenberg equation of motion has been applied. The commutator $[A(t),H]$ usually generates more terms at time t, this

---

[1] A related derivation of current formula can be found in Ref.[41], but here we are giving a more general formula as the lesser Green's functions, which represent non-equilibrium statistics, enter the current formula.

implies that on the right hand side of the above equation, there are even more Green's functions. In this way, the original Green's function $\langle\langle A(t)B(t')\rangle\rangle$ is related to other Green's functions. Clearly, if there is no interaction, for example without the U_{lmnp} term in Eq.(1.1), the Hamiltonian is quadratic in terms of its operators and the EOM can be solved exactly. If the Hamiltonian H does contain interaction (e.g. Eq.(2.15)), in principle there can be an infinite number of EOMs and the problem can not be solved exactly. This requires that we artificially bring a closure to these EOMs, i.e., make approximations. Once we obtain a finite set of equations, it is straightforward to solve them.

To close the set of equations at certain level brings approximations to the theory which affects the final result. If we close it early, the result will be crude; if we close it late enough, the result is more accurate but the derivation becomes more tedious. This "early" and "late" closing can be done in many ways. For example if we require the maximum number of the equations to be 100, then further Green's functions will be approximated with either 0 or another easily accessible number or expression. Or, we can refine this rule and require that a group of Green's functions containing operators of the leads can have a maximum of 50 equations. Each of the closing method represents its own approximation. The most accessible way we found is to count the maximum number of operators belonging to different parts of the transport system: when this type of operators exceeds a specified limit in a Green's function, that Green's function then is approximated with the product of an equal time correlator and a Green's function that contains the rest of the operators. The particular choice of the limit of each kind of operators is called a truncation rule or decoupling scheme.

In the following sections, we shall exemplify the use of EOM by two examples, one without truncation and the other with it.

2.4 Example I: Single Non-Interacting Quantum Dot

We wish to demonstrate the usual mathematical procedure for solving transport problems with some simple examples. In this section we consider a single-leveled single quantum dot without the on-site interaction term U, and the quantum dot is connected to two leads, i.e. Fig.1.1. We write the Hamiltonian here:

$$\hat{H} = \sum_{\alpha k} \epsilon_{\alpha k} c^{\dagger}_{\alpha k} c_{\alpha k} + \epsilon d^{\dagger} d + \sum_{\alpha k} t_{\alpha k} c^{\dagger}_{\alpha k} d + h.c. \tag{2.9}$$

Since there is no interaction, this Hamiltonian is quadratic in terms of the operators and can be solved exactly by several methods. Here we do it with EOM in preparation for our subsequent development of the SymGF. We wish to find the expression of the Green's function $\langle\langle d(t) d^{\dagger}(t')\rangle\rangle$, where again $\langle\langle \cdots \rangle\rangle$ is the time-ordered correlator or Green's function, or in its Fourier transformed form $\langle d d^{\dagger}(\omega)\rangle$.

We know from the previous section that for the Green's function $\langle d(t) d^{\dagger}(t')\rangle$ where t, t' are time indexes, taking its temporal derivative one obtains,

$$\begin{aligned} \frac{d}{dt}\langle\langle d(t) d^{\dagger}(t')\rangle\rangle = {} & \langle\{d(t), d^{\dagger}(t)\}\rangle \delta(t-t') \\ & -i\langle\langle [d(t), H] | d^{\dagger}(t')\rangle\rangle \end{aligned} \tag{2.10}$$

In Fourier space this is

$$\omega\langle dd^\dagger(\omega)\rangle = 1 - i\langle [d,H]d^\dagger(\omega)\rangle \ , \tag{2.11}$$

where we have used the fact that $\{d, d^\dagger\} = 1$. By explicitly evaluating the commutator between the operator d and the Hamiltonian H in Eq.(2.9), *e.g.* $[d, H]$, we obtain an algebraic equation for the Green's function $\langle dd^\dagger\rangle$ as

$$\omega\langle dd^\dagger(\omega)\rangle = \epsilon\langle dd^\dagger(\omega)\rangle + 1 + \sum_{\alpha k}\langle c_{\alpha k}d^\dagger(\omega)\rangle t^*_{\alpha k} \ .$$

After a little manipulation:

$$\langle dd^\dagger(\omega)\rangle = \frac{1}{\omega-\epsilon}\left(1 + \sum_{\alpha k}\langle c_{\alpha k}d^\dagger(\omega)\rangle t^*_{\alpha k}\right) \ . \tag{2.12}$$

We find that in Eq.(2.12) there is a new Green's function $\langle c_{\alpha k}d^\dagger(\omega)\rangle$. We shall derive an EOM for it. This time we directly work in Fourier space and have:

$$\omega\langle c_{\alpha k}d^\dagger(\omega)\rangle = -i\langle [c_{\alpha k}, H]d^\dagger(\omega)\rangle \ ,$$

where we used the fact that $\{c_{\alpha k}, d^\dagger\} = 0$, as these operators belong to different parts of the transport system. Explicitly evaluating the commutator $[c_{\alpha k}, H]$, we obtain:

$$\omega\langle c_{\alpha k}d^\dagger(\omega)\rangle = \epsilon_{\alpha k}\langle c_{\alpha k}d^\dagger(\omega)\rangle + \langle dd^\dagger(\omega)\rangle t_{\alpha k}$$

or in a neater form:

$$\langle c_{\alpha k}d^\dagger(\omega)\rangle = \frac{1}{\omega-\epsilon_{\alpha k}}\langle dd^\dagger(\omega)\rangle t_{\alpha k} \ . \tag{2.13}$$

In Eq.(2.13), no new Green's function is present, thus Eq.(2.12) and Eq.(2.13) form a complete set of EOMs for this transport system. Rewriting them here:

$$\langle dd^\dagger(\omega)\rangle = \frac{1}{\omega-\epsilon}\left(1+\sum_{\alpha k}\langle c_{\alpha k}d^\dagger(\omega)\rangle t^*_{\alpha k}\right)$$
$$\langle c_{\alpha k}d^\dagger(\omega)\rangle = \langle dd^\dagger(\omega)\rangle t_{\alpha k}\frac{1}{\omega-\epsilon_{\alpha k}}$$

and solving them, we have:

$$\langle dd^\dagger(\omega)\rangle = \frac{1}{\omega-\epsilon+i\pi\sum_\alpha t_{\alpha\omega}t^*_{\alpha\omega}} \tag{2.14}$$

And this Green's function is what we are interested in. It represents a density of states (DOS) that is shown in Fig.2.2. When we made this numerical plot, we used the wide-band limit (WBL) approximation[23, 38] such that the coupling parameters $t_{\alpha k}$ are assumed to be energy independent (independent of k) and the real part of the self-energies due to the device leads are neglected. WBL approximation amounts to neglecting the electronic structure of the device leads by assuming constant DOS of the leads and constant coupling leads/central coupling. For leads made of metals as is the case for many experimental situations, the DOS of the leads around the Fermi level do not vary significantly so that WBL is a reasonable approximation. Discussions about the validity of WBL is elaborated in Ref.[38]. In addition, we also assume the leads to be symmetric so that $t_L = t_R$, which is common in experimental setups. The choice of the energy level ϵ is arbitrary. This DOS plot shows that there is a peak at $\omega = \epsilon$. Finally, once we put Eq.(2.14) back into the current or conductance formula [Eq.(2.3) or Eq.(2.4)], we obtain the desired transport properties (not shown).

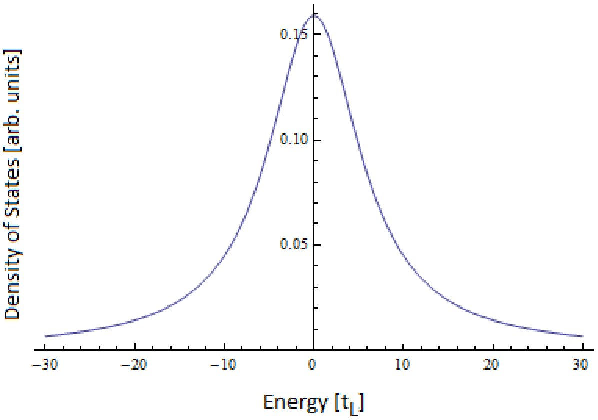

Figure 2.2: Density of states of the interaction-free central dot with wide-band limit approximation. The leads are assumed to be symmetric, $t_L = t_R$. Arbitrary units for ordinate. Abscissa is in units of t_L. The energy level of the central dot ϵ is set to be zero.

2.5 *Example II: Transport with On-Site Interaction*

As a second example, let's consider a problem with a strong on-site interaction U in the quantum dot of Fig.1.1. The Hamiltonian of the device is no longer quadratic due to the U term. We assume an Anderson form:

$$\hat{H} = \sum_{\alpha k\sigma} \epsilon_{\alpha k\sigma} c^\dagger_{\alpha k\sigma} c_{\alpha k\sigma} + \sum_{\sigma} \epsilon_\sigma d^\dagger_\sigma d_\sigma + U d^\dagger_\uparrow d_\uparrow d^\dagger_\downarrow d_\downarrow + \left(\sum_{\alpha k\sigma} t_{\alpha k\sigma} c^\dagger_{\alpha k\sigma} d_\sigma + h.c. \right) \tag{2.15}$$

where $d^\dagger_\sigma$ and d_σ are operators for the central quantum dot and subscript σ represents the spin (↑ or ↓).

Such a Hamiltonian cannot be solved exactly because of the existence of the on-site interaction. Approximations have to be used and the choice of approximation certainly affect the final results. Here as an example of the derivation procedure we present a Hartree-Fock calculation, where four operator sequence $d_\uparrow^\dagger d_\uparrow d_\downarrow^\dagger d_\downarrow$ is approximated with a sequence of half the operators times the expectation value of the other half of the operators, as $d_\uparrow^\dagger d_\uparrow \langle d_\downarrow^\dagger d_\downarrow \rangle$.

Just like that in the previous section, we write down the desired Green's function $\langle dd^\dagger \rangle$ and start deriving its EOM. Firstly, we have

$$\begin{aligned}\langle d_\sigma d_\sigma^\dagger(\omega)\rangle = & \frac{1}{\omega - U - \epsilon_\sigma}\big(1 + \langle c_{L\sigma}(k) d_\sigma^\dagger(\omega)\rangle t_{Lk}^* + \langle c_{R\sigma}(k) d_\sigma^\dagger(\omega)\rangle t_{Rk}^* - \\ & U\langle d_\sigma d_{\bar{\sigma}} d_{\bar{\sigma}}^\dagger d_\sigma^\dagger(\omega)\rangle\big) \ , \end{aligned} \tag{2.16}$$

where a $\bar{\sigma}$ means the opposite spin of σ. In Eq.(2.16) we have 3 new Green's functions. Secondly, we deal with the ones with operators that belong to the leads. With the same method as we obtained Eq.(2.16), we have

$$\begin{aligned}\langle c_{L\sigma}(k) d_\sigma^\dagger(\omega)\rangle &= \langle d_\sigma d_\sigma^\dagger(\omega)\rangle t_L(k)\frac{1}{\omega - \epsilon_{L\sigma}} \\ \langle c_{R\sigma}(k) d_\sigma^\dagger(\omega)\rangle &= \langle d_\sigma d_\sigma^\dagger(\omega)\rangle t_R(k)\frac{1}{\omega - \epsilon_{R\sigma}}\end{aligned} \tag{2.17}$$

In Eqs.(2.17), there are no new Green's functions, therefore the only one left is $\langle d_\sigma d_{\bar{\sigma}} d_{\bar{\sigma}}^\dagger d_\sigma^\dagger(\omega)\rangle$. If we derive its EOM, $\langle d_\sigma d_{\bar{\sigma}} d_{\bar{\sigma}}^\dagger d_\sigma^\dagger(\omega)\rangle$ will generate another 6 Green's functions. Each of these 6 Green's functions can generate 5 Green's functions, and so on. This is the reason why we cannot solve Eq.(2.15) exactly: the EOMs keep expanding without closures. This is also why we need a rule to truncate some of the Green's functions. In this example of a single quantum dot with finite on-site interaction, we require that the total number of d_σ's and $d_\sigma^\dagger$'s do not exceed two and Green's functions with extra operators should be truncated with the following rules:

$$\langle d^\dagger_\sigma d_\sigma O\rangle \approx N_\sigma \langle O\rangle \tag{2.18}$$

$$\langle c^\dagger_{\alpha k} c_{\alpha k'} O\rangle \approx f_\alpha(k)\delta(k-k')\langle O\rangle \ . \tag{2.19}$$

In particular, we apply rule (2.18) when the number of $d^\dagger_\sigma$ plus the number of d_σ exceeds 2; and we apply rule (2.19) when the number of $c^\dagger_{\alpha k}$ plus the number of $c_{\alpha k}$ exceeds 1. These truncation rules completely determines the order and accuracy of the final formula. We associate the number 2 to rule (2.18) because this gives the Hartree-Fock approximation. In this way, the EOM $\langle d_\sigma d_{\bar\sigma} d^\dagger_{\bar\sigma} d^\dagger_\sigma(\omega)\rangle$ is no longer evaluated with the Heisenberg equation of motion, but with the truncation rule (2.18) as:

$$\langle d_\sigma d_{\bar\sigma} d^\dagger_{\bar\sigma} d^\dagger_\sigma(\omega)\rangle = (1-N_\sigma)\langle d_\sigma d^\dagger_\sigma(\omega)\rangle \ . \tag{2.20}$$

Now, all the Green's functions have an EOM and Eqs.(2.16,2.17,2.20) form a complete and closed set of equations.

We rewrite the EOMs here:

$$\begin{aligned}
\langle d_\sigma d^\dagger_\sigma(\omega)\rangle &= \frac{1}{\omega-U-\epsilon_\sigma}\big(1+\langle c_{L\sigma}(k) d^\dagger_\sigma(\omega)\rangle t^*_{Lk} + \langle c_{R\sigma}(k) d^\dagger_\sigma(\omega)\rangle t^*_{Rk} - \\
&\quad U\langle d_\sigma d_{\bar\sigma} d^\dagger_{\bar\sigma} d^\dagger_\sigma(\omega)\rangle\big) \\
\langle d_\sigma d_{\bar\sigma} d^\dagger_{\bar\sigma} d^\dagger_\sigma(\omega)\rangle &= (1-N_\sigma)\langle d_\sigma d^\dagger_\sigma(\omega)\rangle \\
\langle c_{L\sigma}(k) d^\dagger_\sigma(\omega)\rangle &= \langle d_\sigma d^\dagger_\sigma(\omega)\rangle t_L(k)\frac{1}{\omega-\epsilon_{L\sigma}} \\
\langle c_{R\sigma}(k) d^\dagger_\sigma(\omega)\rangle &= \langle d_\sigma d^\dagger_\sigma(\omega)\rangle t_R(k)\frac{1}{\omega-\epsilon_{R\sigma}} \ .
\end{aligned} \tag{2.21}$$

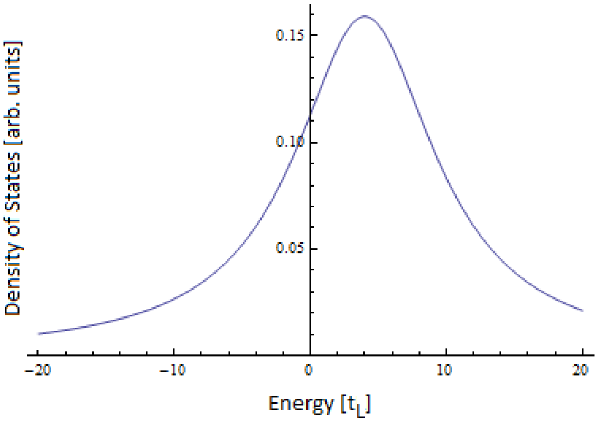

Figure 2.3: Non-self-consistent density of states of central dot with on-site interaction. Wide-band limit approximation is used and we assume symmetric leads $t_L = t_R$. Arbitrary unit for the ordinate; units for the horizontal axis is t_L. The energy level of the central dot ϵ is set to zero. The on-site interaction $U = 8t_L$ and occupation number $N_\sigma = 0.5t_L$.

We emphasize that it is the strict truncation rule (2.18) that made the second EOM in Eq.(2.21) (with the left hand side $\langle d_\sigma d_{\bar{\sigma}} d^\dagger_{\bar{\sigma}} d^\dagger_\sigma(\omega)\rangle$) not producing any further correlators. Solving the above closed EOM (2.21), we obtain:

$$\langle d_\sigma d^\dagger_\sigma(\omega)\rangle = \frac{1}{\omega - \epsilon_\sigma - N_\sigma U + i\pi \sum_\alpha t_{\alpha\omega} t^*_{\alpha\omega}} \ . \tag{2.22}$$

Comparing this with Eq.(2.14), we see that the only difference is that the energy level ϵ is now replaced by an effective energy level $\epsilon_\sigma + N_\sigma U$, where the shift of the energy level is proportional to the occupation number N_σ. This is a general feature of the Hartree-Fock approximation where the averaged interactions shift the original energy levels. We plot in Fig.2.3 the imaginary part of Eq.(2.22), which is the DOS of the quantum dot.

In plotting Fig.2.3, we used WBL approximation and all the parameters are chosen to be the same as in Fig.2.2 - except the new parameters U and N_σ.

We see from both figures that the peak is shifted by $N_\sigma U$, just as Eq.(2.22) described. This features the Hartree-Fock approximation which is a mean-field theory, meaning every particle moves in the average potential produced by all the other particles. In our case, the average is the occupation number N_σ and therefore it gives a shift of $N_\sigma U$.

By putting Eq.(2.22) back into Eq.(2.4) (as $G^r(\omega)$) we get the conductance formula for this single dot system at Hartree-Fock level.

2.6 Summary

In this chapter we presented the central quantity that quantum transport theory has to solve for, i.e., the current and/or conductance. We demonstrated that the current formula varies with different layouts of the device structures. We also demonstrated the standard procedure of solving steady state quantum transport problems within the NEGF formalism, and discussed the iterative procedure of the EOM for solving the Green's functions. The following steps summarize the procedure for solving a quantum transport problem.

Step 1. For a given physical problem, make a model - meaning proposes a Hamiltonian in the second quantized form. Physical intuition is necessary.

Step 2. Write down the required Green's function (usually the Green's function of the central quantum dot). This is the starting point.

Step 3. Derive the EOMs for the Green's functions.

Step 4. For each of the new Green's functions produced by older Green's functions after the EOM iteration, check if it has reached the number of operators in our truncation rules. If yes, truncate it; if not, repeat **Step 3** for it.

Step 5. Repeat **Step 3** and **Step 4** until all Green's functions has an EOM and a closure is reached. Then, the required Green's function can be solved from the final set of linear algebraic equations.

3

The Development of SymGF

In Chapter 2, the formula for electric current and conductance of transport junctions were derived in terms of the Green's function of the scattering region (e.g. the quantum dot). Two simple examples were discussed in Section 2.4 and 2.5 where equation of motion method was applied to derive the Green's functions. Once the Green's functions were derived and plugged into Eqs.(2.3,2.4), the transport results are essentially obtained if the integrations in these equations can be carried out. In most cases, the final integrals are done numerically and will not be the main concern of this thesis. The main concern is to derive the Green's functions for interacting systems to higher order correlations so that phenomenon such as the Kondo effects, can be investigated. Experimentally, the devices can be much more complicated than those shown in Figs.1.1 and 2.1, for instance double and triple quantum dot devices are not uncommon in recent literature[42, 43, 44, 45, 46, 47, 48]. Correlated transport physics in these systems are interesting and important, but their theoretical analysis is routinely impeded by the complexity of the problem.

As we discussed in Chapter 2, while EOM can in principle be iterated to any order by hand and, indeed, many heroic works have been done that way[6, 33], but the algebra quickly becomes unbearable and error prone. On the other hand, the examples in Chapter 2 showed that the mathematical procedure of EOM is actually rather mechanical: by brute force iterations with the help of the truncation rules. With this in mind, it would be extremely helpful to quantum transport theory if we could develop a software that symbolically derives the Green's functions on a computer.

This chapter presents the development of such a symbolic software package SymGF, standing for symbolic Green's function, for deriving Green's functions that appear in the transport formula such as those in Eqs.(2.3,2.7). The rest of this chapter discusses the technical details of SymGF, including the algorithms it adopts and its implementation. Our discussion will be targeted on general interacting systems where $U \neq 0$. For problems without interaction, as we mentioned in Chapter 2, the Green's functions can always be derived exactly as there are just a finite number of equations of motion, and, of course, SymGF will obtain the exact result as well.

3.1 The Goal of SymGF and its Input/Output

In quantum transport theory, a most critical step is to write down the Hamiltonian for a problem, such as Eq.(2.5) for the device in Fig.(2.1), and Eq.(2.15) for that in Fig.1.1. This step is motivated by the physical phenomenon and by physical intuition where the computers cannot help. After the Hamiltonian is determined and EOMs are iterated as that presented in Section 2.3, truncation rules are needed. These rules are also motivated by physical phenomenon and intuition. For instance, as discussed in Fig.4.3, the Kondo resonance involves virtual processes of co-tunneling, so that two particle dynamics must be included. This requirement suggests certain truncation rules and also certain order of the EOM iteration (see Chapter 4 below). These considerations cannot be done by a computer.

Therefore, the three important inputs to SymGF are: (i) the second quantized form of the Hamiltonian; (ii) the commutation rules of the operators involved in the Hamiltonian; (iii) the truncation rule for the operators. What we wish SymGF to do is to take these three sets of inputs, derive the analytical formula of the Green's functions of the device scattering region without further human involvement. Moreover, we also wish to be able to control the accuracy of the SymGF formula and observe how higher order formula affects the results. The present version of SymGF has fulfilled these design goals.

For simplification of the symbolic code, the present version of SymGF is helped a little by inputting a list of summation scripts and a list of preserved operators. We now explain them in the following. The list of summation scripts tells SymGF which subscrips are summed over. For example, in the lead's Hamiltonian (see Eq.(2.15), for example), one usually has $\sum_k c_k^\dagger c_k$, where k can be discrete or continuous; hence k is in the list of summation scripts to ensure

SymGF does not treat k as an independent variable. This list can be removed in a future version of SymGF by a language parser subroutine which finds all the summed variables and put them into the list automatically before the SymGF run. The list of preserved operators is needed because there is a freedom of choosing which operator in a Green's function should be differentiated when EOM is iterated. Namely, for a Green's function $\langle\langle A(t)B(t')\rangle\rangle$, we can either differentiate the variable t or t', thus creating new correlators at time t or t'. We often wish to preserve the operators with simpler forms. This list can be removed in a future version of SymGF by an automatic preprocessing routine that will make an educated "guess", so that the resulting equation of motion has less subscripts, etc.. These issues are purely technical and not essential for the works of SymGF.

After a SymGF run, it gives a series of outputs. First, it outputs a complete set of EOMs in terms of a set of self-energies defined automatically by SymGF. Second, SymGF outputs the solved Green's functions we demanded, also in terms of the automatically defined self-energies. Third, it outputs the list of definitions of the self-energies. Depending on the problem, the self-energies can be simple or very complicated. We made significant effort in order for SymGF to identify the self-energies in clever and natural fashion. By inspecting the analytical solutions provided by SymGF, we can easily tell what and which processes and transitions are considered in the calculations. In Chapter 4 we will show an example where we could identify the terms that contribute to the Kondo effect by examining the list of non-zero Green's functions given by SymGF.

3.2 Deriving EOMs and Truncation of Correlators

The first function of SymGF is to derive the equations of motion. Section 2.3 presented the EOM methodology. A simple example was presented in Section 2.5 for derivations up to the Hartree-Fock level. Here we focus on how the set of EOMs are closed by applying the truncation rules to arbitrary level of correlators.

As already discussed in Chapter 2, when interaction is present, EOMs will iterate further and further to higher orders indefinitely, ending up with infinite number of EOMs. To solve them we need to close the set at some point. The way to close is to apply the mean field approximation when we have had high enough orders of Green's functions. How high is high enough? This question is determined by physics. For instance, 2nd order iteration will give Hartree-Fock level of physics; 3rd order iteration will give the basic Kondo physics (but not very accurate); and so on.

The order of Green's functions is presented by the number of operators of each kind (each subspace of the Hamiltonian). In SymGF, we input the truncation rules that provide the maximum allowed number of operators in any Green's function. Whenever SymGF has derived a Green's function (correlator) whose operators of that particular kind has exceeded the maximum number, SymGF uses the truncation rule to “cut off” the extra operators in the correlator by essentially a mean-field approximation. When this happens, the “long”, high order correlator is replaced by an equal-time correlator multiplied by a lower order correlator. In Section 2.5, we have seen such truncation rules like Eqs.(2.18,2.19); and later in Section 3.6.1 we shall see rules like Eq.(3.16).

If a Green’s function on the right-hand side of an EOM is a new one, SymGF goes on to derive an EOM for this new Green’s function. This process is iterated until no new Green’s functions are found. At that moment, SymGF has completed the EOM derivation and it proceeds to solve the set of EOMs.

3.3 Algorithm for Solving EOMs

Once the set of EOM is obtained, SymGF solves them to obtain the desired Green’s functions. Solving an array of equations is generally much more difficult than deriving them. Here we require SymGF to have the ability of solving the EOMs with none or minimal human interference.

If we simply consider each Green’s function as one single unknown, then the EOMs are standard linear equations for these unknowns. Solving an array of linear equations has a well established methodology and most of them are very reliable, robust and efficient. Unfortunately, due to the extra degrees of freedom that Green’s functions may have, they cannot usually be viewed as regular variables. For example, suppose a Green’s function is defined as $G(k) = \langle \hat{c}^\dagger(k)\hat{d}\rangle$, where $\hat{c}^\dagger$ and $\hat{d}$ are operators, and k is a subscript representing energy. Then the EOM with this Green's function on the left-hand side actually represents a set of (uncountably) infinite number of equations, as for each value of k there is a $G(k)$, and therefore the Green's function $G(k)$ cannot be viewed as just one unknown variable.

Therefore, solving the EOMs requires special attention, and most of the development was devoted to this task. In the following subsections, we shall discuss all the methods we implemented into SymGF for solving the EOMs.

3.3.1 Direct Iteration

Direct iteration is to substitute the right hand side of an EOM into other EOMs. For example, suppose we have the following set of EOMs,

$$G_1 = C_1 + \sum_k C_2(k)G_2(k) + \sum_{k'} C_3(k')G_3(k') \tag{3.1}$$

$$G_2(k) = C_4(k)G_1 \tag{3.2}$$

$$G_3(k) = C_5(k)G_1 \tag{3.3}$$

where the Green's function G_1 is a number, G_2 and G_3 depend on subscript k, which is an abstract representation of some quantum number, C's are coefficients, and we wish to solve for G_1. What we can do is to substitute Eq.(3.2) and Eq.(3.3) into Eq.(3.1), sum over all the necessary subscripts, and obtain an algebraic equation of a singe variable G_1, as

$$G_1 = C_1 + \sum_k C_2(k)C_4(k)G_1 + \sum_{k'} C_3(k')C_5(k')G_1 \ .$$

Here, it is natural to see quantities $\sum_k C_2(k)C_4(k)$ and $\sum_{k'} C_3(k')C_5(k')$ as self-energies. In this way, G_1 is solved.

This method of solution is the most straightforward and in principle it can solve all the algebraic equations. However, when EOMs become more complicated, we will have serious problems for recognizing self-energies symbolically by the computer. In addition, when more subscripts are present, recognizing each kind of summation subscripts and correctly sum them up symbolically is not simple. One often ends up with a series of expressions which have the same subscript but different ordering and range of summation. Of course, in principle this can still be solved by inventing very delicate symbolic algorithms. Indeed, human eyes can usually quickly identify - from within very complicated expressions, which factors belong to which self-energy. SymGF has not reached that level of patten recognition. Hence, even though SymGF has a direct iteration method, we do not recommend the use of direct iteration until very smart algorithms can be invented in the future. Instead, we recommend the use of Gaussian Elimination method described in Section 3.3.4, which is a lot more powerful and elegant.

3.3.2 Graph-Aided Solution

The idea of graph-aided solution came from the observation that for a single-level quantum dot problem, the Anderson model Hamiltonian (see Eq.2.15) gives EOMs in a special way. Namely, the Green's functions that can be represented by a c-number (dimension 1×1 matrix) and Green's functions that have a continuous subscript (for example the k in Eq.(2.17), hereafter termed continuous Green's function), alternate in the sequence of EOMs. In other words, an

EOM always states that a Green's function of dimension 1 × 1 is equal to the product of a continuous Green's function and a coefficient that depends on the same continuous subscript summed over, like $G_i = \sum_k C(k)G_j(k)$. On the other hand a continuous Green's function is equal to the product of a coefficient which depends on a continuous subscript and a Green's function of dimension 1 × 1. For example, in the equations of motion that SymGF derives, the following is always true:

$$\begin{aligned} G_1 &= \sum_k C_1(k)G_i(k) + ... \\ G_i(k) &= C_2(k)G_j + ... \end{aligned}$$

In the first EOM, the left hand side G_1 is an 1 × 1 Green's function; the right hand side is a coefficient C_1 multiplied by a continuous Green's function G_i - both C_1 and G_i depend on the same continuous index k. Then, in the next EOM, the left hand side is a continuous Green's function with index k, the right hand side is a coefficient C_2 - having the same index k, multiplied by an 1 × 1 Green's function.

The above observation allows us to use a graph to represent the EOMs. If we denote a Green's function by a vertex, denote the coefficients (e.g. C_1, C_2) as the weight on the directed edges connecting the vertices, then the resulting graph completely describes the set of EOMs. Consequently, solving the EOMs is equivalent to solving the graph, whose steps are shown in the following example. Let's consider a partial graph shown in Fig.3.1. In this figure, the number in the circles are the serial number (the index) of each Green's functions. For example

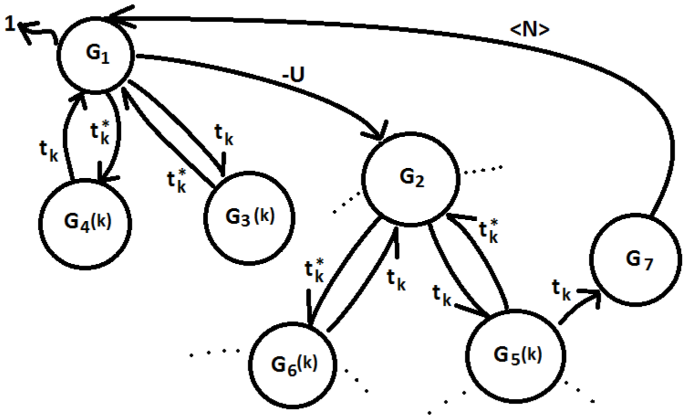

Figure 3.1: A simplified part of a graph representing a whole set of EOMs. The numbers in the circles represent the serial number of the Green's functions. The letter "k" following some of the numbers means that Green's function is dependent on subscript "k". Each out-going edge of a circle (a Green's function) represent a term of the EOM of that Green's function, which is the product of the weight of the edge and the Green's function at the destination of that edge.

the circle on the upper-left corner with "G_1" inside, it represents the Green's function G_1 which is our starting point of EOMs and it is probably the Green's function we are trying to solve. If a Green's function is followed by k, it means this Green's function depend on the subscript k. For example right below the circle of G_1, we have the circle for Green's function $G_4(k)$. Each out-going edge from a circle (a Green's function) represents a term on the right hand side of the EOM corresponding to that Green's function, which is the product of the Green's function at the destination of the edge and the weight of the edge itself. For example, we have an edge from G_1 to $G_4(k)$, and the weight is t_k^*, then we know the EOM for G_1 has a term $t_k^* G_4(k)$, where we have assumed that the subscript k is to be summed over. Therefore, Fig.3.1 represents the following

EOMs:

$$\begin{aligned}
G_1 &= 1 + \sum_k t_k^* G_4(k) + \sum_k t_k G_3(k) - U G_2 \\
G_4(k) &= t_k G_1 \\
G_3(k) &= t_k^* G_1 \\
G_2 &= \sum_k t_k^* G_6(k) + \sum_k t_k G_5(k) \\
G_6(k) &= t_k G_2 \\
G_5(k) &= t_k^* G_2 + t_k G_7 \\
G_7 &= N G_1 \ .
\end{aligned} \tag{3.4}$$

Note that to emphasize the use of mean-field approximation, the weight of the edge from Green's function 7 and 1 is an equal time correlator which is usually an occupation number, as shown in Fig.3.1, which is usually dtermined self-consistently later.

With this graph, and actually all the graphs corresponding to the single dot Anderson Model, we can conclude that, beginning from the Green's function G_1, following through the directed edges, each two steps contributes a self-energy; if a weight of an edge is the on-site interaction, then that edge does not contribute to a self-energy and self-energy begins from the next edge. For example in Fig.3.1, the path $G_1 \to G_3(k) \to G_1$ gives a self-energy $\sum_k t_k t_k^*$. From G_1 to G_2, the weight of the edge is the on-site interaction $-U$, so this one does not form a self-energy for G_1 or G_2, but of course this U has an impact, although not through a self-energy. But beginning from G_2, the path $G_2 \to G_5(k) \to G_7$

gives a self-energy in the same way as the path $G_1 \to G_3(k) \to G_1$.

With this criteria, one then keeps the Green's functions connected by self-energies or on-site interactions and can re-write another set of equations. This new set of equations are now linear equations and can be solved immediately. For Fig.3.1, what will be left in the new set of equations would be G_1, G_2, and G_7, as:

$$\begin{aligned} G_1 &= 1 + \Gamma G_1 + \Gamma G_1 - U G_2 \\ G_2 &= \Gamma G_2 + \Gamma G_2 + \Gamma G_7 \\ G_7 &= N G_1 \ , \end{aligned} \tag{3.5}$$

where for simplicity we have chose such an example so that there is only one self-energy $\Gamma = \sum_k t_k^* t_k$ for all equations.

The above graph method reproduces very efficiently the results reported in Ref.[33], as a benchmark of the SymGF algorithm. Despite the success of this method on the single quantum dot problem, it does not work on systems with multiple quantum dots such as the side-coupled double quantum dot device of Fig.3.3. We therefore developed another method to be discussed in the next subsection.

3.3.3 *Conditioned Iteration*

We have stated in Section 3.3.1 that direct iteration can in principle solve all the EOMs. The problem is the difficulty for recognizing self-energies symbolically. In the context of single level Anderson model Hamiltonian Eq.(3.24), this problem can be avoided by iterating not the Green's function itself, but the product and summation that comes with it.

Suppose we have a set of EOMs like Eq.(3.1-3.3), we can try to substitute $\sum_k C_2(k)G_2(k)$ as a whole and not just $G_2(k)$ alone. In particular, suppose in Eq.(3.1) we wish to remove $G_2(k)$, then the direct iteration method takes Eq.(3.2) - $G_2(k) = C_4(k)G_1$ and put it back in Eq.(3.1). Conditioned iteration method, on the other hand, applies the following precondition first: since the term containing $G_2(k)$ in Eq.(3.1) has the form $\sum_k C_2(k)G_2(k)$, we multiply Eq.(3.2) by $C_2(k)$ and sum over k. We then have

$$\sum_k C_2(k)G_2(k) = \sum_k C_2(k)C_4(k)G_1 \ . \tag{3.6}$$

The entire left hand side of Eq.(3.6) can be substituted back in Eq.(3.1). This approach is the conditioned iteration.

In this way, everything will have the same dimension as the first Green's function G_1 (in this case a scalar), and hence anything that has extra dimensions (for example, if they depend on k) is an unfinished self-energy. Therefore the recognition of self-energies is made much easier and this is the main advantage of the conditioned iteration method.

Of course, there are always "loops" in the graphs of the EOMs which means if we blindly iterate the Green's functions, we may fall into an infinite recursion of the ever increasing lump of expressions. When we meet "loops", we should immediately solve the vertex that leads the loop, i.e., the Green's function with the smallest serial number in the loop. For example, in Fig.3.1, we see that

G_2 is the sum of terms that contain G_1 and G_5, so if we blindly iterate over G_2, then the iteration will not stop as G_5 is related to G_2. In this case, we must solve for G_2 as soon as the "loop" is formed, i.e., when G_2 is expressed in terms of G_1, G_7 and G_2 itself ($G_5(k)$ and $G_6(k)$ will not appear here, as the iteration goes on there), we should stop iterating and solve for G_2 so that it is now expressed in terms of G_1 and G_7 only. With such an expression for G_2, we will not have "dead recursions" when we iterate the Green's functions. We have used this algorithm to obtain the higher order results of the side-coupled quantum dot system to be discussed in Chapter 4[7]. As far as we know, this is the first time that such higher order results were obtained for such a physical system.

We have so far limited ourselves to discussing the the most prototypical problem of single level Anderson model. It is very desirable to be able to deal with multiple energy levels as well. This is the point where we need yet another solution of the EOMs.

3.3.4 Gaussian Elimination

The reason that the EOMs are not regular linear equations is that they may contain extra degrees of freedom so that one EOM actually represents an infinitely many EOMs. For instance $G(k)$ has a continuous index k such that $G(k_1)$ and $G(k_2)$ are different variables if $k_1 \neq k_2$. Since k is continuous, we thus have infinite number of variables even though G is just one Green's function. What happens if we just enumerate them all so that they look like a regular array of linear equations? For instance, we may imagine discretizing the continuous k into infinitely many points $\{k_j\}, j = 1, 2, \cdots, \infty$ and treat each $G(k_j)$ as a variable. Can the resulting EOMs become regular linear equations now? The answer is *Yes*. They can be treated as regular linear equations once we overcome a little more complications induced by the infinity.

Arrays of linear equations are usually calculated in the language of matrix algebra, here we shall do the same. When Green's functions have more degrees of freedom, they, as well as their coefficients, become matrices themselves. A Green's function denoted by $G_i(k)$ may be seen as a vector ($1 \times \infty$ matrix); and another one denoted by $G_j(k,l)$ may be seen as a $\infty \times \infty$ matrix due to the two continuous indices k, l. The key is to hypothetically rearrange the elements of each of the Green's function so that each element is in a position of an independent variable. If a Green's function is a vector, then enumerate all its elements in a row besides the 1×1 Green's function. If it is a matrix, then enumerate the first row, and then enumerate the second row [1], and so on until all rows are finished. If it is a multi-dimensional array, the procedure is easily

---

[1] Strictly speaking, we can't reach the second row as there are alreadhy infinitely many elements in the first row. But if we consider the elements' growing into infinitely many to be a limiting case, then we can always formally write down the all the rows as if they have finite lengths.

Table 3.1: The matrix corresponding to EOMs (3.7-3.9). Contents above the horizontal line and to the left of the frist vertical line are indices indicating the meaning of each position and they are not part of the matrix itself.

	G_1	$G_2(1)$	$G_2(2)$	...	$G_3(1,1)$	$G_3(1,2)$	...	$G_3(2,1)$	...	rhs
G_1	1	$C_2(1)$	$C_2(2)$	...	0	0	...	0	...	C_1
$G_2(1)$	0	1	0	...	$C_4(1,1,1)$	$C_4(1,1,2)$	...	$C_4(1,2,1)$	...	0
$G_2(2)$	0	0	1	...	$C_4(2,1,1)$	$C_4(2,1,2)$	...	$C_4(2,2,1)$	...	0
$G_3(1,1)$	$C_5(1,1)$	0	0	...	1	0	...	0	...	0
$G_3(1,2)$	$C_5(1,2)$	0	0	...	0	1	...	0	...	0
...	...	...	...	...	...	...	...	...	...	...
$G_3(2,1)$	$C_5(2,1)$	0	0	...	0	0	...	1	...	0
...	...	...	...	...	...	...	...	...	...	...

extended. For example, if we have a set of EOMs as

$$G_1 = C_1 + C_2(k)G_2(k) \tag{3.7}$$

$$G_2(k) = C_4(k,k',k'')G_3(k',k'') \tag{3.8}$$

$$G_3(k,k') = C_5(k,k')G_1 \ , \tag{3.9}$$

then its corresponding matrix can be (hypothetically, since k's can be continuous thus having infinite possible values) written as in Tab.3.1. In Tab.3.1,every element of the matrix is a number, thus the matrix is just a regular matrix which can be solved with Gaussian elimination or any other methods. Nevertheless, since this matrix has infinite rows and columns, it still cannot be solved. We emphasize here that the matrix is still analytic as the elements are given in abstract symbols.

In order to solve this infinite matrix, we extend the Gaussian elimination method to matrices composed of block matrices. To do so, let's rewrite the matrix in Tab.3.1 into the following form:

$$M = \begin{pmatrix} I_{1\times 1} & A & 0 & C_1 \\ 0 & I_{|k|\times|k|} & B & 0 \\ D & 0 & I_{|k'||k''|\times|k'||k''|} & 0 \end{pmatrix}$$

where $I_{n\times n}$ is the unit matrix of size $n \times n$, zeros represent zero matrices in their respective size (since M is a block matrix, not indicating their size will not lead to confusion), $|k|$ is the number of possible values of the subscript k which we assume to be infinity. The block matrices in M are composed of the coefficients in the EOMs. In particular, A is a $1 \times |k|$ matrix whose element $A_k = C_2(k)$; B is a $|k| \times |k'||k''|$ matrix and $B_{k,k'k''} = C_4(k, k', k'')$, note that we have "flattened" the intuitively multi-dimensional array $C_4(k, k', k'')$ into a matrix B; and finally C is a $|k'||k''| \times 1$ matrix and $D_{k'k''} = C_5(k', k'')$. This is how our matrix should be established. We can now move on to do the Gaussian elimination.

Without loss of generality, we exemplify the idea of Gaussian elimination with a 2×2 matrix M whose elements are all blocks. We write it down as:

$$M = \begin{pmatrix} A & B \\ C & D \end{pmatrix}.$$

Then our goal is to use row transformation to eliminate the upper triangle (here it's just B). Denoting the first and second row as r_1 and r_2, we can achieve this by doing $r_1 - BD^{-1}r_2$. Then the new matrix would be:

$$M' = \begin{pmatrix} A - BD^{-1}C & 0 \\ C & D \end{pmatrix},$$

this completes the Gaussian elimination process since the upper right corner of the M matrix is now eliminated.

There is a problem, however. In the above procedure we have assumed that we can readily obtain the inverse of block D. The problem is that inverting an (generally) infinitely large matrix is not well defined, if ever possible. Fortunately, such blocks D is made up with coefficients from the EOMs that can always be written as the sum of an identity matrix and a "factored" matrix, i.e., their elements can always be written as $D_{ij} = I + a_i b_j$, where a and b are vectors. This enables us to use the binomial inverse theorem[49] which states:

$$(I + a_i b_j)^{-1} = I - \frac{a_i b_j}{1 + \sum_k a_k b_k} \ . \tag{3.10}$$

The above theorem works for the cases where there is only one non-diagonal term, i.e. $a_i b_j$.

There are still a few situations for which we endd up with the need of finding the inverse of matrices that involve multiple terms, e.g. we need to find the inverse of the following matrix:

$$I + \mathbf{u_1}\mathbf{v_1}^T + \mathbf{u_2}\mathbf{v_2}^T + ... + \mathbf{u_n}\mathbf{v_n}^T \tag{3.11}$$

where $\mathbf{u_i}$ and $\mathbf{v_j}$ are both column vectors and the superscript T means transpose. To find its inverse, we assume the inverse to have the following form:

$$I+C_{11}\mathbf{u_1}\mathbf{v_1}^T+C_{12}\mathbf{u_1}\mathbf{v_2}^T+...+C_{1n}\mathbf{u_1}\mathbf{v_n}^T+C_{21}\mathbf{u_2}\mathbf{v_1}^T+...+C_{nn}\mathbf{u_n}\mathbf{v_n}^T \quad (3.12)$$

where C_{ij} is the coefficient for $\mathbf{u_i}\mathbf{v_j}^T$ which is to be determined. Since a matrix multiplied by its inverse must be equal to the unit matrix, we obtain:

$$\begin{gathered}\left(I+C_{11}\mathbf{u_1}\mathbf{v_1}^T+C_{12}\mathbf{u_1}\mathbf{v_2}^T+...+C_{1n}\mathbf{u_1}\mathbf{v_n}^T+C_{21}\mathbf{u_2}\mathbf{v_1}^T+...+C_{nn}\mathbf{u_n}\mathbf{v_n}^T\right)\\ \times\left(I+\mathbf{u_1}\mathbf{v_1}^T+\mathbf{u_2}\mathbf{v_2}^T+...+\mathbf{u_n}\mathbf{v_n}^T\right)=I\end{gathered}$$

Expanding the above equation and letting coefficients of all terms with $\mathbf{u_i}\mathbf{v_j}^T$ to be zero, we obtain

$$\begin{pmatrix}\mathbf{v_1}^T\mathbf{u_1} & \mathbf{v_2}^T\mathbf{u_1} & ... & \mathbf{v_n}^T\mathbf{u_1}\\ \mathbf{v_1}^T\mathbf{u_2} & \mathbf{v_2}^T\mathbf{u_2} & ... & \mathbf{v_n}^T\mathbf{u_2}\\ \mathbf{v_1}^T\mathbf{u_3} & \mathbf{v_2}^T\mathbf{u_3} & ... & \mathbf{v_n}^T\mathbf{u_3}\\ ... & ... & ... & ...\\ \mathbf{v_1}^T\mathbf{u_n} & \mathbf{v_2}^T\mathbf{u_n} & ... & \mathbf{v_n}^T\mathbf{u_n}\end{pmatrix}\begin{pmatrix}C_{11}\\ C_{12}\\ C_{13}\\ ...\\ C_{1n}\end{pmatrix}=\begin{pmatrix}-1\\ 0\\ 0\\ ...\\ 0\end{pmatrix}$$

and

$$\begin{pmatrix}\mathbf{v_1}^T\mathbf{u_1} & \mathbf{v_2}^T\mathbf{u_1} & ... & \mathbf{v_n}^T\mathbf{u_1}\\ \mathbf{v_1}^T\mathbf{u_2} & \mathbf{v_2}^T\mathbf{u_2} & ... & \mathbf{v_n}^T\mathbf{u_2}\\ \mathbf{v_1}^T\mathbf{u_3} & \mathbf{v_2}^T\mathbf{u_3} & ... & \mathbf{v_n}^T\mathbf{u_3}\\ ... & ... & ... & ...\\ \mathbf{v_1}^T\mathbf{u_n} & \mathbf{v_2}^T\mathbf{u_n} & ... & \mathbf{v_n}^T\mathbf{u_n}\end{pmatrix}\begin{pmatrix}C_{21}\\ C_{22}\\ C_{23}\\ ...\\ C_{2n}\end{pmatrix}=\begin{pmatrix}0\\ -1\\ 0\\ ...\\ 0\end{pmatrix}$$

and so on, until

$$\begin{pmatrix} \mathbf{v_1}^T\mathbf{u_1} & \mathbf{v_2}^T\mathbf{u_1} & ... & \mathbf{v_n}^T\mathbf{u_1} \\ \mathbf{v_1}^T\mathbf{u_2} & \mathbf{v_2}^T\mathbf{u_2} & ... & \mathbf{v_n}^T\mathbf{u_2} \\ \mathbf{v_1}^T\mathbf{u_3} & \mathbf{v_2}^T\mathbf{u_3} & ... & \mathbf{v_n}^T\mathbf{u_3} \\ ... & ... & ... & ... \\ \mathbf{v_1}^T\mathbf{u_n} & \mathbf{v_2}^T\mathbf{u_n} & ... & \mathbf{v_n}^T\mathbf{u_n} \end{pmatrix} \begin{pmatrix} C_{n1} \\ C_{n2} \\ C_{n3} \\ ... \\ C_{nn} \end{pmatrix} = \begin{pmatrix} 0 \\ 0 \\ 0 \\ ... \\ -1 \end{pmatrix}$$

where, again, n is the number of terms involved in Eq.(3.11). Solving all these matrix equations, we obtain all the coefficients needed for the inverse; and thus the inverse matrix can be obtained. In this way, an inverse of a matrix of the special form can be obtained by matrix algebra, allowing Gaussian elimination to work. From our experience, the method in this section is the most general one for solving the EOMs.

3.4 Self-Energies

When we calculate Green's functions of a quantum dot (or any system that has coupling or interaction with other parties), we necessarily will generate self-energies due to the interaction. Self-energies embody the impact from other parts of the total Hamiltonian, and they are crucial to almost all the interesting physics that a Green's function can reveal. During the calculation of Green's functions by means of EOM, identifying the self-energies represent the most serious challenge of this work. I dedicate this section to self-energies for both of their importance and SymGF's weakness in identifying them.

3.4.1 Recognition and Evaluation of Self-Energies

In terms of solving a set of EOMs, the self-energies arise naturally as we substitute the higher order Green's functions with their EOMs. In a single level quantum dot model with continuous lead states (see, for example Hamiltonian Eq.(2.15)), they usually have the form of integration over the continuous quantum number. However, this cannot be used as a criterion for recognition of self-energies. It is quite likely that a self-energy has the impact from yet another self-energy, then in this case, there can be confusions when we need to decide which subscript(s) to be integrated first or should it (they) be integrated together with other subscripts represented by the same name (the simple strategy of direct iteration has this problem). Eq.(8.45) in the Appendix shows a complicated self-energy. As we see the integration over k affects up to three variables in Eq.(8.45). We could not and would not have refined this self-energy with just the direct iteration approach.

In the implementation of conditioned iteration method (see Section 3.3.3), integration of extra degree of freedom can be used as a criterion as it has unified the dimension of the unknowns with the desired Green's function that we are trying to solve. The problem of identifying self-energies is most elegantly and downrightly solved by the Gaussian elimination method. In Eq.(3.10), the self-energy arises as the trace of the original matrix on the denominator of the second term on the right hand side:

$$1 + \sum_k a_k b_k \ . \tag{3.13}$$

The identity matrix or number 1 in Eq.(3.13) is not part of the self-energy but that does not affect our argument. This has made a clearer picture that a self-energy helps finding a partial/temporary solution to the final result. Interestingly, “inverse” itself is a means of solving for the unknowns of equations in general.

Evaluating self-energies is not trivial. If we are to deal with a self-energy from a lead which has continuous states, then an integration over the continuous quantum number is imperative. If we have just one pole in the real axis, then the Plemelj formula[50] can be used for the integration which states $\frac{1}{x \pm i0^+} = P\frac{1}{x} \mp i\pi\delta(x)$, where δ is the Dirac δ-function. In this way, the integration can be carried out. When the system gets more complicated, for example a double quantum dot system, then the self-energies can have many poles on the real energy axis to cause trouble in the integration. In this scenario, we first observe that the Plemelj formula can be derived by choosing the integration contour in such a way that at the pole, the contour surrounds it in the half plane that doesn't contain the pole (although it is infinitesimally close to the real axis) followed by a direct use of Cauchy integration theorem. To do exactly the same to the self-energies with more poles, i.e., bypass the poles with surrounding contour into the analytic plane, we can extend the Plemelj formula to meet our needs. The example of side-couple double quantum dot to be presented in Chapter 4 used this method for evaluating self-energies.

When we adopt the Gaussian elimination method, the self-energies have a very obvious form, i.e., it is the trace as part of the denominator in Eq.(3.10) and the like. The forms are identical to their counterpart in conditioned iteration method.

3.4.2 Other Considerations about Self-Energies

Having established an approach to get the self-energies as discussed in the last subsection, here we discuss some general thoughts which may point to better approaches in the future.

First of all, it is quite reasonable to think that if we grasp the general form of the self-energy, perhaps we can just write them down or even write down the Green's functions in a systematic way without a tedious calculation. Self energy arising from EOM may have quite a genreal structure. For the many transport problems we have investigated using SymGF, the self-energies all roughly have the following form:

$$\begin{aligned} \Sigma_0(\omega) &= -i\pi \sum_{\alpha} t_\alpha(\omega) t^*_\alpha(\omega) \\ \Sigma_n(\omega) &= \frac{\Sigma_{n-1}}{1+\Sigma_{n-1}}, \end{aligned} \tag{3.14}$$

where n represents the order of that self-energy (the order during the EOM iteration). While this relation is not accurate, it seems that the existing self-energies fall into this form with only a few exceptions. An interesting further investigation is to do more analysis in order to have a solid conclusion.

Next, can we always derive analytical forms of the self-energies? This appears to be difficult. Clearly, if the self-energies have a simple form like Σ_0 in

Eq.(3.14), they definitely can be written in a analytic form. Unfortunately, for more complicated self-energies, what we usually obtain is an expression having an integration that cannot be done analytically. To do such integrations analytically, one has to find the poles on the real energy axis in order to evaluate their residues. The equation that determines the poles are algebraic but may have any order, for example an order of five or more: such a highly nonlinear root finding problem does not have an analytical solution in general. The present version of SymGF derives all the self-energy expressions but may not be able to complete the final integration. Therefore, for practical problems one has to evaluate these self-energies numerically during the plotting of the final transport results.

Finally, by doing a lot of analysis with SymGF, it appears empirically that most of the high order algebraic equations in the EOM analysis has at most three real solutions, thus higher order than three contains extraneous roots. If, by investigating the equation for determining the poles, we can rule out in advance the extraneous roots, we may end up with an algebraic root finding equation of order 3 that can then be solved analytically to find all the poles. This would allow self-energies to be derived completely analytically. The pole finding equations have been implemented in SymGF, but it works only for some special cases. A more general implementation requires significant further research and represents a future direction for SymGF.

3.5 Implementation of SymGF

We have developed SymGF using the symbolic language Mathematica[8]. SymGF relies heavily on Mathematica's powerful ability of pattern recognition and list manipulation. In terms of functions, SymGF can be divided into two parts: the derivation of EOMs, and solving the EOMs. For now, everything we do are in Fourier space.

The evaluation of commutators and anti-commutators is central to the derivation of EOMs. As we have seen in Section 2.3, EOM method requires frequent evaluation of commutators. Meanwhile, since we are mostly dealing with Fermions, what is given to SymGF is a list of anti-commutators. For this reason we make use of the following relation:

$$[AB, C] = \begin{cases} A[B, C] - [C, A]B \\ A\{B, C\} - \{C, A\}B \end{cases} \tag{3.15}$$

where the evaluation of the left hand side with commutators or anti-commutators have the same form. So that it would be much easier to carry out the Heisenberg equation of motion as we no longer need to worry about whether we have a commutator or anti-commutator. What is done in SymGF is just a recursive use of Eq.(3.15).

As stated in the previous section, the present version of SymGF uses Gaussian elimination to solve the desired Green's functions. The algorithm is quite straightforward, but during block matrix multiplication or block matrix inversion, there is room for optimization as we need summation over the row/column index, which is an integration. This is how self-energies are created in Gaussian elimination. When SymGF encounters such an integration, it keeps the integration unevaluated and substitutes with a new symbol indicating that this is a self-energy. When the SymGF run is finished, the user can choose his/her favorite methods to carry out the integrations. If we have progress in dealing with self-energies in the future, we can implement the automatic evaluation of such self-energies.

Mathematica provides a numerical calculus package that provides the function “NResidue”, which numerically calculate the residue at a given point. We used this function and a regular numerical integration command “NIntegrate” during the calculation of the T-shaped double quantum dot transport system (see Chapter 4). Whether this function will be integrated into SymGF depend on our future research on the self-energies.

3.6 Verification of SymGF

SymGF is a very complicated symbolic program which requires serious verification. We verify it by comparing results for both simple and rather complicated problems whose Green’s functions were derived by hand. Reproducing the same results gives us confidence that SymGF can be used to assist real research. The ultimate test is to compare physical results to experiments which will be the contents of the subsequent chapter.

3.6.1 Verification I: Non-Interacting Single Quantum Dot

We begin by verifying SymGF for the simplest transport problem, i.e., a single quantum dot connected to two leads and there is no interaction. The Hamiltonian is in Eq.(2.9). We have solved this system in Chapter 2.

To verify that SymGF produces the same results, we provide the following inputs in addition to the Hamiltonian. First, the anti-commutation relations, in SymGF's form, are:

$$\begin{aligned} \{d, d^\dagger, 1\} \\ \{c_L(k_1), c_L^\dagger(k_2), \delta(k_1 - k_2)\} \\ \{c_R(k_1), c_R^\dagger(k_2), \delta(k_1 - k_2)\} \end{aligned}$$

The first item, for example, means $\{d, d^\dagger\} = 1$; and it is similar for the rest where δ denotes the Dirac δ-function. Usually one has to provide the truncation rules, although it is unnecessary for this non-interacting problem, we provide it anyway as this is one of the most important input to SymGF

$$\begin{aligned} \{d, d^\dagger, 3, \{d^\dagger, d, N_d\}\} \\ \{c_L(k), c_L^\dagger(k), c_R(k), c_R^\dagger(k), 1, \{c_L(k_1)^\dagger, c_L(k_2), f_L(k_1)\delta(k_1 - k_2)\}, \\ \{c_R(k_1)^\dagger, c_R(k_2), f_R(k_1)\delta(k_1 - k_2)\}\} \end{aligned}$$

The above list is written in SymGF's style, in conventional way it would be:

$$\begin{aligned} \langle d^\dagger d O\rangle &\approx N_d \langle O\rangle \\ \langle c_\alpha^\dagger(k) c_\alpha(k') O\rangle &\approx f_\alpha(k)\delta(k - k')\langle O\rangle \end{aligned} \tag{3.16}$$

where whenever SymGF sees a total of more than 3 d's or $d^\dagger$'s in a single Green's function (for example one d and two $d^\dagger$'s), SymGF truncates this Green's function by replacing the sequence $d^\dagger d$ with N_d and approximate the original Green's function with N_d times the (shorter) Green's function which consists of the rest of the operators. So is true if total number of $c_{\alpha k}$ or $c^\dagger_{\alpha k}$ exceeds 1, then the sequences $c^\dagger_{\alpha k} c_{\alpha k'}$ will be replaced by $f_\alpha(k)\delta(k-k')$, where f_α is the Fermi distribution function of the lead marked by α. It should be noted that the numbers above only counts operators at one of the two times. For example, for a Green's function $\langle A(t)B(t)C(t), D(t')\rangle$, SymGF only counts the number of operators within $A(\omega)B(\omega)C(\omega)$ (since we are working in Fourier space). As we can see from a manual derivation, these truncation rules are not actually used, as it is mathematically not possible for the consequent Green's functions to have that many operators.

SymGF gave the identical result as the manual derivation Eq.(2.14). This is the first verification of SymGF.

3.6.2 *Verification II: Single Dot with Interaction*

Now we proceed to the single level single dot device with an nonzero on-site interaction U. The system is essentially Fig.1.1 and its Hamiltonian is in Eq.(2.15). It has been solved in Chapter 2 at the Hartree-Fock level. A higher level result can be found in Ref.[34]. We compare SymGF's results to both of them.

To reproduce the Hartree-Fock result by SymGF, we apply the following truncation rule (whose meaning will be explained later)

$$\begin{aligned}\{d_\sigma, d_\sigma^\dagger, 1, \{d^\dagger, d, N_\sigma\}\} \\ \{c_L(k), c_L^\dagger(k), c_R(k), c_R^\dagger(k), 1, \{c_L(k_1)^\dagger, c_L(k_2), f_L(k_1)\delta(k_1 - k_2)\}, \\ \{c_R(k_1)^\dagger, c_R(k_2), f_R(k_1)\delta(k_1 - k_2)\}\}\end{aligned} \tag{3.17}$$

And for higher order formula we should allow more operators in a single Green's function, namely (in SymGF syntax):

$$\begin{aligned}\{d_\sigma, d_\sigma^\dagger, 3, \{d^\dagger, d, N_\sigma\}\} \\ \{c_L(k), c_L^\dagger(k), c_R(k), c_R^\dagger(k), 1, \{c_L(k_1)^\dagger, c_L(k_2), f_L(k_1)\delta(k_1 - k_2)\}, \\ \{c_R(k_1)^\dagger, c_R(k_2), f_R(k_1)\delta(k_1 - k_2)\}\}\ .\end{aligned} \tag{3.18}$$

In conventional form, the above means:

$$\langle d_\sigma^\dagger d_\sigma O\rangle \approx N_\sigma \langle O\rangle \tag{3.19}$$

$$\langle c_\alpha^\dagger(k) c_\alpha(k') O\rangle \approx f_\alpha(k)\delta(k - k')\langle O\rangle \tag{3.20}$$

and Rule (3.19) is applied whenever SymGF finds more than 1 [in Rule (3.17)] or 3 [in Rule (3.18)] $d_\sigma^\dagger$'s or d_σ's in a Green's function; Rule (3.20) is applied with more than one $c_\alpha^\dagger(k)$ or $c_\alpha(k)$.

From the above examples we have used different truncation rules for different operators. Usually we allow more operaotors if that kind of operators represent the physics we are more interested in. This only affects the approximations that we make.

In this subsection, lowest order (Hartree-Fock) results refers to the formula obtained with Rule (3.17), and higher order results refer to the formula obtained with Rule (3.18). At the Hartree-Fock level, SymGF gave identical results as in Eq.(2.22).

Ref.[34] addresses the same system at the high order and we shall use the result as a test to SymGF. For the higher order calculation using the Rule (3.18), SymGF gives:

$$
\begin{aligned}
G^r_\downarrow(\omega) &= \langle d_\sigma d^\dagger_\sigma(\omega)\rangle \\
&= \big(-4(-1+N_\uparrow)U - 4\omega - 2i(2\Gamma_1+\Gamma_2) + 4\epsilon_\downarrow\big)\Big/\Big((2\omega + i\Gamma_2 - 2\epsilon_\downarrow) \\
&\quad (2U - 2\omega - i(2\Gamma_1+\Gamma_2) + 2\epsilon_\downarrow) + 2iU\Gamma_1\big(f(\omega+\epsilon_\uparrow-\epsilon_\downarrow) + \\
&\quad f(U-\omega+\epsilon_\uparrow+\epsilon_\downarrow)\big)\Big) \ . \qquad (3.21)
\end{aligned}
$$

In Ref.[34], the formula for $\langle d_\sigma d^\dagger_\sigma(\omega)\rangle$ (Eq.(8) in Ref. [34]) reads:

$$
\begin{aligned}
G_\sigma(\omega) =& \frac{1-N_{\bar\sigma}}{\omega-\epsilon_\sigma-\left(S_{02}-\frac{US_{12}}{\omega-\epsilon_\sigma-U-S_{02}-S_{32}}\right)} + \\
& \frac{N_{\bar\sigma}}{\omega-\epsilon_\sigma-U-\left(S_{02}+\frac{US_{22}}{\omega-\epsilon_\sigma-S_{02}-S_{32}}\right)}
\end{aligned}
$$

where

$$
\begin{aligned}
S_{02} &= -i\frac{\Gamma_\sigma}{2} \\
S_{12} &= -i\frac{\Gamma_{\bar\sigma}}{2}\big(f(\omega-\epsilon_\sigma+\epsilon_{\bar\sigma}) + f(\epsilon_{\bar\sigma}+\epsilon_\sigma+U-\omega)\big) \\
S_{22} &= -i\frac{\Gamma_{\bar\sigma}}{2}\big(2 - f(\omega-\epsilon_\sigma+\epsilon_{\bar\sigma}) - f(\epsilon_{\bar\sigma}+\epsilon_\sigma+U-\omega)\big) \\
S_{32} &= -i\Gamma_{\bar\sigma}
\end{aligned}
$$

and where Γ's are the linewidth function defined in Ref.[34]. The authors of Ref.[34] arranged their formula in the above way to demonstrate the resonant levels. Even though the formula produced by SymGF has a less neat form, by simple mathematical rearrangements one can prove that the SymGF result Eq.(3.21) is indeed identical to Eq.(3.22).

The imaginary part of Eq.(3.21) (or Eq.(3.22)) is plotted in Fig.3.2 with occupation numbers $N_\uparrow$ and $N_\downarrow$ as input parameters. The results with a self-consistently determined N_σ is identical with Fig.1 in Ref.[34]. To obtain N_σ, one bears in mind that

$$\begin{aligned} N_\sigma \equiv \langle d_\sigma^\dagger d_\sigma \rangle &= \mathrm{Im}\langle\langle d_\sigma^\dagger(t) d_\sigma(t)\rangle\rangle \\ &= \mathrm{Im}\int \frac{d\omega}{2\pi}\langle\langle d_\sigma^\dagger d_\sigma(\omega)\rangle\rangle \\ &\equiv \mathrm{Im}\int \frac{d\omega}{2\pi} G^<(\omega) \end{aligned} \tag{3.22}$$

where the second and third equations are written in energy space. Therefore, after SymGF symbolically derived the Green's functions and transport formula, to obtain numerical curves one still needs to calculate the occupation numbers. In principle, one should derive another set of EOMs for the lesser Green's function $G^< \equiv \langle\langle d^\dagger d(\omega)\rangle\rangle$. $G^<$ satisfies the Keldysh equation[23]

$$G^< = G^r \Sigma^< G^a \ ,$$

hence solving $G^<$ requires the solution of the lesser self-energy $\Sigma^<$. Here we present a commonly used ansatz reported in Ref.[51] which is suitable for small biases and leads made of good conductors. This ansatz was shown to produce results in qualitative agreement with experiments[52]. The ansatz has the advantage that the current is automatically conserved and it states:

$$\Sigma^{<} = \frac{\Sigma_0^{<}}{\Sigma_0^r - \Sigma_0^a} \left[(G^a)^{-1} - (G^r)^{-1} \right] \ , \tag{3.23}$$

where $\Sigma_0^{<}(\omega) = -\sum_{\alpha=L,R} \left(\Sigma_0^r(\omega) - \Sigma_0^a(\omega) \right) f_\alpha(\omega)$. Here the subscript 0 indicates quantities obtained at interaction strength $U = 0$. In this way, the occupation numbers are obtained self-consistently in the eventual numerical computation of the derived analytical expressions for transport features with reasonable accuracy[51, 52]. In particular, if the system is in equilibrium, *i.e.*, when we calculate transport properties in the zero bias limit, (3.23) reduces to the fluctuation-dissipation theorem[23]

$$G^{<}(\omega) = -2if(\omega)\,\mathrm{Im}[G^r(\omega)] \ ,$$

where $f(\omega)$ is the Fermi distribution function of the system at equilibrium. We shall discuss the feasibility of this way of solving $G^{<}$ in Section 8.3 (Appendix C).

3.6.3 Verification III: Side Coupled Double-Dot at Low Order

In this subsection we present calculations of a side-coupled double quantum dot (DQD) model at the Hartree-Fock level. The device structure is shown in Fig.3.3. This system has been calculated at Hartree-Fock level in Ref.[36] and provides another good test for SymGF. A higher order calculation is presented in the next chapter as it is much more complicated.

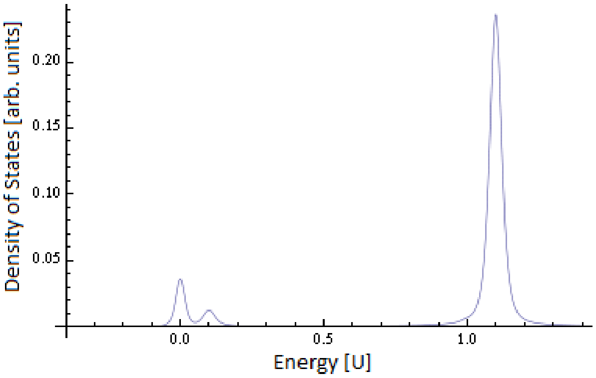

Figure 3.2: Non-self-consistent density of states of central dot with on-site interaction. Wide-band limit approximation is used and symmetric leads are assumed ($t_L = t_R$). Arbitrary units for ordinate. Abscissa in units of U. $t_L = t_R = 0.01U$. Occupation number N_σ is set to 0.5.

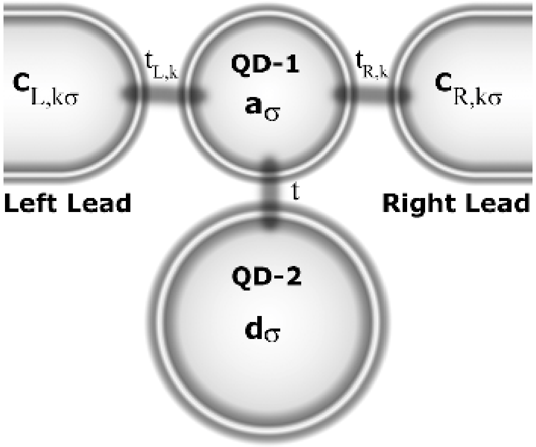

Figure 3.3: The layout of the side-coupled double quantum dot system. There is an on-site interaction U present in the dangling dot QD-2.

The model assumes an interaction-free central dot and a dangling dot coupled to it, with an on-site interaction U inside the dangling dot (see Fig.3.3). The Hamiltonian can be written as

$$\begin{aligned}\hat{H} = &\sum_{\alpha k\sigma} \epsilon_{\alpha k} c^{\dagger}_{\alpha k\sigma} c_{\alpha k\sigma} + \sum_{\sigma} \epsilon_0 a^{\dagger}_{\sigma} a_{\sigma} + \sum_{\sigma} \epsilon_{\sigma} d^{\dagger}_{\sigma} d_{\sigma} \\ &+ \sum_{\alpha k\sigma} \left(t_{\alpha k} c^{\dagger}_{\alpha k\sigma} a_{\sigma} + h.c. \right) + \sum_{\sigma} \left(t a^{\dagger}_{\sigma} d_{\sigma} + h.c \right) \\ &+ U d^{\dagger}_{\uparrow} d_{\uparrow} d^{\dagger}_{\downarrow} d_{\downarrow} \ . \end{aligned} \tag{3.24}$$

Here, the annihilation (creation) operator of electrons in QD-1 is a_σ ($a^\dagger_\sigma$), in QD-2 is d_σ ($d^\dagger_\sigma$), respectively. In the lead labeled by α, it is $c_{\alpha k\sigma}$ ($c^\dagger_{\alpha k\sigma}$) where α can be left or right, k is the continuous quantum number characterizing the leads. The index $\sigma =\uparrow, \downarrow$ represents spin-up and -down channels, respectively. The parameter $t_{\alpha k}$ describes coupling of lead α to QD-1, and t for coupling between the two dots. In this Hamiltonian, parameter U accounts for the on-site interaction strength in QD-2.

Next, the anti-commutators are:

$$\begin{aligned} &\{c_{\alpha k\sigma}, c^{\dagger}_{\beta k'\sigma'}\} = \delta_{\alpha\beta}\delta_{kk'}\delta_{\sigma\sigma'} \\ &\{a_{\sigma}, a^{\dagger}_{\sigma'}\} = \delta_{\sigma\sigma'} \\ &\{d_{\sigma}, d^{\dagger}_{\sigma'}\} = \delta_{\sigma\sigma'} \ , \end{aligned} \tag{3.25}$$

and operators $c_{\alpha k\sigma}$, a_σ and d_σ anti-commute with each other since they correspond to particles living in different regions of the device.

Finally, we specify the truncation rule. Since we are doing a Hartree-Fock calculation, we ask the maximum allowed number of operators of the dangling dot to be 2. Green's functions with extra operators will be truncated in the following way:

$$\begin{aligned} \langle d_\sigma^\dagger d_\sigma O\rangle &\approx N_\sigma^d \langle O\rangle \\ \langle c_{\alpha k\sigma}^\dagger c_{\alpha k'\sigma'} O\rangle &\approx f_\alpha(k)\delta(k-k')\delta(\sigma,\sigma')\langle O\rangle \end{aligned} \tag{3.26}$$

where, again, O represents any sequence of operators. In this way, extra correlations are approximated by the corresponding equal time correlators.

With Rule (3.26), SymGF derived the retarded Green's function of the central dot QD-1 as:

$$G_\sigma^r(w) = -i\sum_\sigma \frac{1}{-w + \frac{1}{-\epsilon_d - N_{\bar\sigma}^d U + w} + \Sigma_L + \Sigma_R}, \tag{3.27}$$

where $\Sigma_{\sigma L}$ and $\Sigma_{\sigma R}$ are the self-energies of left and right lead respectively: $\Sigma_{\sigma\alpha} = -i\pi t_{\alpha k\sigma} t_{\alpha k\sigma}^*$. In the wide-band limit, $\Sigma_{\sigma\alpha}$ is a pure imaginary constant. Eq.(3.27) is a special case of Eq.(3) of Ref.[36] when the on-site interaction of the central quantum dot is zero (since in our QD-1 there is no on-site interaction). This is also a very convincing comparison as the equivalence is exact at this order.

Eq.(3.27) shows that the DOS of spin state σ in QD-1 is related to the occupation number $N_{\bar\sigma}^d$ of the state in QD-2 having opposite spin ($\sigma =\uparrow,\downarrow; \bar\sigma =\downarrow,\uparrow$). Hence, when $N_\downarrow^d$ and $N_\uparrow^d$ of QD-2 are different, DOS of spin states in QD-1 are also different. That is why there are two curves in Fig.3.4. Each curve has two peaks corresponding to bonding and anti-bonding states due to the coupling of the two dots, *i.e.* the hybridization of ϵ_0 and ϵ_d. There is a

DOS dip between the two peaks - going all the way to zero, indicating an anti-resonance behavior. For transmissive systems, anti-resonance is indeed often seen[35, 36, 37, 53, 54, 55, 56]. In a electron density calculation of a molecular system of the same layout (replace quantum dots here with molecules) presented by Mark Ratner at Universite de Montreal, we can see almost all the non-zero density of electrons are on the central molecules and none on the connection to the leads. When the on-site interaction U of QD-2 is zero, the anti-resonance occurs exactly at ϵ_d. The effect of U at the Hartree-Fock level is to shift this anti-resonance by an amount of $N^d_{\bar{\sigma}} U$ as seen in the denominator of Eq.(3.27). This picture is clearly observed in Fig.3.4 where the dip shifts by the value of $N^d_{\bar{\sigma}} U$. The figures of DOS have the same features as that of Fig.2 in Ref.[36].

When calculating the conductance of the DQD system, contributions from both spin channels are summed hence there will be two dips in the conductance curve, as we shall see later.

Next, we shall calculate the equilibrium conductance according to Eq.(2.4). In the numerical computation, we apply the wide-band limit (WBL) approximation[23, 38] such that the coupling parameters $t_{\alpha k \sigma}$ and t are assumed to be energy-independent and the real part of the self-energies due to the device leads are neglected. WBL approximation amounts to neglecting the electronic structure of the device leads by assuming constant DOS and constant coupling to the central device. For leads made of metals as is the case for many experimental situations, the DOS of the leads around the Fermi level do not vary significantly

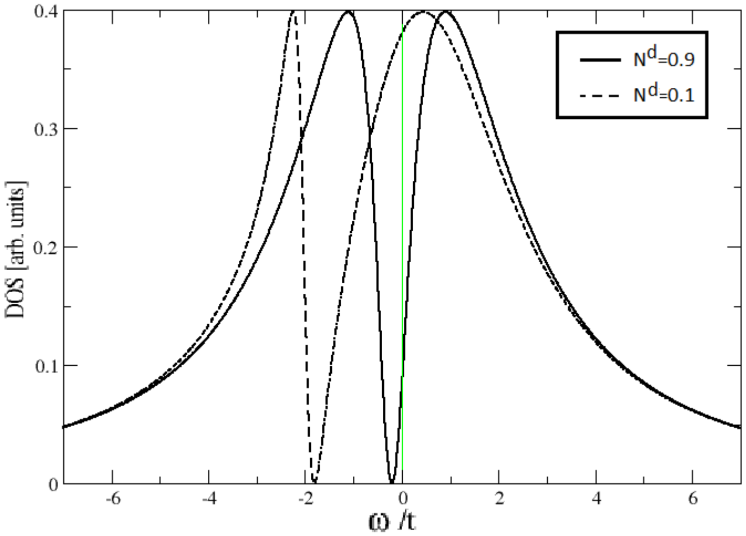

Figure 3.4: Density of states (DOS) in QD-1 versus energy obtained at Hartree-Fock level with $U = 2t$ and $\epsilon_d = -2t$. Wide-band limit approximation is used. Solid line (with its dip on the right) is for $N_\uparrow^d = 0.9$; dashed line (with its dip on the left) is for $N_\downarrow^d = 0.1$.

so that WBL is a reasonable approximation. Discussions about WBL is elaborated in Ref.[38]. We emphasize that WBL is only used during the numerical computation while SymGF does not assume WBL when formulas are derived.

Involved in the retarded Green's function is the occupation number N_σ^d, and we resort to the fluctuation-dissipation theorem for its self-consistent solution. Fig.3.5 shows the self-consistently calculated occupation number N_σ^d of QD-2 as a function of ϵ_d. Fig.3.5(a,b) are for $U = 5t$ and $U = 1.3t$ respectively. When $U \gg 1.5t$ and $\epsilon_d < -U$, both spin-up and spin-down states are well occupied as shown in Fig.3.5(a) and $N_\uparrow^d = N_\downarrow^d$. When ϵ_d is between $-U$ and the Fermi level of the leads, the occupation numbers of the two spin states differ: only one state is well occupied while the occupation of the other state

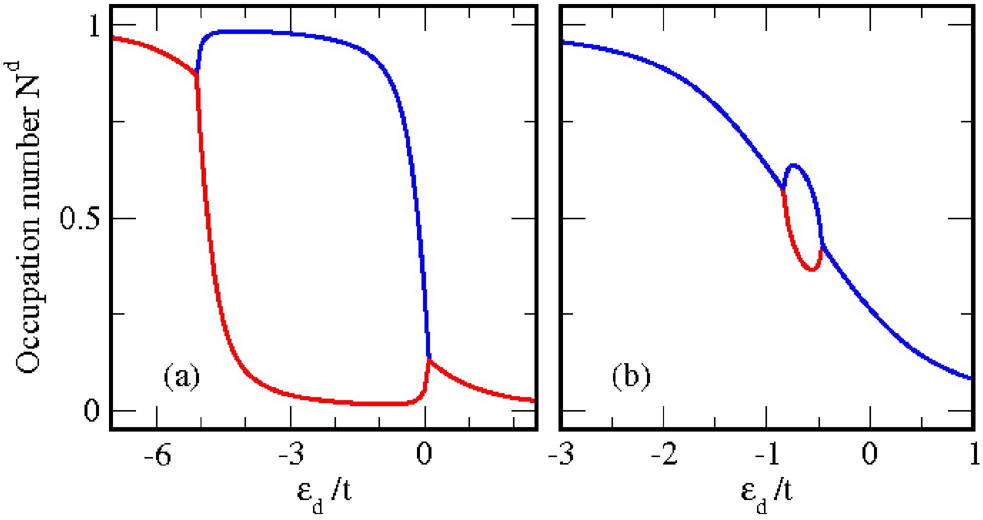

Figure 3.5: Occupation number N_σ^d of QD-2 as a function of ϵ_d at temperature $T = 0.1t$. U is set to be: (a) $U = 5t$ and (b) $U = 1.3t$. The two lines in each sub-figure represent spin-up and spin-down.

rapidly drops. This is expected because in this case, $\epsilon_d + U > E_f$. Finally when $\epsilon_d > E_f$, $N_\uparrow^d = N_\downarrow^d$ again but taking low values. In Fig.3.5(b), N_σ^d is plotted for smaller $U = 1.3t$: the region of $N_\uparrow^d, N_\downarrow^d$ splitting is significantly narrowed and the maximum difference between them is much smaller. Reducing U further, the splitting disappears. The splitting between $N_\uparrow^d, N_\downarrow^d$ has consequences in conductance at the Hartree-Fock level, as shown below. We confirm that this splitting is just a low order effect, in reality or higher order calculation, the spin splitting does not exist.

Conductance is obtained from Eq.(2.4). Fig.3.6(a) shows the total conductance of the DQD. Fig.3.6(b,c) are the conductances of the spin-up and spin-down channels, versus ϵ_d. These are obtained at the HF level. For $U \geq 1.5t$ and

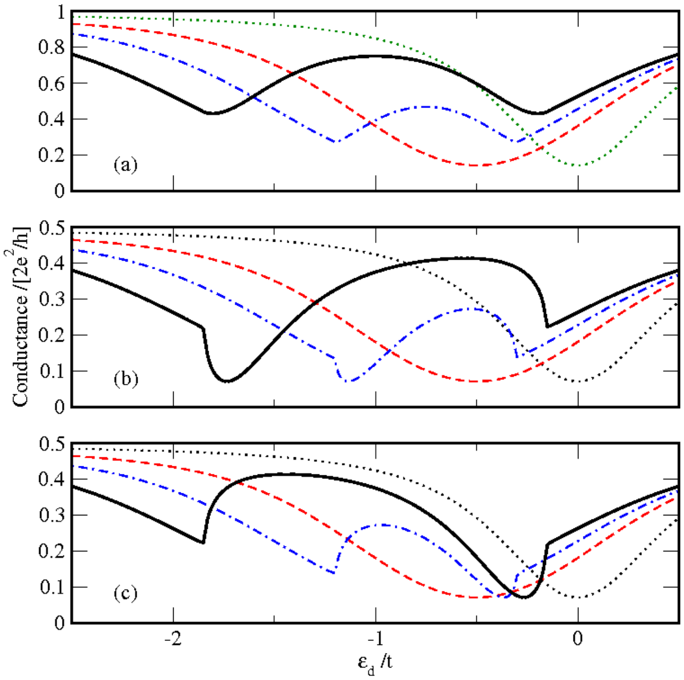

Figure 3.6: (a) Zero-bias total conductance obtained from HF formula as a function of ϵ_d with various U. (b) Conductance of spin-up channel; (c) conductance of spin-down channel. (b,c) add up to (a). For all plots, the dotted lines are for $U = 0$, the dashed lines are for $U = t$, the dash-dotted lines for $U = 1.5t$, and thick solid lines for $U = 2t$. When $U = 0$, the Hartree-Fock formula reduces to the exact results. For all curves the temperature is set at $T = 0.1t$. For large U, the curves have two dips in (a).

due to the splitting of $N^d_\uparrow, N^d_\downarrow$ (see Fig.3.4), the total conductance curve has two dips having equal depth. Each dip is contributed by one spin channel. When U is small, for example $U = t$ (dashed line in Fig.3.6), the conductance of both spin channels are equal hence they add up to a total conductance having only one dip. This is because at $U = t$, there is no splitting in $N^d_\uparrow, N^d_\downarrow$. Note, however, spin dependent conductance is only a feature of low order approximation, and it disappears in the higher order results as expected (see Chapter 4).

3.7 Summary

In this chapter we presented the ideas behind the implementation of SymGF. It is essentially a tool that automatically derives the EOMs and automatically solves them. While deriving the EOMs is not very complicated, solving them is quite difficult since we wish to go to arbitrary levels of correlations. We have implemented several methods, direct iteration, graph-aided solution, conditioned iteraction and, most elegantly, the Gaussian elimination of block matrices. We have tested SymGF against solved systems and three such verifications were presented in this chapter. We have also applied SymGF to more complicated verifications, in particular to a magnetic tunnel junction where an interacting quantum dot is contacted by two ferromagnetic electrodes[33], for this problem analytical formula were derived to reveal the Kondo resonance[33]. Again, SymGF produced exactly the same expressions for the Green's functions. These verifications strongly suggest that SymGF is reliable. Finally, we mention that while SymGF is developed to solve quantum transport problems, it cannot tell if the input Hamiltonian is for transport or not. This means the applicability of this symbolic should be much wider than just transport theory as long as the Hamiltonian of the system can be represented by Anderson model.

4

Quantum Transport in Side-Coupled Double Quantum Dots

In this chapter we present higher order calculations of the T-shaped double quantum dot (DQD) with on-site interaction on the dangling quantum dot shown in Fig.3.3. We already analyzed this device at the Hartree-Fock level in Section 3.6. Using SymGF, we can easily derive formulas to the order of correlation high enough to reveal the Kondo resonance[7].

Kondo effect is named after Jun Kondo[18] for his pioneering work on explaining an abnormal conductance trend of certain materials at low temperatures. The key idea is that a spin-impurity exist in a bulk material and couples to the rest of the material. So when the temperaturs is low enough to allow multiple quantum transitions, this extra coupling increases the resistance of the material. In quantum dot transport, people have borrowed this term to describe the high order co-tunneling process that takes place for some situations where interaction is present. Fig.4.3 sketches the process featuring Kondo effect. Later in this section we'll see high order transitions not between the central dot and the leads like those in Fig.4.3, but between the two quantum dots of consideration, which is also seen as a Kondo effect.

Both theoretical and experimental attentions have been devoted to quantum trasport in various double quantum dot (DQD) [57, 58, 59, 5, 1, 60, 61, 62, 63, 64, 65, 66, 67] in recent years. The quantum transport system we investigate in Fig.3.3 features a T-shaped DQD device where QD-1 directly couples to the device leads while QD-2 does not and has a strong on-site interaction energy U. Experimentally, conductance through a DQD having a central dot with a side-coupled dot, was reported in Ref.[5]. The measured transport features were attributed to a Fano-Kondo interplay and, by tuning gate voltages, alternating Kondo valley and non-Kondo valley in the conductance curve was observed[5]. Another interesting device was reported in Ref.[1] where a quantum dot was side-coupled to a quantum wire and conductance of the wire was measured. Here the conductance features were attributed to the Fano-Kondo antiresonance. On the theoretical side, side-coupled DQD systems with strong interaction on the side (dangling) dot (Fig.3.3) or on both dots, have received considerable interest by numerical renormalization group (NRG)[60, 61, 62] and slave-boson analysis[63, 64, 65, 66, 67]. The NRG method is best reviewed in Refs.[2, 68]. This method is intrinsically numerical but inherently non-perturbative. It has successfully solved Kondo effect both in low temperature and high temperature situation. But again, like all other methods, when the system is more complicated, for example when we include more quantum dots in our calculation, it could be really tedious to apply. Also, since we wish to obtain analytic formulas in order to get a clear physical picture of the high order transitions, we only briefly mention this method and focus on equation of motion method implemented in SymGF. The NRG analysis of Ref.[60] investigated the spectral density of a side-coupled double dot system as a function of inter-dot coupling, where the Kondo singlet ground state is preserved. Ref.[61] analyzed a similar DQD having strong interactions in both dots with NRG, focusing on the temperature dependence of the conductance and proposing a possible explanation to the experiment of Ref.[5]. Ref.[62] investigated the DQD with spin-spin interaction using NRG. In contrast to NRG, the slave-boson approximation was adopted mainly for its simplicity in dealing with DQD[63, 64, 65, 66, 67]. Finally, even though the EOM method has been successfully applied to analyzing quantum transport in many different systems, its application to the DQD device has been limited to lower order (of EQM iteration) than what is required to reveal the Kondo effect[35, 36]. Investigating DQD device with the lower order EOM, Ref.[35, 36] showed a strong anti-resonance, where there is an energy point where the density of states is exactly zero, in comparison with a peak splitting. Anti-resonance was also found in other systems[37, 53, 54, 55] where slave-boson or tight-binding methods are used.

Using SymGF which analytically pushes EOM to higher order, we have investigated the Kondo effect of the T-shaped DQD of Fig.3.3 where QD-1 directly couples to the device leads but the strong on-site interaction U only exists in QD-2. The higher order results show significant differences in quantum transport properties of the DQD device as compared with the lower order analysis. Interesting and rich transport features are revealed including the Kondo resonance, Fano line-shape, anti-resonance, destruction of anti-resonance, etc.. From the analytical form of derived Green's functions, one can identify microscopic processes which contribute to the Kondo resonance. The results obtained by SymGF are compared to the experiments[5, 1], qualitative consistency is obtained and good quantitative agreement can also be achieved by using a reasonable set of device parameters.

At appropriate order of correlations, SymGF derives Green's functions that reveal the Kondo effect for the DQD system. The Hamiltonian of this system is given in Eq.(3.24). The list of anti-commutators is in Eq.(3.25). The only change in the input to SymGF is the truncation rule, which is:

$$\langle d_\sigma^\dagger d_\sigma O\rangle \approx N_\sigma^d \langle O\rangle \tag{4.1}$$

$$\langle a_\sigma^\dagger a_\sigma O\rangle \approx N_\sigma^a \langle O\rangle \tag{4.2}$$

$$\langle c_{\alpha k\sigma}^\dagger c_{\alpha k'\sigma'} O\rangle \approx f_\alpha(k)\delta(k-k')\delta(\sigma,\sigma')\langle O\rangle \tag{4.3}$$

where the maximum allowed number of operators of the dangling dot (QD-2,d_σ and $d_\sigma^\dagger$) is increased to 3. Because of the higher order truncation, the total number of EOMs is now 133 - meaning there are 133 different Green's functions derived by SymGF. For simplicity, we denote them by G_i, where i is the serial number that SymGF assigned to them when they are derived. Among the 133 Green's functions, two of them have been identified to embody the Kondo effect. The lengthy formulas are listed in the Appendix. Pleasantly, for the DQD

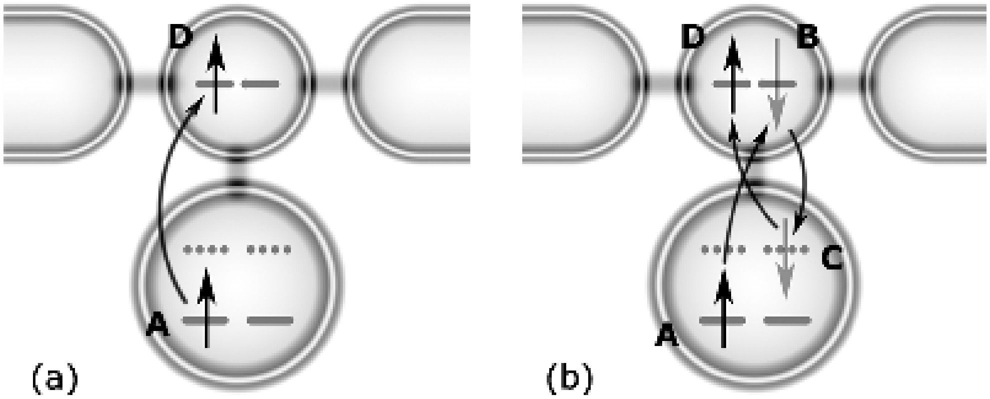

Figure 4.1: (a) Transition of a spin-up electron from QD-2 to QD-1 as indicated from A to D. (b) One of the possible transition processes (terms in the higher order formula) that starts from A and ends at D: the spin-up electron "jumps" from A to B, to C, and finally to D, during which spin-flips are involved. The transitions from A to B and from B to C are virtual processes as they occur simultaneously. States involved in virtual processes are denoted by grey arrows.

problem reported here, all the analytical formula were derived symbolically by SymGF in less than two minutes on a desktop computer.

4.1 High Order Correlation Processes

Among the 133 Green's function that SymGF has derived (see beginning Eq.(8.32) in the Appendix for the final result these equations generate), two can be immediately identified to be related to the Kondo effect. They are:

$$G_{86} = \langle\langle \hat{a}_{\downarrow}\hat{a}^{\dagger}_{\downarrow}\hat{d}_{\uparrow}\hat{d}_{\downarrow}\hat{d}^{\dagger}_{\downarrow}, \hat{a}^{\dagger}_{\uparrow}\rangle\rangle \tag{4.4}$$

$$G_{127} = \langle\langle \hat{a}_{\uparrow}\hat{a}^{\dagger}_{\uparrow}\hat{d}_{\uparrow}\hat{d}_{\downarrow}\hat{d}^{\dagger}_{\downarrow}, \hat{a}^{\dagger}_{\uparrow}\rangle\rangle. \tag{4.5}$$

Fig.(4.1) shows the process described by G_{86}, where the virtual process involves the simultaneous transition from QD-2 to QD-1 and from QD-1 to QD-2, featuring a co-tunneling process.

Since the total number of $\hat{a}$ and $\hat{a}^\dagger$ in G_{86} (and in G_{127}) is three, according to the truncation rule (4.1), it is approximated by:

$$G_{86} \approx (1 - N^a_\downarrow)\langle\langle \hat{d}_\uparrow \hat{d}_\downarrow \hat{d}^\dagger_\downarrow, \hat{a}^\dagger_\uparrow\rangle\rangle$$

$$G_{127} \approx (1 - N^a_\uparrow)\langle\langle \hat{d}_\uparrow \hat{d}_\downarrow \hat{d}^\dagger_\downarrow, \hat{a}^\dagger_\uparrow\rangle\rangle$$

so that the probability amplitude of the process described by, for example Fig.4.1, is obtained by the product of the probability amplitude of a lower order process and the occupation number. This is a mean-field approximation.

We shall apply the wide-band limit approximation (WBL) to reduce the above equation further. WBL entails to neglecting the electronic structure of the electrodes which is reasonable for electrodes made of good metal whose DOS has weak dependence on the energy. For our problem this means setting $t_{l,r}(k) = t_{l,r}$ =constant. Denoting $\Gamma_{LD} \equiv \pi\left(t_l^2 + t_r^2\right)$ and using WBL, the final expressions become:

$$\begin{aligned} G_{86} &= \frac{(1 - N^a_\downarrow) t g_5 \left(\left(G_6 - G_7\right)\left(1 + i\Gamma_{LD}\right) - (1 - N^a_\downarrow) t^2 g_2 G_1 \right)}{1 - t^2 \left(1 + (1 - N^a_\downarrow) U g_2\right) g_5 + i\Gamma_{LD}} \\ G_{127} &= \frac{(1 - N^a_\uparrow) t g_5 \left(\left(G_6 - G_7\right)\left(1 + i\Gamma_{LD}\right) - (1 - N^a_\downarrow) t^2 g_2 G_1 \right)}{1 - t^2 \left(1 + (1 - N^a_\downarrow) U g_2\right) g_5 + i\Gamma_{LD}} \quad , \end{aligned} \tag{4.6}$$

where G_1, G_6, G_7, g_2 and g_5 are presented in the Appendix in Eqs.(8.32, 8.33, 8.34, 8.35) and (8.39, 8.40). The probability amplitude provided by (4.6) gives

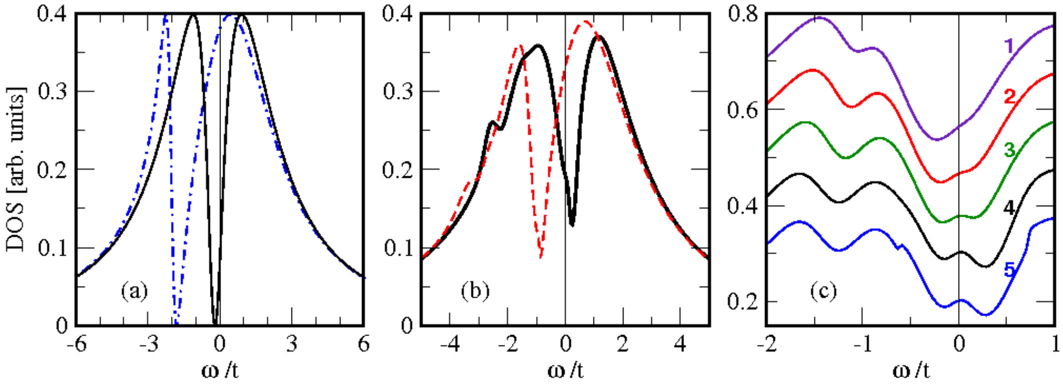

Figure 4.2: Density of states (DOS) in QD-1 versus energy. (a) DOS obtained at Hartree-Fock level with $U = 2t$ and $\epsilon_d = -2t$. Solid line is for $N^d_\uparrow = 0.9$, dash-dotted line is for $N^d_\downarrow = 0.1$. (b) DOS obtained with higher order formula at temperature $T = 0.1t$. Solid line, $U = 2t$ and $\epsilon_d = -2t$; dashed line, $U = 2t$ and $\epsilon_d = -3t$. The occupation numbers N^a_σ and N^d_σ are calculated self-consistently. (c) DOS obtained with higher order formula at various temperatures. For all curves, $U = t$ and $\epsilon_d = -1.05t$. From line 1 to line 5, $T = 2t$, t, $0.5t$, $0.1t$ and $0.01t$. Except line 5 ($T = 0.01t$), line 1-4 are consecutively shifted upward by 0.1 for clarity. The Kondo peaks found in line 3,4 and 5 (at $\omega = -0.6t$ and 0 in line 5, and at $\omega = 0$ in lines 3 and 4) disappear above the Kondo Temperature T_K predicted by Refs.[1, 2, 3, 4].

rise to the Kondo peaks that we will show later. These Kondo peaks manifest themselves because they are absent in a lower order calculation.

4.2 The Density of States

Fig.4.2(b,c) plot DOS at higher order approximations and N^d_σ is calculated self-consistently by Eq.(3.22). They are qualitatively different from the Hartree-Fock (HF) result of Fig.4.2(a), which is a reproduction of Fig.(3.4). In Fig.4.2(b), we set temperature $T = 0.1t$. The solid line is for $U = 2t$ and $\epsilon_d = -2t$; dashed line for $U = 2t$ and $\epsilon_d = -3t$; dash-dotted line for $U = 5t$ and $\epsilon_d = -2t$. Now, there are three peaks in DOS instead of two (in the HF result). The solid line, obtained using the same U and ϵ_d as that of HF (*i.e.* Fig.4.2(a)), has DOS peaks at energy $\omega = -2.50t$, $\omega = -0.95t$ and $\omega = 1.15t$.

To understand these peak positions, we may consider a simple tight-binding model having three levels at ϵ_0, ϵ_d and $\epsilon_d + U$. For the DQD structure, ϵ_0 and ϵ_d are coupled by parameter t, and no coupling between ϵ_d and $\epsilon_d + U$. The tight-binding Hamiltonian is therefore,

$$\begin{pmatrix} \epsilon_0 & t & t \\ t & \epsilon_d & 0 \\ t & 0 & \epsilon_d + U \end{pmatrix} .$$

When $\epsilon_d = -2t$ and $U = 2t$, the eigen-values of this tight-binding model are found to be (by direct diagonalization) $-2.48t$, $-0.69t$ and $1.17t$. These values agree fairly well with the peak positions of Fig.4.2(b). This simple analysis neglects the left and right leads: when leads are present, the peak positions are slightly different from these eigen-values. The tight-binding analysis suggests that the curves in Fig.4.2(b) result from hybridization of three levels: ϵ_0, ϵ_d and $\epsilon_d + U$. We also found that the higher order DOS is almost independent of spin, very different from the HF results where there is a spin-dependence through N_σ^d. This spin independence is because the Hamiltonian Eq.(3.24) is symmetric with respect to σ and there is no symmetry breaking factors. The higher order approximation preserves this symmetry but HF does not.

Importantly, the anti-resonance dips in the DOS of Fig.4.2(b) become non-zero. To understand this feature, let's consider transition of a spin-up electron from QD-2 to QD-1, *i.e.* from A to D in Fig.4.1(a). In the higher order formula derived by SymGF, there are many terms representing such transitions. In addition to a direct transition, there are two terms involving more complicated transitions, i.e. Eqs.(4.4, 4.5) in Section 4.1. Fig.4.1(b) shows the physical meaning of Eq.(4.4) where the transition is from A to B, to C, and finally to D. Part of this process is virtual, *e.g.* from A to B and from B to C, where the electron occurs at A, B and C at the *same* time (thus virtual). Adding up all such virtual processes coherently, the transition from A to D is broadened and the anti-resonance dip is therefore smeared.

Another new feature in the higher order approximation is shown in Fig.4.2(c) which plots five DOS curves at temperatures $T = 2t$, t, $0.5t$, $0.1t$ and $0.01t$ (labeled 1 to 5, vertically shifted for clarity), with $U = t$ and $\epsilon_d = -1.05t$. In all the curves, we found that the three higher peaks located near $\omega = -1.5t, -0.8t$ and t, can be well estimated using the tight-binding model above. At low temperatures, there are one or two extra small peaks at $\omega \sim -0.6t$ (in curve 5) and/or $\omega \sim 0$ (curves 3,4,5). These extra peaks cannot be explained by the tight binding model of hybridization of the energy levels ϵ_0, ϵ_d and $\epsilon_d + U$. There are two main features of the extra peak. First, its appearance is sensitive to the value of parameters and is only possible when higher order processes are taken into account. Second, the extra peak is sensitive to temperature, it disappears when temperature is increased. By examining the higher order formula derived by SymGF (see Section 4.1, Eq.(4.4, 4.5)), the extra peaks are contributed by summing up various higher order virtual processes similar to that

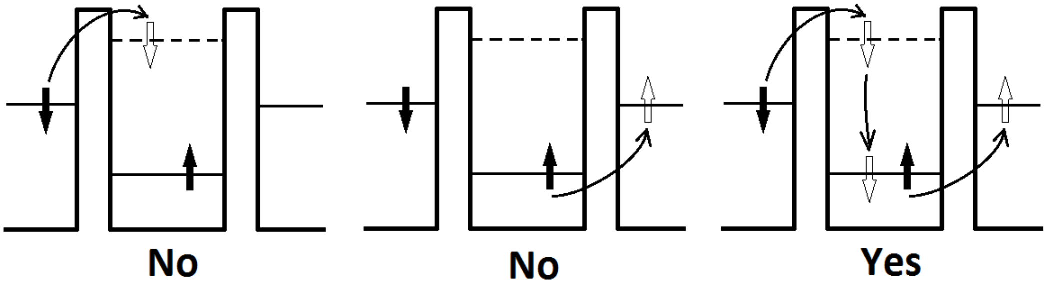

Figure 4.3: Kondo effect in the single dot tranport system. When interaction is present, electrons in the left lead and quantum dot (denoted by solid arrows) can't hop into the quantum dot or the right lead, respectively, because that requires energy. However, if both electrons hop simultaneously, then the whole process conserves energy and thus make it possible to create a current from left to right lead. This is a high order co-tunneling process.

shown in Fig.4.1. These behaviors are features of the Kondo resonance and the extra peaks are the Kondo peaks in the present DQD system.

For a single QD contacted by two leads, the Kondo effect is induced by high order co-tunneling processes taking place between the leads and the QD[69, 70, 71]. In Fig.4.3 we sketch the physical picture of the Kondo effect in single QD contacted by two leads. The electron inside the QD can't hop up into the right lead as Fermi level of the right lead is higher than its own energy; and the electron in the left lead can't jump into the QD as it has to occupy a higher energy level due to the existence of on-site interaction. But they can hop simultaneously, i.e., the electron in left lead jumps into the QD and meanwhile the electron inside the QD hops into the right lead. This co-tunneling process, called Kondo resonance, conserves the total energy and could happen[72]. For our DQD system, the high order co-tunneling process occurs between QD-1 and QD-2 as illustrated in Fig.4.1. The Kondo temperature for a single impu-

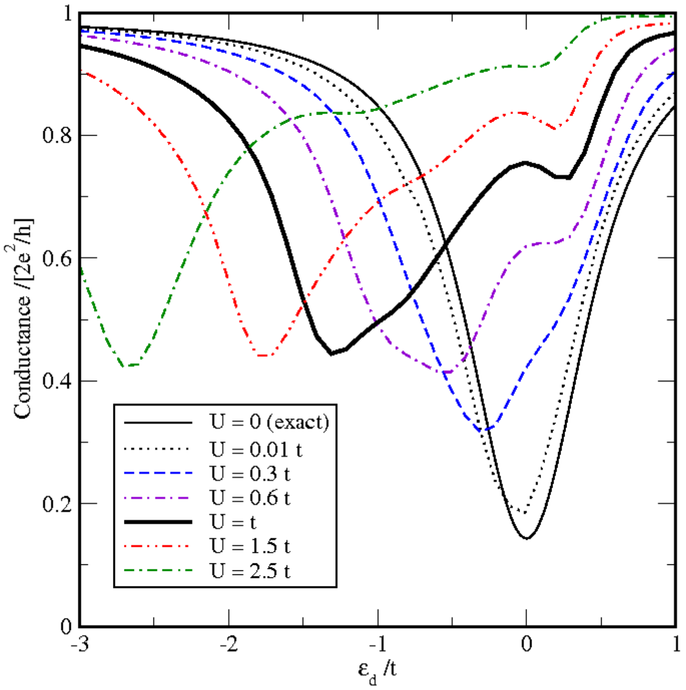

Figure 4.4: Zero-bias conductance obtained from high-order formula as a function of ϵ_d at temperature $T = 0.1t$ for various U.

rity Anderson model can be estimated by the following expression[1, 2, 3, 4], $T_K = \sqrt{\Gamma U} exp\left[\pi\epsilon_d(\epsilon_d + U)/\Gamma U\right]/2$, which was originally obtained with NRG for single-dot coupled to two leads, and where Γ describes the coupling between the QD and the leads. For the T-shaped DQD system, we use the coupling between QD-1 and QD-2 as Γ to estimate a Kondo temperature, namely $\Gamma \sim 2\pi t^2$. For $\epsilon_d = -1.05t$ and $U = t$ (used in Fig.4.2(c)), we obtain $T_K = 1.29t$. Indeed, Fig.4.2(c) shows that the Kondo peaks vanish when temperature exceeds this scale.

4.3 The Conductance

Fig.4.4 shows the total conductance obtained from higher order formula at temperature $T = 0.1t$ and for different values of U. As discussed in the previous section , higher order analysis preserves the symmetry of DOS with respect to spin index σ, the conductance of both spin channels are the same. Several observations are in order. First, as U is reduced, the conductance approaches the exact result obtained at $U = 0$. Second, when ϵ_d and $\epsilon_d + U$ are both far from E_f, the transition of electrons between the two QDs is reduced. As a result, QD-1 is not affected by the presence of QD-2, consequently the conductance of the system recovers the unit value $G_0 \equiv 2e^2/h$. Third, each conductance curve has a dip located slightly below or at $\epsilon_d = -U$. Fourth, when U is between $0.6t$ and $2.5t$, the conductance develops another smaller dip just above $E_f = 0$ (for instance the thick solid line for $U = t$ in Fig.4.4). The dips originate from the corresponding DOS.

By lowering the temperature further, the Kondo features of Fig.4.2(c) appear in the conductance. Fig.4.5 compares the conductance at $T = 0.1t$ (the dashed line) and very low temperature $T = 0.01t$ (the solid line). We observe that at $T = 0.01t$, two extra peaks due to Kondo effect appear at $\epsilon_d = -1.05t$ (peak X) and $\epsilon_d = -0.53t$ (peak Y), which correspond to the Kondo peaks in the DOS (curve 5 in Fig.4.2(c)). At $T = 0.1t$, while the Kondo peak in DOS can be seen (curve 4 in Fig.4.2(c)), it can be barely discerned in the dashed line of Fig.4.5 near $\epsilon_d = -1.05t$.

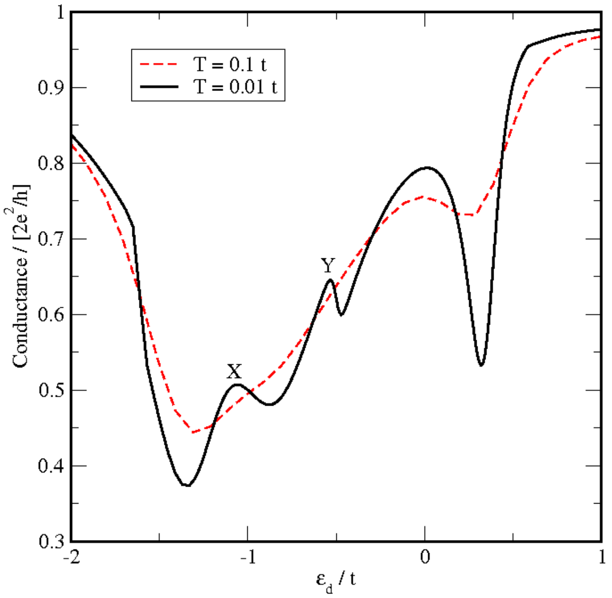

Figure 4.5: Conductance at low temperature showing the Kondo effect. Both curves have $U = t$. $T = 0.1t$ for the dashed line, $T = 0.01t$ for the solid line. The Kondo peaks are seen in the $T = 0.01t$ curve as indicated by “X” and “Y”.

4.4 Comparison with Experimental Results

We can compare our results with experimental measurements reported in Refs.[5, 1]. Qualitatively, the experimental data[5, 1] show both Fano[73] and Kondo features which can be reproduced in our calculation. Fano effect can be viewed as the coupling effect of a discrete energy level to a continuous spectrum, whose main feature is an asymmetric line shape which originates from the electron occupation in the continuous spectrum. In the experiment of [1], the device was a quantum wire with a side coupled QD. Even though it has only one QD, our DQD system approaches it when QD-1 is very well coupled to the leads. As clearly stated in [1], the region marked by symbol “A” in Fig.1 of Ref.[1] and the data in Fig.3 of Ref.[1] corresponds to the case of a single energy level in their QD, which is our case analyzed here. In Fig.4.6(a) we plot the calculated conductance curve versus level position which was adjusted by a gate voltage in the experiment[1]. The result is very well consistent with the $750mK$ curve in Fig.3(a) of Ref.[1]: the maximum difference between the theory result and the experimental data is about 20%. Notably, the parameters used in our calculation [1] are quite close to those suggested in Ref.[1]. The comparison suggests that changing the gate voltage V_g in the experiment by $0.01V$ (horizontal axis of Fig.3(a) in Ref.[1]) corresponds to changing the energy level of the side-coupled dot in our theory by $0.11meV$, indicating a gate efficiency of 1.1% which is a very reasonable value in experimental measurements. Importantly, Fig.4 of Ref.[1] demonstrates that there is no spin splitting of the conductance dip at zero magnetic field. Our higher order analysis, as stated above, agrees with this observation. In contrast, HF results would give a spin splitting as shown Fig.3.6.

Experimentally, Sasaki et al.[5] measured the conductance of a DQD system similar to that of Fig.3.3 analyzed here. In Fig.4.6(b) we plot the calculated

---

[1] To compare with the experimental curve (the 750meV curve) in Figure.3(a) of [1], we set interaction $U = 0.64meV$ which is within 20% to the experimentally reported range; dot-dot coupling linewidth function $\Gamma = 2\pi t^2 = 4meV$, lead-dot coupling linewidth function $\Gamma_{LD} = \sum_k 2\pi t_{Lk}^2 = 1.6meV$, and the energy level of QD-1 $\epsilon_0 = -3.36meV$. We choose the value of ϵ_0 such that the conductance of the wire is the same as that of the experimental conductance far from resonance, which is $1.8e^2/h$ (see lowest curve of Figure.1 in [1]). In this limit, our DQD transport approaches the single QD device[1].

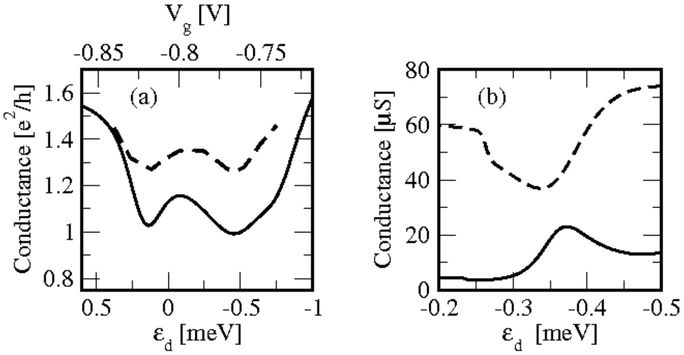

Figure 4.6: Conductance versus ϵ_d of QD-2. (a) The dashed line is reproduced from the top curve (temperature $T = 750$mK) in Fig.3(a) of [1] and its abscissa is plotted on the top. The solid line is produced by SymGF; its abscissa is plotted at the bottom. The parameters of the solid line are: $U = 0.64meV$, $\Gamma \equiv 2\pi t^2 = 4meV$, $\Gamma_{LD} \equiv \sum_k 2\pi t_{Lk}^2 = 1.6meV$, $\epsilon_0 = -3.36meV$, and temperature $T = 750$mK. The maximum difference between these two lines are about $0.25e^2/h$ at $\epsilon_d = -0.5meV$ or $V_g = -0.76V$. (b) Both curves are produced by SymGF. The parameters for the solid line are: $\Gamma = 5.5meV$, $\Gamma_{LD} = 0.14meV$, $\epsilon_0 = -0.53meV$, $U = 0.35meV$, and temperature $T = 41mK$; the parameters for the dashed line are: $\Gamma_{LD} = 0.89meV$, $\epsilon_0 = -0.35meV$, and the rest are the same as the solid line. This curve qualitatively agrees with the experimental data in Fig.2(a,b) of [5].

conductance curves to compare with the experimental data of [5]. In particular, the solid and dashed lines of Fig.4.6(b) correspond to Fig.2(a,b) of Ref.[5]. Our results agree with the experimental data qualitatively. In the experiment[5], the conductance peak can be changed to a conductance dip (Fig.2(a) to Fig.2(b) in Ref.[5]) by lowering the gate voltage that controls the energy level of QD-1. Lowering gate voltage effectively raises the energy level ϵ_0 of QD-1. Indeed, as shown in Fig.4.6, by raising $\epsilon_0 = -0.53$meV to -0.35meV, the peak (solid line) changes to the dip (dashed line) [1].

---

[1] Note that when gate voltage of QD-1 is changed (in the experiment), not only it changes the energy level ϵ_0, it may also change other parameters of the device such as the lead-dot coupling. The two curves in Fig.4.6(b) were obtained using two different lead-dot coupling

4.5 Summary

In this Chapter we presented the first application of SymGF, namely the T-shaped double quantum dot system where there is an on-site interaction on the dangling dot. We have carried out a higher level analysis that reveals the Kondo effect. The results for density of states are compared with an isolated tight-binding model and demonstrated strong interacting nature of the transport system. Rich physics is revealed by SymGF. Besides Kondo effect, we observed Fano line shape, anti-resonance and destruction of anti-resonance, etc. With the analytical expressions derived by SymGF, we can identify the terms that contribute to the Kondo effect: vivid physical picture of the transition processes can be directly and clearly seen by these terms. To the best of our knowledge, no one has reported higher order correlation results for this system, and we resort to the comparison directly with experiments. Not only qualitative agreement are obtained, but also - with a proper choice of parameters, a reasonable quantitative agreement is achieved.

---

constants as indicated in the figure caption.

5

Single Quantum Dot in Parallel with a Direct Lead-Lead Link

In this chapter we present quantum transport properties of a junction bridged by a single quantum dot in parallel with a direct link, as shown in Fig.5.1. This model is useful for situations where the tunneling process from one lead directly to the other lead is non-negligible, such as in the scanning tunneling microscope (STM) measurements in molecular transport junction of Refs.[39, 40, 74, 75]. This situation may also have been observed in STM tunneling to a single magnetic atom deposited on a metallic surface where asymmetric Fano resonance in the tunneling spectra was reported[76, 77]. Direct coupling between needle tip and substrate may happen if the distance between the sample and needle tip and the distance between substrate and the needle tip are comparable and/or the electronic states in the sample is less conductive than those on the sample. Since the Fano resonance line shape comes from a quantum interference between a discrete and a continuous transition, Fig.5.1 mimics this situation.

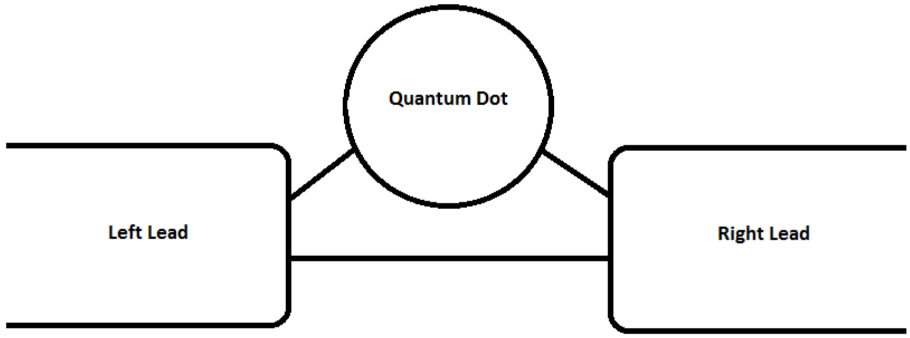

Figure 5.1: Schmetic layout of the transport system with direct lead-lead contact. A quantum dot is coupled to two leads, while there is also direct coupling between the two leads. Couplings are represented by a solid line.

The Hamiltonian of this system is in Eq.(2.5), here we rewrite it here.

$$\begin{aligned}\hat{H} = &\sum_{\sigma} \epsilon\sigma d^{\dagger}_{\sigma} d_{\sigma} + U d^{\dagger}_{\uparrow} d_{\uparrow} d^{\dagger}_{\downarrow} d_{\downarrow} + \sum_{\alpha\sigma k} \epsilon_{\alpha\sigma k} c^{\dagger}_{\alpha\sigma k} c_{\alpha\sigma k} + \\ &\left(\sum_{\alpha\sigma k} t_{\alpha k} c^{\dagger}_{\alpha\sigma k} d_{\sigma} + h.c \right) + \left(\sum_{\sigma k_1 k_2} v_{k_1 k_2} c^{\dagger}_{L\sigma k_1} c_{R\sigma k_2} + h.c. \right) \ , \qquad (5.1)\end{aligned}$$

where $d^{\dagger}_{\sigma}$ and d_{σ} are operators of the central dot. Ref.[78] reported a calculation of transport under the influence of a microwave field without U. Ref.[41] calculated transport both at zero and finite magnetic flux with a Green's function of the central quantum dot that includes an on-site interaction $U \to +\infty$. An infinite U reduces the complexity of theory since it forces half-filling of the energy level of the quantum dot.

We have already presented the current formula corresponding to the Hamiltonian Eq.(5.1) in Section 2.3 [see Eq.(2.7)] with derivation details contained in the Appendix. In this chapter we apply SymGF to obtain the Green's function of the central dot, and then substitute the resulting Green's function into the current formula Eq.(2.7) to obtain the transport properties.

5.1 Hartree-Fock Result

In this section we present results obtained at the Hartree-Fock level. Here we use Eq.(3.23) for an estimate of $G_\sigma^<$. In the analysis, the self-energies contributed from the leads come *only* from the coupling between the leads and the central quantum dot, characterized by the coupling constant t_α. In this way, Eq.(3.23) preserves the current through the channel that contains the central dot, *i.e.*, the upper channel in Fig.5.1.

For this problem at the Hartree-Fock level, we use the following truncation rules:

$$\langle d_\sigma^\dagger d_\sigma O\rangle \approx N_\sigma \langle O\rangle \tag{5.2}$$

$$\langle c_{\alpha\sigma k}^\dagger c_{\alpha\sigma k'} O\rangle \approx f_\alpha(k)\delta_{kk'}\langle O\rangle \tag{5.3}$$

where O represents any sequence of operators. Rule (5.2) is applied whenever the total number of $d_\sigma^\dagger$ or d_σ exceeds 2; rule (5.3) is applied whenever the total number of $c_{\alpha\sigma k}^\dagger$ or $c_{\alpha\sigma k}$ exceeds 1. With these truncation rules, the EOMs are just slightly different from that without the direct lead-lead link, Eq.(2.21).

$$\begin{aligned}
\langle d_\uparrow d_\uparrow^\dagger\rangle &= \frac{1}{\omega-\epsilon_d}\Big(1-U\langle d_\uparrow d_\downarrow d_\downarrow^\dagger d_\uparrow^\dagger\rangle+\sum_k\langle c_{Lk}d_\uparrow^\dagger\rangle t_{Lk}^*+\sum_k\langle c_{Rk}d_\uparrow^\dagger\rangle t_{Rk}^*\Big)\\
\langle d_\uparrow d_\downarrow d_\downarrow^\dagger d_\uparrow^\dagger\rangle &= N_\downarrow^d\langle d_\uparrow d_\uparrow^\dagger\rangle\\
\langle c_{Lk}d_\uparrow^\dagger\rangle &= \frac{1}{\omega-\epsilon_{L\uparrow}}\Big(\sum_{k'}\langle c_{Rk'}d_\uparrow^\dagger\rangle v_{kk'}+\langle d_\uparrow d_\uparrow^\dagger\rangle t_{Lk}\Big)\\
\langle c_{Rk}d_\uparrow^\dagger\rangle &= \frac{1}{\omega-\epsilon_{R\uparrow}}\Big(\sum_{k'}\langle c_{Lk'}d_\uparrow^\dagger\rangle v_{kk'}^*+\langle d_\uparrow d_\uparrow^\dagger\rangle t_{Rk}\Big) \qquad (5.4)
\end{aligned}$$

The EOMs of the other spin channel are obtained by interchanging up- and down-spin. The Green's function of the central dot is derived by SymGF, and found to be:

$$G^r(\omega)=\frac{1}{\omega-(1-N_\downarrow)U-\epsilon_d+\frac{i\pi(t_L^2(\omega)+t_R^2(\omega))}{1+\pi^2v_{\omega,\omega}^2}+\frac{2\pi^2 t_L(\omega)t_R(\omega)v_{\omega,\omega}}{1+\pi^2v_{\omega,\omega}^2}} \qquad (5.5)$$

From this expression we see that the effect of the direct lead-lead link is a shift of the energy level of the central dot weighed by the occupation number.

5.1.1 Density of States

Applying the wide-band limit approximation, the Hartree-Fock DOS are obtained and shown in Figs.5.2 and 5.3 where different curves are for different lead-lead coupling constant v. In Fig.5.2, v changes from 0 to 0.5 in step of 0.1; in Fig.5.3 v changes from 0.4 to 2 in step of 0.4. The coupling between the central dot and the leads are made symmetric, $t_L = t_R$, and we use t_α as the energy unit in these figures. We see from the figure and the expression of the central dot Green's function Eq.(5.5), that at energy $\omega = \epsilon + (1 - N_\sigma)U$,

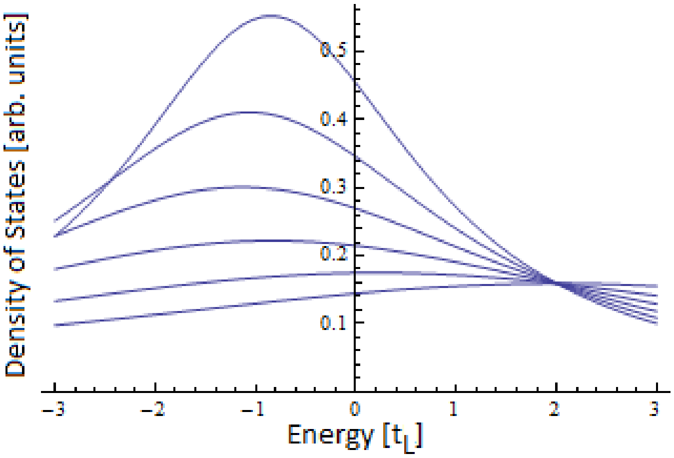

Figure 5.2: Density of states of the central quantum dot. Wide-band limit approximation is used. We assumed symmetric lead-dot coupling ($t_L = t_R$) and t_L is used as the energy unit. At energy 0, from bottom up, the curves' $v = 0, 0.1, 0.2, 0.3, 0.4, 0.5 t_L$, respectively. The energy level of the central quantum dot ϵ_d is chosen to be 0 and $(1 - N_\sigma)U$ is chosen to be 2.

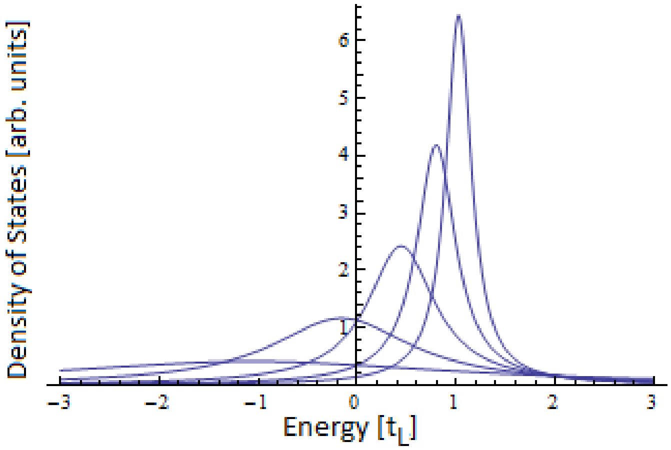

Figure 5.3: Density of states of the central quantum dot. Wide-band limit approximation is used. We assumed symmetric lead-dot coupling ($t_L = t_R$) and t_L is used as the energy unit. The curve with lowest peak height has $v = 0.4 t_L$, second loweset has $v = 0.8 t_L$, third $v = 1.2 t_L$, fourth $v = 1.6 t_L$ and finally the curve with the highest and sharpest peak as $v = 2 t_L$. The energy level of the central quantum dot ϵ_d is chosen to be 0 and $(1 - N_\sigma)U$ is chosen to be $2 t_L$.

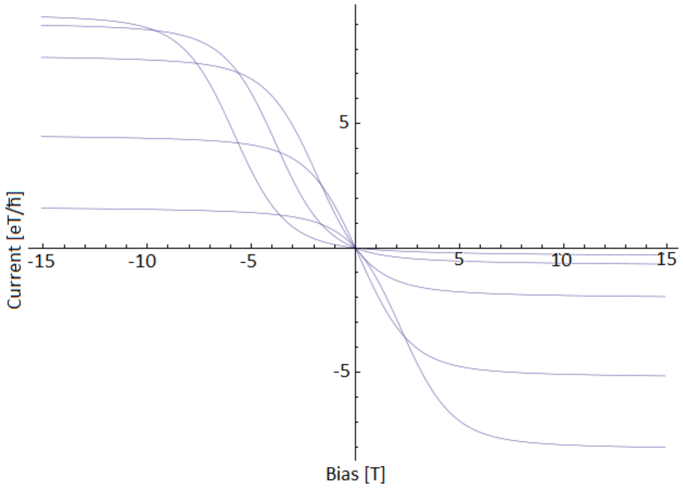

Figure 5.4: Current of the left lead as a function of the bias applied to left lead. The temperature T sets the energy unit. At lowest bias, the curves are obtained (from top to bottom) at $\epsilon_d = -4, -2, 0, 2, 4T$. The lead-dot coupling constants $t_\alpha = T$.

the DOS is independent of v. With increasing v, the peak first shifts to lower energy and then to higher energy. This is somewhat counter-intuitive, since usually the coupling smears the peaks. We will have a general discussion about the DOS at the end of Section 5.2.1.

5.1.2 *The I-V Curve*

Fig.5.4 shows the current as a function of the bias applied to the left lead without the direct lead-lead link - i.e. for the situation of $v = 0$. We have verified that these curves are identical with those obtained by directly evaluating the current formula Eq.(2.3).

Then, in Fig.5.5 we show the current where t_α is zero, which means there is only a direct lead-lead link and no quantum dot. As we expect, there is only

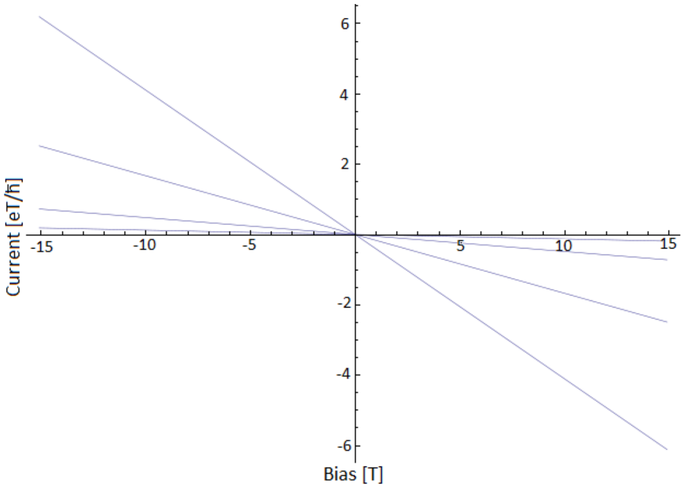

Figure 5.5: Current of the left lead as a function of the bias applied to the left lead. The temperature T sets the energy unit. The lead-lead coupling constant v is chosen to be $0.5, 1, 2, 4T$ for the curves with least to greatest slopes, respectively.

linear response.

Finally we plot the current with both non-zero v and t_α in Fig.5.6. For the sake of clarity we shifted the curves to separate them. Basically, if we take out the curves from Fig.5.4 and add them to the $v = 0.5$ curve in Fig.5.5, what we get will just be like Fig.5.6. This means the two tunneling channels are almost independent at the Hartree-Fock level.

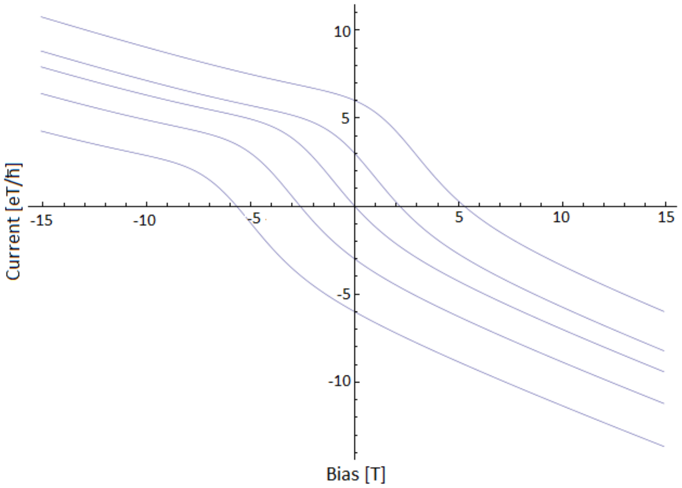

Figure 5.6: Current in the left lead as a function of bias applied to the left lead. The temperature T sets the energy unit. The lead-lead coupling constant $v = 0.5T$, the lead-dot coupling constant $t_\alpha = T$. These I-V curves, from bottom to top, are for $\epsilon_d = -4, -2, 0, 2, 4T$, respectively. For better clarity we have shifted each curve by $1.5\epsilon_d$.

5.2 Higher Order Results

To go beyond the Hartree-Fock approximation, we apply the following truncation rules:

$$\langle d_\sigma^\dagger d_\sigma O\rangle \approx N_\sigma \langle O\rangle \tag{5.6}$$

$$\langle c_{\alpha\sigma k}^\dagger c_{\alpha\sigma k'} O\rangle \approx f_\alpha(k)\delta_{kk'}\langle O\rangle \tag{5.7}$$

where O represents any sequence of operators. Here Rule (5.2) is applied whenever the total number of $d_\sigma^\dagger$ or d_σ exceeds 3; Rule (5.3) is applied whenever the total number of $c_{\alpha\sigma k}^\dagger$ or $c_{\alpha\sigma k}$ exceeds 1 (similar to that used for Hartree-Fock).

Then SymGF derives the following expression for $G^r(\omega)$:

$$\begin{aligned} G^r_\sigma(\omega) = 1\left(g_1(\omega) - A(\omega)(1-N_{\bar{\sigma}})\right) \Big/ \Bigg(& 1 + i\pi g_1(\omega)\frac{t_L^2(\omega)+t_R^2(\omega)}{1+\pi^2 v_{\omega,\omega}^2} + \\ & 2\frac{\pi^2 g_1(\omega)}{1+\pi^2 v_{\omega,\omega}^2} t_R(\omega) t_L \omega v_{\omega,\omega} + A(\omega) \times \\ & \left(\frac{i\pi g_2(\omega)}{1+\pi^2 v_{\omega,\omega}^2}\sum_\alpha t_\alpha(\omega)^2 (2 - f_\alpha(\omega) - f_\alpha(U+2\epsilon_d-\omega)) + \right. \\ & \left. \frac{\pi^2 g_2(\omega)}{1+\pi^2 v_{\omega,\omega}^2} t_R(\omega) t_L(\omega) v_{\omega,\omega} \sum_\alpha (f_\alpha(U+2\epsilon-\omega) - f_\alpha(\omega))\right)\Bigg) \end{aligned} \tag{5.8}$$

where $N_{\bar{\sigma}}$ is the occupation number of the opposite spin and we have defined

$$A(\omega) \equiv \frac{U g_1(\omega) g_2(\omega)}{1 + \frac{3g_2(\omega)}{1+\pi^2 v_{\omega,\omega}^2}\left(i\pi(t_R(\omega)^2 + t_L(\omega)^2) + 2\pi^2 t_R(\omega) t_L(\omega) v_{\omega,\omega}\right)} \tag{5.9}$$

and the isolated Green's functions

$$\begin{aligned} g_1(\omega) &= \frac{1}{\omega - U - \epsilon} \\ g_2(\omega) &= \frac{1}{\omega - \epsilon}\ . \end{aligned} \tag{5.10}$$

5.2.1 Density of States

In Fig.5.7, DOS of the central dot at high order correlation is shown. The unit of energy is set by $t_L = t_R$. Applying the wide band limit approximation, the energy symbol ω can be dropped. From this figure we find two sharp peaks of DOS separated slightly more than U when v is large. This is an effect of the on-site interaction and the peaks show a Coulomb blockade phenomenon, where two major peaks of DOS of the central dot is present at energy around the energy level of the central dot ϵ and around the energy level plus the on-site interaction

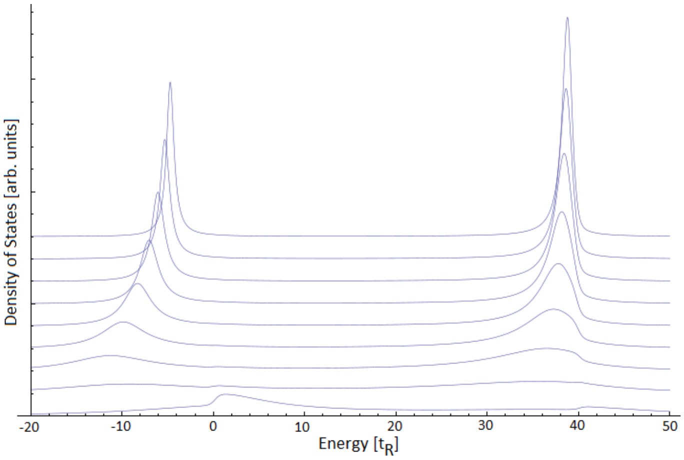

Figure 5.7: Density of states obtained with higher order Green's function Eq.(5.8). The horizontal axis is energy. The unit is t_R. The parameters we used are: $U = 4t_R$, $\epsilon_d = 0$, temperature $T = 0.3t_R$, chemical potentials of both leads $\mu_L = \mu_R = 0$; from bottom up, the lead-lead coupling v ranges from 0 to $1.6t_R$ in steps of $0.2t_R$. Each curve is shifted $0.1t_R$ upward, consecutively.

$\epsilon + U$, because at these energies it is easier for the electrons in the leads to hop in. Between the two energies ϵ and $\epsilon + U$ there is barely any hopping, so come the name "Coulomb blockade". From Fig.5.7 we see the larger the coupling v gets, the sharper the peaks become. When v is very small or zero, there are still two peaks - though not very pronounced, and they both have shifted to higher energy. Comparing Fig.5.7 with Fig.5.2 and Fig.5.3, each peak in Fig.5.7 has the features presented in Figs.5.2 and 5.3. Namely, with increasing v, the peaks gets higher and sharper, meanwhile the peak position shifts to lower energy first and then to higher energy as v increases. But the two peaks are slightly different from each other, because the self-consistently determined occupation number is not 0.5 (not shown). Again, this DOS obtained at higher order is qualitatively

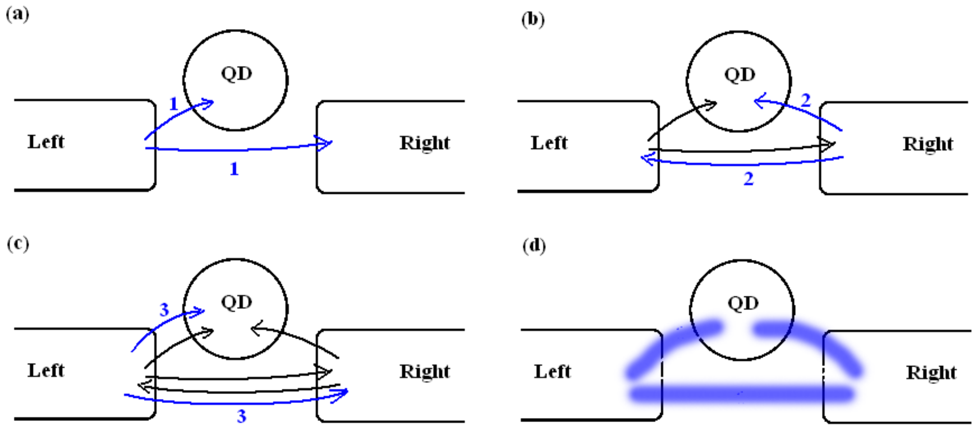

Figure 5.8: Transition process showing the direct inter-lead link enhances the transition from the leads to the central. (a)-(c) show how electrons could jump from one site to another; and (d) illustrates the total effect. With the direct link between the leads the transition between the central dot and the leads are made easier.

different from that obtained with Hartree-Fock approximation (Figs.5.2 and 5.3).

In both Hartree-Fock and this higher order calculation, we see that with larger lead-lead coupling constant v, the DOS of the central dot becomes larger, with the DOS peak higher and sharper. Mathematically this is quite straightforward - one just have to solve Eq.(5.4) for Hartree-Fock or solve more complicated equations derived by SymGF. Physically, an electron in, for example, left lead can tunnel to both the central dot and to the right lead. At the right lead, it can go on tunnel, either to the central dot or back to the left lead. In terms of the transition between the central dot and the leads, this direct link between leads provide a multiplier to the transition rate without this direct link. This process is shown in Fig.5.8. This is the picture why larger v leads to larger DOS

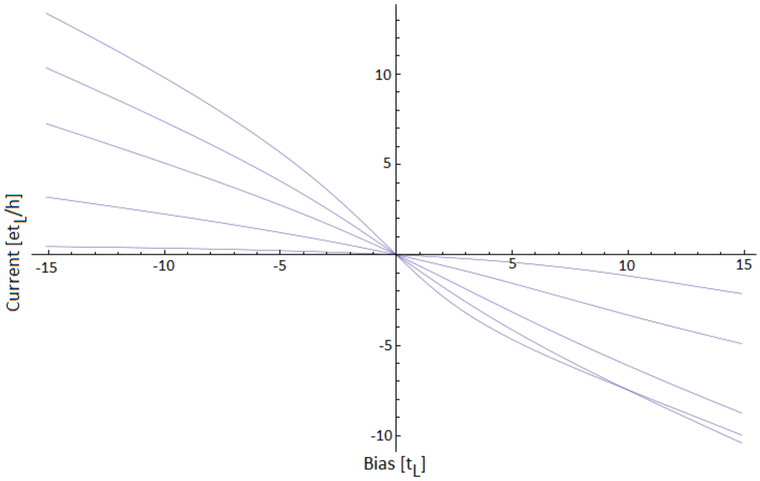

Figure 5.9: Current in the left lead as a function of the bias applied to the left lead. Wide-band limit approximation is used and symmetric lead-dot coupling is assumed ($t_L = t_R$). Energy unit is chosen as t_L. The parameters are: $U = 40t_L$, $\epsilon_d = 0$, temperature $T = 0.3t_L$. At bias $-15t_L$, from bottom to top, the lead-lead coupling v is chosen to be 0, $0.2t_L$, $0.4t_L$ and $0.6t_L$, respectively.

on the central quantum dot.

5.2.2 *The I-V Curve*

Fig.5.9 plots the current obtained with the higher order Green's function Eq.(5.8) versus the bias applied to the left lead. Unlike Fig.5.6, curves in Fig.5.9 are very different from the sum of their independent channels (i.e., when $t_\alpha = 0$ and when $v = 0$, not shown here). Inspecting the EOMs derived by SymGF, there are many Green's functions containing operators of one lead, such as $\langle d_\uparrow d_\downarrow c^\dagger_{L\downarrow} d^\dagger_\uparrow \rangle$, that are related to the Green's function of similar kind by with operators in the second lead such as $\langle d_\uparrow d_\downarrow c^\dagger_{R\downarrow} d^\dagger_\uparrow \rangle$. In the Hartree-Fock calculation, the EOM Eq.(5.4) have only two such occasions ($\langle c_{Lk} d^\dagger_\uparrow \rangle$ and $\langle c_{Rk} d^\dagger_\uparrow \rangle$), but in the higher order calculation such inter-lead connection of Green's functions is more common. These findings appear to suggest that the higher correlation reveals more quantum interference between the quantum paths going through the two leads. We hope direct quantitative comparisons to real experiments can be made in the future.

5.3 Summary

In this chapter, we applied SymGF to a device where the two electrodes are bridged by both a central quantum dot and a direct lead-lead link. Analysis were done at both the Hartree-Fock and a higher order correlation. Qualitative differences are observed in the DOS obtained at the two different correlation levels. We can identify a Coulomb blockade due to the on-site interaction. We also observe that the DOS peaks become sharper and higher when the lead-lead coupling becomes stronger. The two tunneling paths - one through the quantum dot and the other through the direct link, appear to interfere. But such an interference is not obvious if the calculation is only done at the Hartree-Fock level. The conductance (dI/dV) corresponding to the Hartree-Fock result Fig.5.6 (not shown) has a more obvious Fano lineshape than the higher order result Fig.5.9. This has been seen in the T-shaped double quantum dot system we investigated in Chapter 4, where Fano lineshape in higher order results can be buried in a wide range of parameters while Hartree-Fock result always has that feature except a few cases. This is reasonable as higher order formula brings in more electronic structures that may compete with Fano lineshape.

6

SymGF for *ab initio* Calculation

We have so far carried out model analysis of quantum transport in various device structures at various levels of correlations. By model analysis we mean the Hamiltonian of the device and the parameters in the Hamiltonian are not obtained by calculation, but postulated following the physical situation. Model calculations have the advantage of revealing the underlying physics of a given model without carrying out tedious numerical computation, even for higher correlation effects.

For practical purposes, one may be interested in materials specific issues of the transport physics, hence the Hamiltonian and its parameters need to be calculated by material specific first principles methods. So far, first principles numerical analysis of quantum transport has largely been done by combing the density functional theory (DFT), which aims to calculate many-body electronic ground state energy by means of the density of the electrons instead of the wave function, with NEGF[24, 25], where higher order correlations are completely ignored. A DFT calculation has taken into account the classical Coulomb potential and the exchange-correlation potential at the mean field level. However, when it comes to transport, a non-interacting formula for the Green's function is so far used[24, 25].

Clearly, we can use the *ab initio* tools to calculate parameters of a device model, apply these parameters in the high order formulas derived by SymGF, and investigate higher order correlation effects in specific device structures and materials. It is the purpose of this chapter to investigate the possibility of using SymGF in combination with *ab initio* calculations. In particular, we obtain parameters in the Anderson Model Hamiltonian by means of an *ab initio* calculation, and then substitute them into the formulas obtained by SymGF. The main purpose of this chapter is to demonstrate the procedures, hence we use a very simple atomic model in our actual calculations.

6.1 Parameters in the Hamiltonian

In the numerical analysis, we apply the NEGF-DFT method as implemented in the NanoDcal quantum transport package[27]. The NEGF-DFT method has been documented extensively in literature[79, 80] and will not be repeated here. Very briefly, in the NEGF-DFT method for quantum transport in open device structures (e.g. Fig.1.1), DFT is used to determine the device Hamiltonian and the electronic structure with the non-equilibrium density matrix provided by NEGF; and in order for NEGF to determine the nonequilibrium density matrix, the Hamiltonian determined by DFT is needed. This gives rise to a self-consistent field (SCF) calculations. With SCF NEGF-DFT calculation, a wide range of nanoelectronic devices has been investigated in the literature, and for this work, we shall apply it to obtain the needed device parameters.

Obviously, the ultimate theory to combine SymGF and NEGF-DFT would be letting SymGF derive the formulas that is needed by NEGF, and bring that NEGF with higher order correlation into the SCF loop of NEGF-DFT. This will be a direction of future work. For now, we use SymGF as a post process of *ab initio* calculations done by NEGF-DFT.

According to the Hamiltonian Eq.(2.15), we need several parameters from first principles calculation and these are obtained by using the NanoDcal electronic package. These parameters are: energy levels of each parts of the device (when they are isolated), the coupling constants between them, and an on-site interaction energy. These parameters are then used in the formula derived by SymGF. Before going into details, we emphasize that the on-site energy obtained by DFT is a mean field value, a more accurate value requires more accurate many-body methods such as quantum Monte Carlo or exact diagonalization. Exact diagonalization is prohibitively expensive from the computation point of view and is beyond the scope of this work.

6.1.1 Energy Levels

In the device model of NanoDcal, a two-lead system (see Fig.1.1) is partitioned into seven parts: the left lead, the central scattering region, the right lead, the coupling between left lead and central region and between the central region

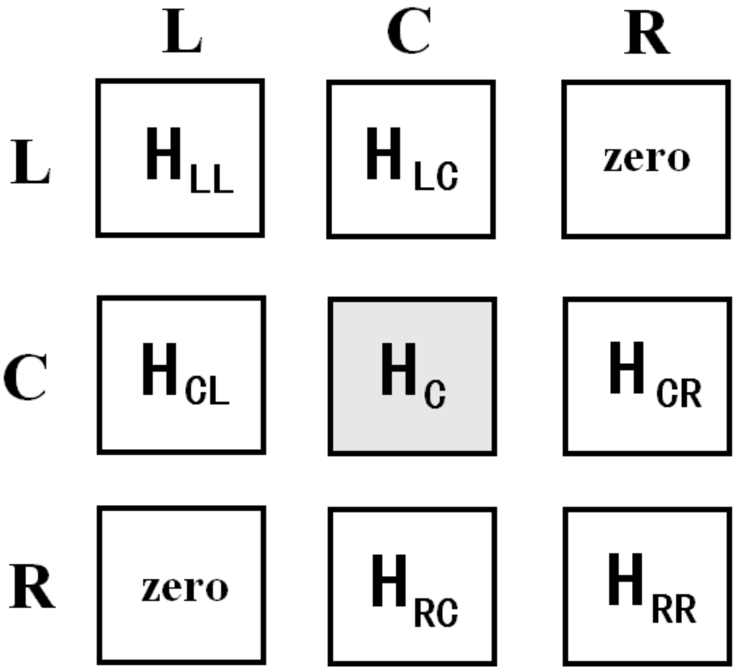

$$\begin{array}{c|ccc} & \mathbf{L} & \mathbf{C} & \mathbf{R} \\ \hline \mathbf{L} & H_{LL} & H_{LC} & \text{zero} \\ \mathbf{C} & H_{CL} & H_{C} & H_{CR} \\ \mathbf{R} & \text{zero} & H_{RC} & H_{RR} \end{array}$$

Figure 6.1: The general device structure of NanoDcal transport package. It is divided into blocks (sub-Hilbert spaces) for the left lead (H_{LL}), the right lead (H_{RR}), the central scattering region (H_C), the coupling between left lead and central region (H_{LC} and H_{CL}), and finally the coupling between right lead and the central region (H_{RC} and H_{CR}). Since NanoDcal does not assume there to be any direct coupling between the left and right leads, the sub-Hamiltonian for these coupling at the upper-right and lower-left corners are zero.

and left lead, the coupling between right lead and central region and between central region and right lead. The structure of the corresponding Hamiltonian is sketched in Fig.6.1. To obtain the energy levels for the central region, we simply diagonalize the DFT Hamiltonian corresponding to the central region H_C (i.e., central shaded part in Fig.6.1) which also finds eigenfunctions ψ_d.

If one wishes to use a single-level approximation in the SymGF analysis, one should focus on one scattering state which is calculated by NanoDcal. A scattering state is an eigen-state of the device Hamiltonian whose energy is well defined. Scattering states encode the interactions between every parts of the system. This way, from the output of NanoDcal, we obtain the energy levels ϵ_σ in the Hamiltonian Eq.(2.15) and its corresponding eigen-states which will be used in evaluating the coupling constants t_α.

6.1.2 Interaction

The on-site interaction, by its physical significance, is the energy that is required to add an extra electron to the system, namely $U = E(N+1) - E(N)$ where N is the number of electrons in the system. Almost every *ab initio* software tools provide a functionality to calculate the total energy with or without electronic neutrality, thus U can be obtained. Again, as discussed above, this way of determining U is at the mean-field level.

6.1.3 Coupling Constants

Getting the coupling constants, e.g. the parameters t_α in Eq.(2.15), is somewhat tricky. One needs to calculate the scattering states first. In NanoDcal, calculation of scattering states is provided; one only has to provide the energy at which the scattering states are calculated. Once the scattering states (hereafter denoted by ψ_{SC}) are obtained, one obtains the coupling constants by

$$t(\omega) =< \psi_d|H|\psi_{SC}(\omega) > \ , \tag{6.1}$$

where H is the total Hamiltonian calculated by the NEGF-DFT code, and we have transformed t's dependence on continuous quantum number k into energy

ω, as the scattering states ψ_{SC} is calculated at specified energies.

Generally, a number of coupling constants at different energies are required even at zero temperature. This is because the energy levels of the central region is hybridized with those in the device leads, thus the levels are widened. Therefore one has to repeat the above procedure for a small energy range. Finally, since the coupling constants depend continuously on energy, one can interpolate to obtain them at any particular energy.

6.2 Example: a Carbon-Nitrogen Wire Attached to Copper Leads

In this section, we present an example with a NC_3N wire connecting to symmetric copper leads. This exercise is not meant to investigate an experimentally realistic material, but to demonstrate the theoretical development of this Chapter. For simplicity, we use the single level approximation.

6.2.1 The System and the On-Site Interaction

The system is shown in Fig.6.2. All the atoms are aligned in a straight line, and the inter-atomic distances are as marked. The copper leads are semi-infinite.

To obtain the parameter U, we apply DFT as implemented in the Vienna ab initio package (VASP)[81, 82, 83, 84] on a neutral NC_3N wire to calculate the total energy $E(N)$. We then repeat the same calculation by adding one extra electron to calculate $E(N + 1)$. With these values, we obtain the on-site

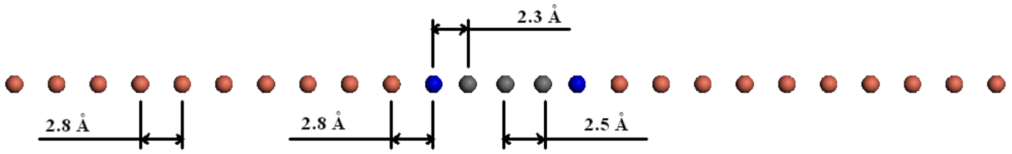

Figure 6.2: The NC_3N wire connected to copper chain leads. The copper chains are semi-infinitely long. The atoms in orange are copper, in blue ones are nickel, and in white are carbon.

interaction $U = E(N+1) - E(N)$ to be 3.4eV.

6.2.2 The NanoDcal Calculation

Using NanoDcal transport package[27], we have self-consistently calculated the device Hamiltonian of the two-lead device. The band structure of the leads are shown in Fig.6.3. We observe that for the copper chain, there is only one band that crosses the Fermi level. This means we can well use the single level approximation. Should there be another band that crosses the Fermi level, the scattering states will have an explicit band dependence, and we have to obtain the full spectrum by diagonalizing the central region's Hamiltonian.

Once we have completed the NEGF-DFT self-consistent calculation by NanoDcal, we obtain the central region's density of states at the presence of the leads, shown in Fig.6.4.

The NEGF-DFT calculation also gives the scattering state which is plotted in Fig.6.5. Since NanoDcal uses localized basis set[85, 86], the left lead, central region and right lead are shown quite intuitively. With the scattering state, we

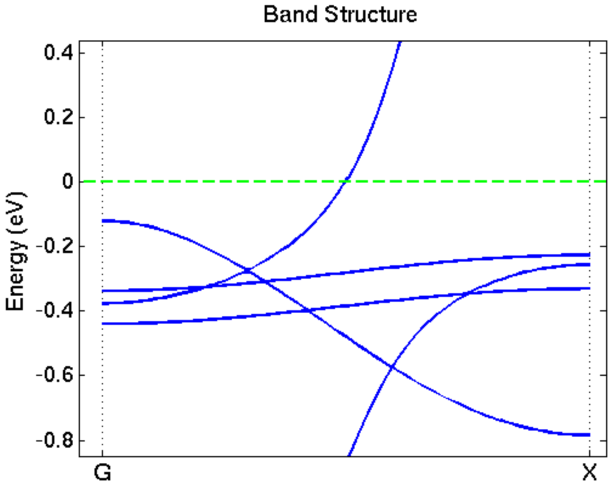

Figure 6.3: The band structure of the copper chain leads. There is only one band that crosses the Fermi energy. This simplifies the calculation of the coupling constant $t_{\alpha k}$

.

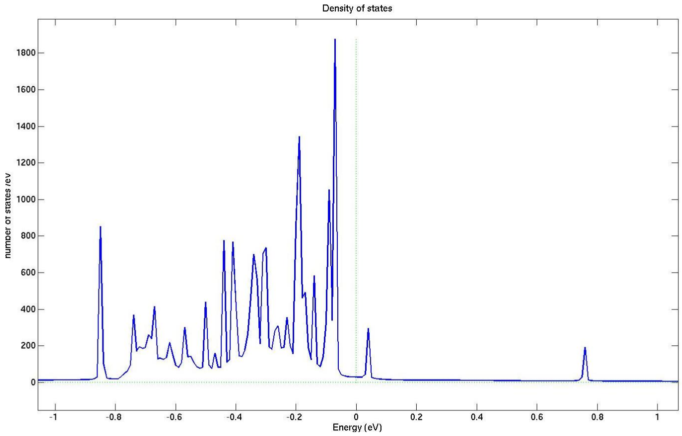

Figure 6.4: Density of states of the NC_3N wire at the presence of the copper leads. Electronic structures below the Fermi level is much richer than above it.

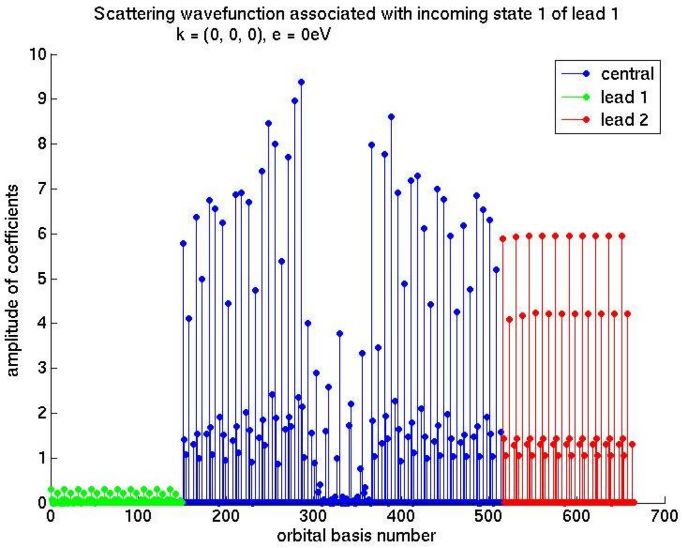

Figure 6.5: The scattering states of the whole system at the Fermi level. The left and right lead is easily recognized as they tend to be uniform. The whole scattering state is normalized with respect to the current.

can obtain the energy level that amounts to the single level approximation. In this problem, the energy level of Eq.(2.15) is found to be $\epsilon_\sigma = 0.6$Hartree, or 16.3eV.

Once the scattering states are obtained at various energies, we can proceed to the calculation of the coupling constants $t_{\alpha k \sigma}$. The coupling constants are usually complex numbers. However, since finally we will only need their square modulus, we can ignore their phase information altogether, keeping only their modulus. The coupling constants as a function of energy is plotted in Fig.6.6.

We plot the conductance of the copper-NC_3N-copper atomic wire in Fig.6.7 at various temperatures. This figure contains 34 data points for temperature ranging from $T = 0$K to $T = 330$K in steps of 10K. A general trend is that

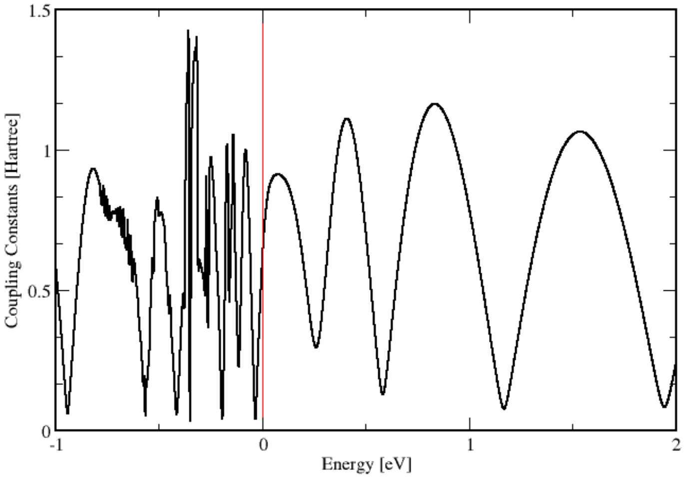

Figure 6.6: The coupling constants versus energy. This is obtained with Eq.(6.1). The coupling is very sensitive to energy below the Fermi level.

the conductance is close to G_0 ($G_0 \equiv 2e^2/h$) at $T = 0$K and it reduces as the temperature raises; but at a high enough temperature the conductance raises again. The product of the density of states (Fig.6.4) and the coupling between the leads and the scattering region (we can estimate it from Fig.6.6) has a sharp peak around the Fermi level, so that at low temperature the conductance is close to G_0 but when the Fermi-Dirac distribution of the leads is smeared by higher temperature, the conductance reduces. The rise of the conductance at even higher temperature can be understood as follows. Since we are plotting the conductance at 0-330K, the energy range that we should consider is -0.1eV till 0.1eV, as this is the range where the derivative of the Fermi-Dirac distribution function is significantly different from zero, namely,

$$f'(\omega) = -\frac{e^{\omega/k_BT}}{k_BT\left(1+e^{\omega/k_BT}\right)^2} \tag{6.2}$$

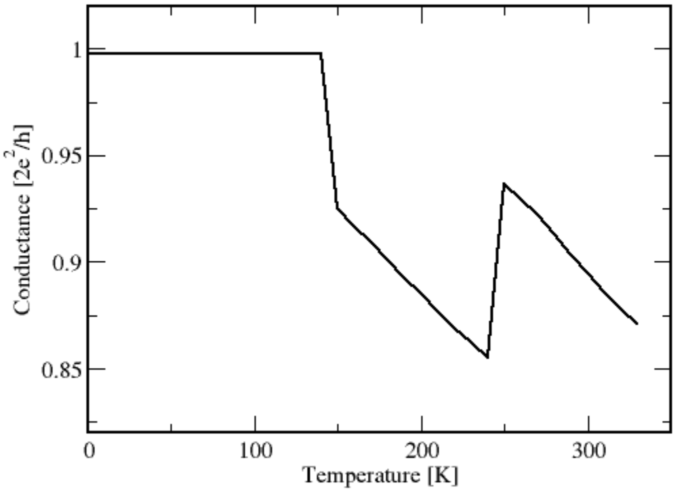

Figure 6.7: Conductance at various temperatures. The data points are taken in steps of 10K until 330K.

where $k_B = 8.617 \times 10^{-5}$eV/K is the Boltzmann constant, and T the temperature that ranges from 0 to 330K. In this energy range, we can see that the peak contributing to the rise of conductance at higher temperature is actually the DOS peak at energy $\omega = 0.05$eV (see Fig.6.4), while the peak at $\omega = -0.07$eV has no contribution since the coupling at that energy is very small (see Fig.6.6). We shall compare our SymGF results with these findings.

6.2.3 SymGF Results

With the parameters obtained in the last subsection, SymGF can carry out its calculations. The formulas generated by SymGF are the same as in that in Section 3.6.2, e.g. Eq.(3.21). The density of states are plotted in Fig.6.8. Comparing Fig.6.8 with Fig.6.4, we see that both DOS plot has the feature that

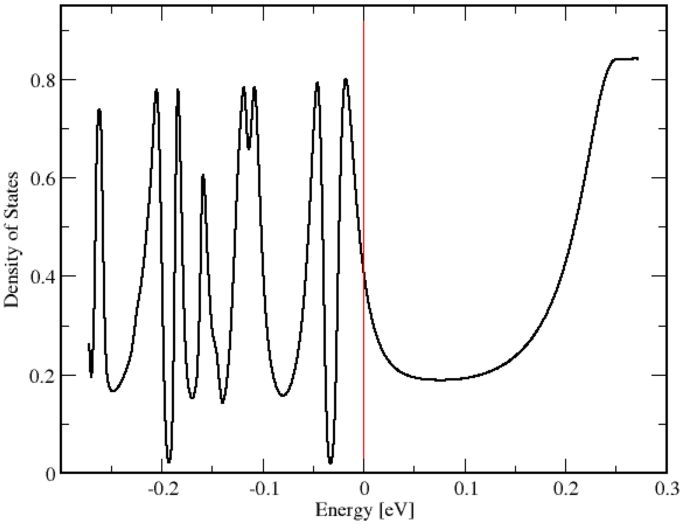

Figure 6.8: Density of states obtained by SymGF with parameters generated by first principles method NanoDcal for the 1-D stomic chain shown in Fig.6.2. It has similar features as that in Fig.6.4.

below Fermi energy the electronic structure is richer than it is above Fermi level. But since in the SymGF calculation we are using the single level approximation, all the features in Fig.6.8 come from the coupling between the leads and the central scattering region (Fig.6.6). If we used wide-band limit, then the DOS produced by SymGF will have at most two regular peaks like what is shown in Fig.3.2. Since the interaction U is determined to be 3.4eV (see Section 6.2.1), DOS in this energy range is mostly determined by the coupling constants t_α (Fig.6.6).

The temperature dependent conductance obtained by SymGF is shown in Fig.6.9. It has the same trend as in Fig.6.7, namely, high conductance at low temperature, then it drops at higher temperature, and then increases back at

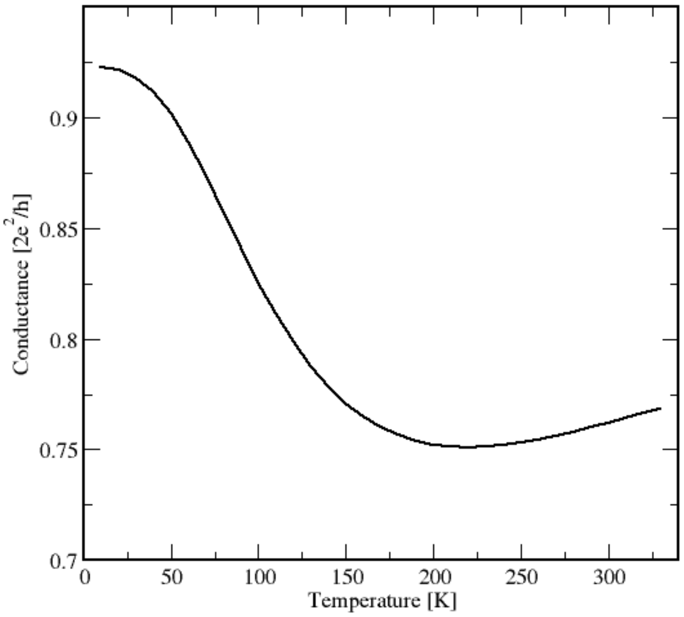

Figure 6.9: Conductance as a function of temperature obtained with formulas produced by SymnGF and the parameters calculated with NanoDcal. It roughly has the same trend as in Fig.6.7 that at low temperature the conductance is close to G_0. Then it decreases at higher temperature (100K) but increases again at even higher temperature (250K).

even higher temperature. This trend has been discussed in the last subsection. The conductance in Fig.6.9 is collectively smaller than that of Fig.6.7.

If $U = 0$, we get back the non-interacting problem. We plot in Fig.6.10 the effect of changing interaction U. With a larger U the conductance linearly becomes smaller. We observe that at smaller U, SymGF gives results closer to that of NanoDcal, which does not contain high order correlation terms induced by finite U.

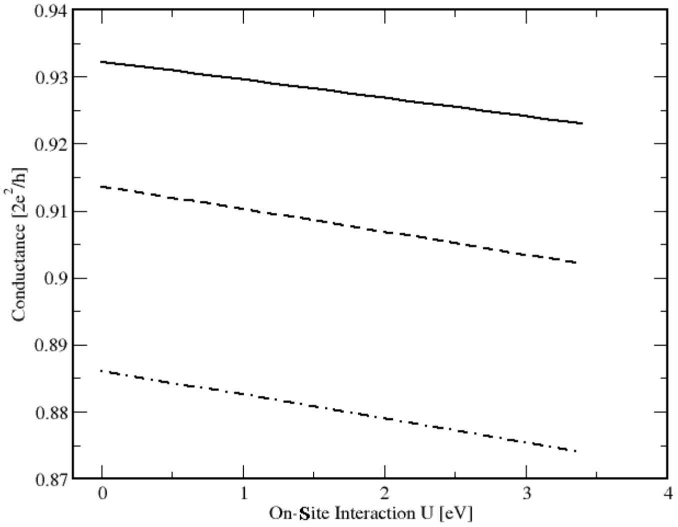

Figure 6.10: Conductance as a function of on-site interaction U. When U gets larger, the conductance reduces linearly. The value of U is taken from 0 to 3.4eV, which we determined to be the energy needed to add one more electron to the neutral NC_3N molecule.

6.3 Summary

In this chapter we have discussed how one can port SymGF to *ab initio* calculations, in particular, to combine it with the NEGF-DFT methods such as NanoDcal. The idea is to compute parameters in the Hamiltonian such as that of Eq.(2.15). To do so, we diagonalize the first principles NEGF-DFT Hamiltonian for the central region of the device to obtain the energy levels and eigen states; we calculate the scattering states of the leads (which have both energy and band dependence); we also determine the on-site interaction U by a mean-field total energy analysis; and finally we determine the coupling constants using the NEGF-DFT wave functions. Even though we focused on a system with just one scattering state, the general approach can be applied to systems having more states. We presented an example of a NC_3N wire connecting to copper chains. All the Hamiltonian parameters in Eq.(2.15) were obtained by the transport package NanoDcal and electronic package VASP. These parameters are plugged into the formulas in 3.6.2, namely to Eq.(3.21). A finite U reduces the conductance of the wire compared to the situation of non-interacting wires.

In summary, the steps for combining SymGF and NanoDcal (with single level approximation) for materials specific calculation are the following:

- Step 1 Complete an NanoDcal calculation and a SymGF run with the model of choice.
- Step 2 Calculate the scattering states for a range of energy around the Fermi level.
- Step 3 Diagonlize the Hamiltonian for the central scattering region provided by NanoDcal to obtain the energy levels and their corresponding eigen-wave functions.
- Step 4 For each scattering state at a given energy, calculate the coupling constant at that energy.
- Step 5 Substitute the parameters obtain in **Step 3** and **Step 4** into the formulas produced by SymGF in **Step 1** and obtain the final answer.

7

Conclusion

The Keldysh Non-Equilibrium Green's Function (NEGF) method is a very popular and powerful theoretical tool. Powerful as it is, however, when dealing with strong interactions, deriving formulas for NEGF can be prohibitively tedious, and this seriously limited its use.

In this thesis, we presented the development of a symbolic for quantum transport theory, called "SymGF". It helps deriving the Green's functions for transport systems. The major input to SymGF are (i) the model Hamiltonian in second quantized form, (ii) the anti-commutation rules of the operators involved in the Hamiltonian and (iii) the truncation rules that determine the order and accuracy of the final result. After a successful SymGF run, it gives the Green's function in terms of the self-energies that it automatically defines and the Green's functions for isolated systems which are known.

SymGF essentially does two things: (i) to derive the set of equations of motion (EOMs) and (ii) to solve them.

To derive the EOMs, SymGF follows the following procedure:

Step 1. For a given physical problem, make a model - meaning proposes a Hamiltonian in the second quantized form. Physical intuition is necessary.

Step 2. Understand and therefore write down the required Green's function (usually the Green's function of the central quantum dot). This is the starting point.

Step 3. Derive the EOMs for the Green's functions.

Step 4. For each of the new Green's functions produced by older Green's functions after the EOM iteration, check if it has reached the number of operators in our truncation rules. If yes, truncate it; if not, repeat **Step 3** for it.

Step 5. Repeat **Step 3** and **Step 4** until all Green's functions has an EOM and a closure is reached. Finally, the required Green's function can be solved from the final set of linear algebraic equations.

To solve the EOMs, SymGF makes use of a couple of algorithms. The most recommended algorithm is the Gaussian elimination for block matrices. Basically this is to treat each block matrix within the big matrix corresponding to the full set of EOMs like c-numbers, except the division becomes matrix inversion and regular multiplication becomes matrix multiplication. We elaborated this algorithm in Secion 3.3.4.

The test of SymGF included several of the manually solved problems, besides the three verifications presented in Section 3.6, it is also thoroughly tested against Ref.[33]. These tests greatly increased our faith in this tool that it could be assisting real research.

We have applied SymGF to a T-shaped double quantum dot system (see Chapter 4) and the system with direct lead-lead contact (see Chapter 5). We pushed formulas of both projects to a fairly high order. The results turned out to be reasonable. In Chapter 4, the high order results obtained by SymGF can even compare with experiments quantitively with an appropriate choice of parameters.

We can also use SymGF for *ab initio* calculations as well. One possible procedure is presented in Chapter 6 for NanoDcal. Basically, we are calculating the parameters in the model Hamiltonian with NanoDcal and putting those parameters into the formulas produced by SymGF.

In conclusion, SymGF has been proved to be reliable for the known problems and gave reasonable results for problems where results of the same order are not yet known. It is a very promising tool that has the potential of giving really fascinating results for complex problems.

8

Appendices

8.1 *Appendix A: Current Formula for Single Quantum Dot in Parallel with a Lead-Lead Link*

In this section, we provide a more detailed derivation of the current formula for the transport junction shown in Fig.2.1, where the gap of the two electrodes is bridged by a a single quantum dot in parallel with a direct conducting link.

The Hamiltonian of the system is Eq.(2.5), we reproduce it here:

$$\begin{aligned}\hat{H} = &\sum_{\epsilon} \sigma d_{\sigma}^{\dagger} d_{\sigma} + U d_{\uparrow}^{\dagger} d_{\uparrow} d_{\downarrow}^{\dagger} d_{\downarrow} + \sum_{\alpha\sigma k} \epsilon_{\alpha\sigma k} c_{\alpha\sigma k}^{\dagger} c_{\alpha\sigma k} + \\ &\left(\sum_{\alpha\sigma k} t_{\alpha k} c_{\alpha\sigma k}^{\dagger} d_{\sigma} + h.c \right) + \left(\sum_{\sigma k_1 k_2} v_{k_1 k_2} c_{L\sigma k_1}^{\dagger} c_{R\sigma k_2} + h.c. \right) \end{aligned} \tag{8.1}$$

We define the number operator of electrons with spin index σ in the left lead as $\hat{N}_{L\sigma} \equiv \sum_k c_{L\sigma k}^{\dagger} c_{L\sigma k}$, these electrons contribute the current in left lead as,

$$\hat{I}_{\sigma} = e \frac{d\hat{N}_{L\sigma}}{dt} \ .$$

By using the Heisenberg equation of motion, we have

$$\begin{aligned}\hat{I}_\sigma &= -ie[\hat{N}_{L\sigma}, H] \\ &= \left(-ie\sum_{k_1k_2} c^\dagger_{L\sigma k_1} c_{R\sigma k_2} v_{k_1k_2} + h.c.\right) + \\ &\quad \left(-ie\sum_{k} c^\dagger_{L\sigma k} d_\sigma t_{Lk} + h.c.\right)\end{aligned}$$

where the dependence on time t is assumed. Using this current operator we obtain the electric current to be:

$$\begin{aligned}I = -e&\sum_{k_1k_2} v_{k_1k_2} G^<_{\sigma k_1k_2}(t,t) + h.c \\ -e&\sum_{k} t_{Lk} G^<_{L\sigma k}(t,t) + h.c\end{aligned} \tag{8.2}$$

where we have defined

$$\begin{aligned}G^<_{k_1k_2}(t_2,t_1) &\equiv i\langle c^\dagger_{L\sigma k_1}(t_1) c_{R\sigma k_2}(t_2)\rangle \\ G^<_{L\sigma k}(t_2,t_1) &\equiv i\langle c^\dagger_{L\sigma k}(t_1) d_\sigma(t_2)\rangle \ .\end{aligned}$$

We then solve the time ordered Green's function (assuming steady state, so that it is a function of the difference in time $t_1 - t_2$),

$$G^t_{\sigma k_1k_2}(t_1-t_2) \equiv -i\langle T[c_{R\sigma k_1}(t_1) c^\dagger_{L\sigma k_2}(t_2)]\rangle \ .$$

Using EOM metho, we obtain:

$$\begin{aligned}\left(-i\frac{\partial}{\partial t_2} - \epsilon_L(k_2)\right) G^t_{\sigma k_1k_2}(t_1-t_2) = \sum_{k'} G^t_{R\sigma k_1k'}(t_1-t_2) v^*_{k_2k'} + \\ G^t_{R\sigma k_1}(t_1-t_2) t^*_L(k_2)\end{aligned} \tag{8.3}$$

where we have defined

$$G^t_{R\sigma k_1 k_2}(t_1 - t_2) = -i\langle T[c_{R\sigma k_1}(t_1) c^\dagger_{R\sigma k_2}(t_2)]\rangle$$

$$G^t_{R\sigma k_1}(t_1 - t_2) = -i\langle T[c_{R\sigma k_1}(t_1) d^\dagger_{\sigma}(t_2)]\rangle$$

Letting $g_{\alpha k}(t_1 - t_2)$ satisfy

$$\left(-i\frac{\partial}{\partial t_2} - \epsilon_L(k_2)\right) g_{\alpha k}(t_1 - t_2) = \delta(t_1 - t_2) \ ,$$

we can then solve Eq.(8.3) with convolution:

$$\begin{aligned} G^t_{\sigma k_1 k_2}(t_1 - t_2) = \sum_{k'} \int G^t_{R\sigma k_1 k'}(t_1 - t') v^*_{k_2 k'} g_{\alpha k_2}(t' - t_2) + \\ \int G^t_{R\sigma k_1}(t_1 - t') t^*_L(k_2) g_{\alpha k_2}(t' - t_2) \end{aligned} \tag{8.4}$$

And similarly,

$$\begin{aligned} G^t_{\alpha\sigma k_1}(t_1 - t_2) = \sum_{k'} \int G^t_{\bar{\alpha}\sigma k_1 k'}(t_1 - t') v^*_{k' k_1} g_{\alpha k_1}(t' - t_2) + \\ \int G^t_{\sigma}(t_1 - t') t_{\alpha k_1} g_{\alpha k_1}(t' - t_2) \end{aligned} \tag{8.5}$$

where $\bar{\alpha}$ means the other lead than the lead labeled α. Next, we apply the analytical continuation theorem to Eq.(8.4,8.5) and Fourier transform the resulting formula to obtain

$$\begin{aligned} G^<_{\sigma k_1 k_2} = \sum_{k'} G^r_{R\sigma k_1 k'} g^<_{L\sigma k_2} v^*_{k_2 k'} + \sum_{k'} G^<_{R\sigma k_1 k'} g^a_{L\sigma k_2} v^*_{k_2 k'} \\ + G^r_{R\sigma k_1} g^<_{L\sigma k_2} t^*_{L k_2} + G^<_{R\sigma k_1} g^a_{L\sigma k_2} t^*_{L k_2} \end{aligned} \tag{8.6}$$

and

$$\begin{aligned} G^<_{\alpha\sigma k} = \sum_{k'} (G^r_{\bar{\alpha}\sigma k'} g^<_{\alpha\sigma k} + G^<_{\bar{\alpha}\sigma k'} g^a_{\alpha\sigma k})\, v^*_{k' k_1} + \\ (G^r_{\sigma} g^<_{\alpha\sigma k} + G^<_{\sigma} g^a_{\alpha\sigma k})\, t_{Rk} \end{aligned} \tag{8.7}$$

where the dependence of Green's function on energy ω is assumed.

In this way, we can rewrite the current Eq.(8.2) in energy space as

$$\begin{aligned} I = -e \int \frac{d\omega}{2\pi} \sum_{k_1 k_2} v_{k_1 k_2} G^{<}_{\sigma k_1 k_2} + h.c \\ -e \int \frac{d\omega}{2\pi} \sum_{k} t_{Lk} G^{<}_{L\sigma k} + h.c \ . \end{aligned} \tag{8.8}$$

Our eventual goal is to express the current formula in terms of the Green's function of the central quantum dot $G^{r,<}_{\sigma}$. To this end, we substitute $G^{<}_{L\sigma k}$ into $G^{<}_{R\sigma k}$ and $G^{r}_{L\sigma k}$ into $G^{r}_{R\sigma k}$ to obtain

$$\begin{aligned} G^{<}_{R\sigma k} = {} & G^{r}_{\sigma} \Sigma^{r}_{Lv\sigma k} g^{<}_{R\sigma k} + G^{r}_{\sigma} \Sigma^{<}_{Lv\sigma k} g^{a}_{R\sigma k} + G^{<}_{\sigma} \Sigma^{a}_{Lv\sigma k} g^{a}_{R\sigma k} + \\ & \sum_{k'} G^{r}_{R\sigma k} \Sigma^{r}_{kk'} g^{<}_{R\sigma k} + \sum_{k'} G^{r}_{R\sigma k} \Sigma^{<}_{kk'} g^{a}_{R\sigma k} + \sum_{k'} G^{<}_{R\sigma k} \Sigma^{a}_{kk'} g^{a}_{R\sigma k} + \\ & G^{r}_{\sigma} g^{<}_{R\sigma k} t_{Rk} + G^{<}_{\sigma} g^{a}_{R\sigma k} t_{Rk} \end{aligned} \tag{8.9}$$

$$G^{r}_{R\sigma k} = G^{r}_{\sigma} \Sigma^{r}_{Lv\sigma k} g^{r}_{R\sigma k} + G^{r}_{R\sigma k} \Sigma^{r}_{kk'} g^{r}_{R\sigma k} + G^{r}_{\sigma} g^{r}_{R\sigma k} t_{Rk} \tag{8.10}$$

where we have defined

$$\begin{aligned} \Sigma^{t}_{Lv\sigma k} &\equiv \sum_{k'} t_{Lk'} g^{t}_{L\sigma k'} v^{*}_{k'k} \\ \Sigma^{t}_{k_1 k_2} &\equiv \sum_{k'} v_{k' k_2} g^{t}_{L\sigma k'} v^{*}_{k' k_1} \ . \end{aligned}$$

Considering $G^{r}_{R\sigma k}$, Σ^{r}_{Lvk}, $g^{r}_{R\sigma k}$ and t_{Rk} to be vectors whose elements are labeled by k; $\Sigma_{kk'} g^{r}_{R\sigma k}$ to be matrices whose elements are labeled by k and k', we reach the following matrix equation for $G^{r}_{R\sigma}$:

$$G^{r}_{R\sigma} \left(I - \Sigma^{r} g^{r}_{R\sigma} \right) = G^{r}_{\sigma} g^{r}_{R\sigma} \left(\Sigma^{r}_{Lv} + t_{R} \right)$$

where I is the unit matrix. Solving the above matrix equation, we obtain the following formal solution

$$G^r_{R\sigma} = G^r_\sigma g^r_{R\sigma} \left(\Sigma^r_{Lv} + t_R\right) \left(I - \Sigma^r g^r_{R\sigma}\right)^{-1} \tag{8.11}$$

where the superscript -1 means matrix inverse. Later we will explicitly invert the matrix by the binomial theorem[49], now we move on to find formal solutions for other Green's functions.

Similarly, we substitute Eq.(8.11) back into Eq.(8.9) and after some manipulation, we obtain the formal solution for the vector $G^<_{R\sigma}$:

$$\begin{aligned} G^<_{R\sigma} = \Big(& G^r_\sigma \left(\Sigma^<_{Lv} g^r_{L\sigma} + \Sigma^<_{Lv} g^a_{R\sigma} + t_R g^<_{R\sigma}\right) + G^<_\sigma \left(\Sigma^a_{Lv} g^a_{R\sigma} + t_R g^a_{R\sigma}\right) + \\ & G^r_\sigma g^r_{R\sigma} \left(\Sigma^r_{Lv} + t_R\right) \left(I - \Sigma^r g^r_{R\sigma}\right)^{-1} \left(\Sigma^r g^<_{R\sigma} + \Sigma^< g^a_{R\sigma}\right) \Big) \\ & \left(I - \Sigma^a g^a_{R\sigma}\right)^{-1} \end{aligned} \tag{8.12}$$

Now, we can write Eq.(8.8) in the following form

$$\begin{aligned} I = & -e \int \frac{d\omega}{2\pi} \sum_{k_1 k_2} v_{k_1 k_2} G^<_{\sigma k_1 k_2} + h.c \\ & -e \int \frac{d\omega}{2\pi} \sum_k t_{Lk} G^<_{L\sigma k} + h.c \\ = & -e \Bigg(\int \frac{d\omega}{2\pi} \Big(\sum_{k_1 k_2 k'} \left(G^r_{R\sigma k_1 k'} \Sigma^<_{k_1 k'} + G^<_{R\sigma k_1 k'} \Sigma^a_{k_1 k'}\right) + \\ & \sum_{k_1 k_2} \left(G^r_{R\sigma k_1} \Sigma^<_{Lv\sigma k_1} + G^<_{R\sigma k_1} \Sigma^a_{Lv\sigma k_1}\right) \Big) \Bigg) + h.c \\ & -e \int \frac{d\omega}{2\pi} \sum_k t_{Lk} G^<_{L\sigma k} + h.c \end{aligned} \tag{8.13}$$

In Eq.(8.13) above, we have "solved" $G^{r,<}_{\alpha\sigma k}$ in Eq.(8.11) and Eq.(8.12). Since the two leads are symmetric, replacing "R" with "L" in Eq.(8.12) gives the formal solution to $G^{<}_{L\sigma k}$.

We can solve for $G^{r,<}_{R\sigma k_1 k_2}$ with the same method:

$$G^{r}_{R\sigma k_1 k_2} = g^{r}_{R\sigma k_1}\delta_{k_1 k_2} + G^{r}_{\sigma k_1 k'} v_{k' k_2} g^{r}_{R\sigma k_2} + G^{r}_{R\sigma k_1} t^{*}_{R k_2} g^{r}_{R\sigma k_2} \tag{8.14}$$

$$\begin{aligned} G^{<}_{R\sigma k_1 k_2} &= g^{<}_{R\sigma k_1}\delta_{k_1 k_2} + G^{r}_{\sigma k_1 k'} v_{k' k_2} g^{<}_{R\sigma k_2} G^{<}_{\sigma k_1 k'} v_{k' k_2} g^{a}_{R\sigma k_2} \\ &\quad + G^{r}_{R\sigma k_1} t^{*}_{R k_2} g^{<}_{R\sigma k_2} + G^{<}_{R\sigma k_1} t^{*}_{R k_2} g^{a}_{R\sigma k_2} \ . \end{aligned} \tag{8.15}$$

We already have the energy-dependent EOM for $G^{<}_{\sigma k_1 k_2}$ in Eq.(8.6), now we write down the EOM for $G^{r}_{\sigma k_1 k_2}$ as follows

$$G^{r}_{\sigma k_1 k_2} = \sum_{k'} G^{r}_{R\sigma k_1 k'} v^{*}_{k_2 k'} g^{r}_{L\sigma k_2} + G^{r}_{R\sigma k_1} t^{*}_{L k_2} g^{r}_{L\sigma k_2}$$

Substituting them back to Eq.(8.14) and Eq.(8.15) we reach the following expressions after some mathematical manipulation:

$$\begin{aligned} G^{r}_{R\sigma k_1 k_2} &= g^{r}_{R\sigma k_1}\delta_{k_1 k_2} + G^{r}_{R\sigma k_1 k'} \Sigma^{r}_{k' k_2} g^{r}_{R\sigma k_2} + \\ &\quad G^{r}_{R\sigma k_1} \Sigma^{r}_{Lv\sigma k_2} g^{r}_{R\sigma k_2} + G^{r}_{R\sigma k_1} t^{*}_{R k_2} g^{r}_{R\sigma k_2} \end{aligned} \tag{8.16}$$

$$\begin{aligned} G^{<}_{R\sigma k_1 k_2} &= g^{<}_{R\sigma k_1}\delta_{k_1 k_2} + \sum_{k'} G^{r}_{\sigma k_1 k'} v_{k' k_2} g^{<}_{R\sigma k_2} + G^{r}_{R\sigma k_1} t^{*}_{R k_2} g^{<}_{R\sigma k_2} \\ &\quad G^{<}_{R\sigma k_1} t^{*}_{R k_2} g^{a}_{R\sigma k_2} + \sum_{k'} G^{r}_{R\sigma k_1 k'} \Sigma^{<}_{k' k_2} g^{a}_{R\sigma k_2} + \sum_{k'} G^{<}_{R\sigma k_1 k'} \Sigma^{a}_{k' k_2} g^{a}_{R\sigma k_2} \\ &\quad G^{r}_{R\sigma k_1} \Sigma^{<}_{Lv\sigma k_2} g^{a}_{R\sigma k_2} + G^{<}_{R\sigma k_1} \Sigma^{a}_{Lv\sigma k_2} g^{a}_{R\sigma k_2} \ . \end{aligned}$$

Hence we obtain the formal solutions for $G^{r,<}_{R\sigma k_1 k_2}$ as (we denote the corresponding matrix of these Green's functions with $\bar{G}^{r,<}_{R\sigma}$ to distinguish from $G^{r,<}_{R\sigma}$ which correspond to $G^{r,<}_{R\sigma k}$ and $\bar{G}^r_\sigma$ for $G^r_{\sigma k_1 k_2}$):

$$\bar{G}^r_{R\sigma} = \left(g^r_{R\sigma} + G^r_{R\sigma}\Sigma^r_{Lv\sigma} g^r_{R\sigma} + G^r_{R\sigma} t^*_R g^r_{R\sigma}\right)\left(I - \Sigma^r g^r_{R\sigma}\right)^{-1} \tag{8.17}$$

$$\begin{aligned}\bar{G}^<_{R\sigma} = \Big(& g^<_{R\sigma} + \bar{G}^r_\sigma v g^<_{R\sigma} + G^r_{R\sigma} t^*_R g^<_{R\sigma} + G^<_{R\sigma} t^*_R g^a_{R\sigma} + \\ & G^r_{R\sigma}\Sigma^< g^a_{R\sigma} + G^r_{R\sigma}\Sigma^<_{Lv\sigma} g^a_{R\sigma} + G^<_{R\sigma}\Sigma^a_{Lv\sigma} g^a_{R\sigma}\Big) \\ & \left(I - \Sigma^a g^a_{R\sigma}\right)^{-1} \ .\end{aligned} \tag{8.18}$$

Now we evaluate the self-energies and carry out the matrix inversion. Basically, we shall repeatedly apply the Plemelj formula[50] and the binomial inversion theorem[49] (see discussions in Section 3.3.4).

First, we deal with Eq.(8.11). By applying the Plemelj formula we have

$$\Sigma^r_{k_1 k_2} g^r_{R\sigma k_1} = -i\pi v_{\omega k_2} v^*_{\omega k_1} g^r_{R\sigma k_1}$$

Therefore in Eq.(8.11) we need the inverse of the matrix

$$M_{k_1 k_2} = \delta_{k_1 k_2} + i\pi v_{\omega k_1} v^*_{\omega k_2} g^r_{R\sigma k_2} \ .$$

Applying the binomial inverse theorem (Eq.3.10) and then the Plemelj formula again, we have

$$M^{-1}_{k_1 k_2} = \delta_{k_1 k_2} - \frac{i\pi v_{\omega k_1} v^*_{\omega k_2} g^r_{R\sigma k_2}}{1 + \pi^2 v^2_{\omega,\omega}}$$

and therefore

$$\begin{aligned} G^r_{R\sigma k} = G^r_\sigma \times \Big(& \Sigma^r_{Lv\sigma k} g^r_{R\sigma k} + t_{Rk} g^r_{R\sigma k} + \\ & \frac{i\pi \sum_{k'} \Sigma^r_{Lv\sigma k'} g^r_{R\sigma k'} v_{\omega,k'} v^*_{\omega,k} g^r_{R\sigma k}}{-1 - \pi^2 v^2_{\omega,\omega}} + \\ & \frac{i\pi \sum_{k'} t_{Rk'} g^r_{R\sigma k'} v_{\omega,k'} v^*_{\omega,k} g^r_{R\sigma k}}{-1 - \pi^2 v^2_{\omega,\omega}}\Big) \end{aligned}$$

Applying the Plemelj formula again, we reach the final expression for $G^r_{R\sigma k}$ in terms of only the Green's function of the central quantum dot and other parameters that are known through the Hamiltonian,

$$\begin{aligned} G^r_{R\sigma k} = G^r_\sigma \times \Big(& \Sigma^r_{Lv\sigma k} g^r_{R\sigma k} + t_{Rk} g^r_{R\sigma k} + \\ & \frac{i\pi^3 t_{L\omega} v^2_{\omega,\omega} v^*_{\omega,k} g^r_{R\sigma k}}{1+\pi^2 v^2_{\omega,\omega}} + \frac{\pi^2 t_{R,\omega} v_{\omega,\omega} v^*_{\omega,k} g^r_{R\sigma k}}{-1-\pi^2 v^2_{\omega,\omega}} \Big) . \end{aligned} \tag{8.19}$$

To solve $G^<_{R\sigma k}$, we first need the inverse of the matrix

$$M_{k_1 k_2} = \delta_{k_1 k_2} - i\pi v_{\omega k_1} v^*_{\omega k_2} g^a_{R\sigma k_2}$$

Applying the binomial inverse theorem (Eq.3.10) and then the Plemelj formula, we have

$$M^{-1}_{k_1 k_2} = \delta_{k_1 k_2} + \frac{i\pi v_{\omega k_1} v^*_{\omega k_2} g^r_{R\sigma k_2}}{1+\pi^2 v^2_{\omega,\omega}}$$

Next, we substitute the solution Eq.(8.19) into Eq.(8.9), the relevant terms are, first,

$$\begin{aligned} \sum_{k'} G^r_{R\sigma k'} \Sigma^r_{kk'} g^<_{R\sigma k} = \sum_{k'} G^r_\sigma \times \Big(& \Sigma^r_{Lv\sigma k'} g^r_{R\sigma k'} + t_{Rk'} g^r_{R\sigma k'} + \\ & \frac{i\pi^3 t_{L\omega} v^2_{\omega,\omega} v^*_{\omega,k'} g^r_{R\sigma k'}}{1+\pi^2 v^2_{\omega,\omega}} - \frac{\pi^2 t_{R\omega} v_{\omega,\omega} v^*_{\omega,k'} g^r_{R\sigma k'}}{1+\pi^2 v^2_{\omega,\omega}} \Big) \\ & (-i\pi) v_{\omega,k'} v^*_{\omega,k} g^<_{R\sigma k} \end{aligned}$$

Applying the Plemelj formula[50] again, we have

$$\begin{aligned} \sum_{k'} G^r_{R\sigma k'} \Sigma^r_{kk'} g^<_{R\sigma k} = -i\pi G^r_\sigma v^*_{\omega,k} g^<_{R\sigma k} \Big(& -\pi^2 t_{L\omega} v^2_{\omega,\omega} - i\pi t_{R\omega} v_{\omega,\omega} + \\ & \frac{\pi^4 t_{L\omega} v^4_{\omega,\omega}}{1+\pi^2 v^2_{\omega,\omega}} + \frac{i\pi^3 t_{R\omega} v_{\omega,\omega} v^2_{\omega,\omega}}{1+\pi^2 v^2_{\omega,\omega}} \Big) \end{aligned}$$

The second term (where we assumed $g^{<}_{L\sigma k} = 2\pi i f_L(k)\delta_{\omega,\omega_k}$) is:

$$\begin{aligned}\sum_{k'} G^{r}_{R\sigma k'}\Sigma^{r}_{kk'}g^{<}_{R\sigma k} = \sum_{k'} & 2\pi i f_L(\omega)G^{r}_{\sigma}(\omega)v^{*}_{\omega,k}g^{a}_{R\sigma k} \times \\ & \Big(-\pi^2 t_{L\omega}v^2_{\omega,\omega} - i\pi t_{R\omega}v_{\omega,\omega} + \frac{\pi^4 t_{L\omega}v^4_{\omega,\omega}}{1+\pi^2 v^2_{\omega,\omega}} + \\ & \frac{i\pi^3 t_{R\omega}v_{\omega,\omega}v^2_{\omega,\omega}}{1+\pi^2 v^2_{\omega,\omega}}\Big)\end{aligned}$$

Hence, we can reach the expression for $G^{<}_{R\sigma k}$:

$$\begin{aligned}G^{<}_{R\sigma k} = \sum_{k'} \Bigg(& G^{r}_{\sigma}\Sigma^{r}_{Lv\sigma k'}g^{<}_{R\sigma k'} + G^{r}_{\sigma}\Sigma^{<}_{Lv\sigma k'}g^{a}_{R\sigma k'} + G^{<}_{\sigma}\Sigma^{a}_{Lv\sigma k'}g^{a}_{R\sigma k'} + \\ & G^{r}_{\sigma}t_{Rk'}g^{<}_{R\sigma k'} + G^{<}_{\sigma}t_{Rk'}g^{a}_{R\sigma k'} + (-i\pi G^{r}_{\sigma}v^{*}_{\omega,k'}g^{<}_{R\sigma k'} + 2\pi i f_L(\omega)G^{r}_{\sigma}v^{*}_{\omega,k'}g^{a}_{R\sigma k'}) \times \\ & \Big(-\pi^2 t_{L\omega}v^2_{\omega,\omega} - i\pi t_{R\omega}v_{\omega,\omega} + \frac{\pi^4 t_{L\omega}v^4_{\omega,\omega}}{1+\pi^2 v^2_{\omega,\omega}} + \frac{i\pi^3 t_{R\omega}v_{\omega,\omega}v^2_{\omega,\omega}}{1+\pi^2 v^2_{\omega,\omega}}\Big)\Bigg) \times \\ & \left(\delta_{k'k} + \frac{i\pi v_{\omega,k'}v^{*}_{\omega,k}g^{a}_{R\sigma k}}{1+\pi^2 v^2_{\omega,\omega}}\right)\end{aligned} \tag{8.20}$$

Expanding Eq.(8.20) and applying the Plemelj formula, we have

$$\begin{aligned}G^{<}_{R\sigma k} = {} & G^{r}_{\sigma}\Sigma^{r}_{Lv\sigma k}g^{<}_{R\sigma k} + G^{r}_{\sigma}\Sigma^{<}_{Lv\sigma k}g^{a}_{R\sigma k} + G^{<}_{\sigma}\Sigma^{a}_{Lv\sigma k}g^{a}_{R\sigma k} + \\ & G^{r}_{\sigma}t_{Rk}g^{<}_{R\sigma k} + G^{<}_{\sigma}t_{Rk}g^{a}_{R\sigma k} + (-i\pi G^{r}_{\sigma}v^{*}_{\omega,k}g^{<}_{R\sigma k} + 2\pi i f_L(\omega)G^{r}_{\sigma}v^{*}_{\omega,k}g^{a}_{R\sigma k})B \\ & +2\pi^2 t_{L\omega}G^{r}_{\sigma}Y_k\left(f_R(\omega) - f_L(\omega)\right)v^2_{\omega,\omega} - \pi^2 t_{L\omega}G^{<}_{\sigma}Y_k v^2_{\omega,\omega} + \\ & 2\pi i G^{r}_{\sigma}Y_k f_R(\omega)t_{R\omega}v_{\omega,\omega} + i\pi G^{<}_{\sigma}Y_k t_{R\omega}v_{\omega,\omega} + \\ & 2\pi^2 G^{r}_{\sigma}Y_k(f_R(\omega) - f_L(\omega))v^2_{\omega,\omega}B\end{aligned}$$

where we have defined

$$B \equiv -\pi^2 t_{L\omega}v^2_{\omega,\omega} - i\pi t_{R\omega}v_{\omega,\omega} + \frac{\pi^4 t_{L\omega}v^4_{\omega,\omega}}{1+\pi^2 v^2_{\omega,\omega}} + \frac{i\pi^3 t_{R\omega}v_{\omega,\omega}v^2_{\omega,\omega}}{1+\pi^2 v^2_{\omega,\omega}} \tag{8.21}$$

and

$$Y_k \equiv \frac{i\pi v^*_{\omega,k} g^a_{R\sigma k}}{1 + pi^2 v^2_{\omega,\omega}}$$

In this way, Eq.(8.13) has only another two Green's functions need to be derived, namely $G^{r,<}_{R\sigma k_1 k_2}$. The matrix inversion contained in the formal solution Eq.(8.17) can be solved, it is

$$(I - \Sigma^r g^r_{R\sigma})^{-1}_{k_1 k_2} = \delta_{k_1 k_2} + \frac{-i\pi v^*_{\omega,k_1} v_{\omega,k_2} g^r_{R\sigma k_2}}{1 + \pi^2 v^2_{\omega,\omega}}$$

Therefore,

$$\begin{aligned} G^r_{R\sigma k_1 k_2} = {} & g^r_{R\sigma k_1} \delta_{k_1 k_2} + \\ & G^r_{R\sigma k_1} \left(t^*_{R k_2} g^r_{R\sigma k_2} - i\pi t^*_{L\omega} v_{\omega,k_2} g^r_{R\sigma k_2} \right) - \frac{i\pi v_{\omega,k_2} g^r_{R\sigma k_2}}{1 + \pi^2 v^2_{\omega,\omega}} \times \\ & \Big(g^r_{R\sigma k_1} v^*_{\omega,k_1} + G^r_{R\sigma k_1} \left(-i\pi t^*_{R\omega} v^*_{\omega,\omega} - \pi^2 t^*_{L\omega} v^2_{\omega,\omega} \right) \Big) \end{aligned}$$

Now we will deal with the last Green's function $G^<_{R\sigma k_1 k_2}$. In Eq.(8.18), the inverse

$$(I - \Sigma^a g^a_{R\sigma})^{-1}_{k_1 k_2} = \delta_{k_1 k_2} + \frac{i\pi v^*_{\omega,k_1} v_{\omega,k_2} g^a_{R\sigma k_2}}{1 + \pi^2 v^2_{\omega,\omega}}$$

To proceed further, we also need to evaluate the following terms:

$$\begin{aligned} \sum_{k'} G^r_{\sigma k_1 k'} v_{k' k_2} g^<_{R\sigma k_2} &= \sum_{k' k_s} G^r_{R\sigma k_1 k_s} v^*_{k' k_s} g^r_{L\sigma k'} + \\ & \quad \sum_{k'} G^r_{R\sigma k_1} t^*_{L k'} g^r_{L\sigma k'} v_{k' k_2} g^<_{R\sigma k_2} \\ &= -i\pi \sum_{k'} G^r_{R\sigma k_1 k'} v^*_{\omega,k'} v_{\omega,k_2} g^<_{R\sigma k_2} \\ & \quad -i\pi G^r_{R\sigma k_1} t^*_{L\omega} v_{\omega,k_2} g^<_{R\sigma k_2} \end{aligned}$$

and that

$$\begin{aligned}\sum_{k'} G^r_{R\sigma kk'} v^*_{\omega,k'} &= g^r_{R\sigma k} v^*_{\omega,k} - i\pi g^r_{R\sigma k} t^*_{R\omega} v^*_{\omega,\omega} - \pi^2 G^r_{R\sigma k} t^*_{L\omega} v^2_{\omega,\omega} - \\ &\quad \frac{\pi^2 v^2_{\omega,\omega}}{1+\pi^2 v^2_{\omega,\omega}} \times \Big(g^r_{R\sigma k_1} v^*_{\omega,k_1} + G^r_{R\sigma k_1} \times \\ &\quad \left(-i\pi t^*_{R\omega} v^*_{\omega,\omega} - \pi^2 t^*_{L\omega} v^2_{\omega,\omega}\right) \Big) \\ &\equiv Z_k \end{aligned} \tag{8.22}$$

Define $F(k_1,k_2)$ as

$$\begin{aligned} F(k_1,k_2) &= g^<_{R\sigma k_1}\delta_{k_1k_2} + \left(2\pi i f_L(\omega) v_{\omega,k_2} g^a_{R\sigma k_2} - i\pi v_{\omega,k_2} g^<_{R\sigma k_2}\right) Z_{k_1} - \\ &\quad i\pi G^r_{R\sigma k_1} t^*_{L\omega} v_{\omega,k_2} g^<_{R\sigma k_2} + G^r_{R\sigma k_1} t^*_{Rk_2} g^<_{R\sigma k_2} + G^<_{R\sigma k_1} t^*_{Rk_2} g^a_{R\sigma k_2} + \\ &\quad 2\pi i f_L(\omega) G^r_{R\sigma k_1} t^*_{L\omega} v_{\omega,k_2} g^a_{R\sigma k_2} + i\pi G^<_{R\sigma k_1} t^*_{L\omega} v_{\omega,k_2} g^a_{R\sigma k_2} \end{aligned} \tag{8.23}$$

then the Green's function $G^<_{R\sigma k_1 k_2}$ can be written as

$$G^<_{R\sigma k_1 k_2} = F(k_1,k_2) + \sum_{k'} F(k_1,k') v^*_{\omega,k'} \frac{i\pi v_{\omega,k_2} g^a_{R\sigma k_2}}{1+\pi^2 v^2_{\omega,\omega}} \tag{8.24}$$

where, by applying the Plemelj formula we obtain

$$\begin{aligned} \sum_{k'} F(k,k') v^*_{\omega,k'} &= g^<_{R\sigma k} v^*_{\omega,k} + 2\pi^2 Z_k \left(f_R(\omega) - f_L(\omega)\right) v^2_{\omega,\omega} + \\ &\quad 2\pi^2 G^r_{R\sigma k} t^*_{L\omega} \left(f_R(\omega) - f_L(\omega)\right) v^2_{\omega,\omega} + 2\pi i G^r_{R\sigma k} f_R(\omega) t^*_{R\omega} v^*_{\omega,\omega} + \\ &\quad i\pi G^<_{R\sigma k} t^*_{R\omega} v^*_{\omega,\omega} - \pi^2 G^<_{R\sigma k} t^*_{L\omega} v^2_{\omega,\omega} \end{aligned} \tag{8.25}$$

In this way, Eq.(8.24) together with Eq.(8.25) gives the final expression for $G^<_{R\sigma k_1 k_2}$.

Now, we are at the position to finalize the current formula Eq.(8.13). We do this in an easy-to-hard order. First, we evaluate the third term in Eq.(8.13) $\sum_k G^r_{R\sigma k}\Sigma^<_{Lv\sigma k}$. It is

$$\begin{aligned}\sum_k G^r_{R\sigma k}\Sigma^<_{Lv\sigma k} &= 2\pi i G^r_{R\sigma k} f_L(\omega) v_{\omega,k} t^*_{L\omega} \\ &= 2\pi i f_L(\omega) t^*_{L\omega} G^r_\sigma \times \sum_k \Bigg(-i\pi t_{L\omega} v^*_{\omega,k} g^r_{R\sigma k} v_{\omega,k} + t_{Rk} g^r_{R\sigma k} v_{\omega,k} + \\ &\quad \frac{i\pi^3 t_{L\omega} v^2_{\omega,\omega}}{1+\pi^2 v^2_{\omega,\omega}} v^*_{\omega,k} g^r_{R\sigma k} v_{\omega,k} - \frac{\pi^2 t_{R\omega} v_{\omega,\omega}}{1+\pi^2 v^2_{\omega,\omega}} v^*_{\omega,k} g^r_{R\sigma k} v_{\omega,k} \Bigg) \\ &= 2\pi i f_L(\omega) t^*_{L\omega} G^r_\sigma \times \Bigg(-\pi^2 t_{L\omega} v^2_{\omega,\omega} - i\pi t_{R\omega} v_{\omega,\omega} + \\ &\quad \frac{\pi^4 t_{L\omega} v^4_{\omega,\omega}}{1+\pi^2 v^2_{\omega,\omega}} + \frac{i\pi^3 t_{R\omega} v_{\omega,\omega} v^2_{\omega,\omega}}{1+\pi^2 v^2_{\omega,\omega}} \Bigg) \end{aligned} \tag{8.26}$$

At this point, the only unknown is the Green's function of the central dot, which will be derived by SymGF. Hence this is the final form for the purpose of a current formula.

Next, we evaluate the fourth term of Eq.(8.13) $\sum_k G^<_{R\sigma k}\Sigma^a_{Lv\sigma k}$. It is

$$\begin{aligned}\sum_k G^<_{R\sigma k}\Sigma^a_{Lv\sigma k} &= \frac{i\pi t^*_{L\omega}}{1+\pi^2 v^2_{\omega,\omega}} \times \\ &\quad \Big(2\pi^2 t_{L\omega} G^r_\sigma (f_R(\omega) - f_L(\omega)) v^2_{\omega,\omega} - \pi^2 t_{L\omega} G^<_\sigma v^2_{\omega,\omega} - \\ &\quad 2\pi i G^r_\sigma f_R(\omega) t_{R\omega} v_{\omega,\omega} + i\pi G^<_\sigma t_{R\omega} v_{\omega,\omega} + \\ &\quad 2\pi^2 G^r_\sigma (f_R(\omega) - f_L(\omega)) v^2_{\omega,\omega} \times B \Big) \end{aligned} \tag{8.27}$$

where B is defined in Eq.(8.21)

Third, we evaluate the first term in Eq.(8.13) $\sum_{kk'} G^r_{R\sigma kk'}\Sigma^<_{kk'}$. It is

$$\begin{aligned}\sum_{kk'} G^r_{R\sigma kk'}\Sigma^<_{R\sigma kk'} &= 2\pi i f_L(\omega)\sum_{kk'} G^r_{R\sigma kk'} v_{\omega,k} v^*_{\omega,k'}\\ &= 2\pi i f_L(\omega)\sum_k \frac{1}{1+\pi^2 v^2_{\omega,\omega}}\Big(g^r_{R\sigma k} v^*_{\omega,k} +\\ &\quad G^r_{R\sigma k}\left(-i\pi t^*_{R\omega} v^*_{\omega,\omega} - \pi^2 t^*_{L\omega} v^2_{\omega,\omega}\right)\Big) v_{\omega,k}\\ &= 2\pi i f_L(\omega)\frac{1}{1+\pi^2 v^2_{\omega,\omega}}\Big(- i\pi v^2_{\omega,\omega} +\\ &\quad \sum_k G^r_{R\sigma k} v_{\omega,k}\left(-i\pi t^*_{R\omega} v^*_{\omega,\omega} - \pi^2 t^*_{L\omega} v^2_{\omega,\omega}\right)\Big) \qquad (8.28)\end{aligned}$$

where the summation $\sum_k G^r_{R\sigma k} v_{\omega,k}$ has been contained in the evaluated term Eq.(8.26).

Fourth, we evaluate the second term in Eq.(8.13) $\sum_{kk'} G^<_{R\sigma kk'}\Sigma^a_{kk'}$. It is

$$\sum_{kk'} G^<_{R\sigma kk'}\Sigma^a_{kk'} = \sum_{kk'} G^<_{R\sigma kk'} i\pi v_{\omega,k} v^*_{\omega,k'}$$

We first evaluate

$$\begin{aligned}\sum_{k'} G^<_{R\sigma kk'} v^*_{\omega,k'} &= \sum_{k'} F(k,k') v^*_{\omega,k'} + \sum_{k'k_s} F(k,k_s) v^*_{\omega,k_s}\frac{i\pi v_{\omega,k'} g^a_{R\sigma k'}}{1+\pi^2 v^2_{\omega,\omega}} v^*_{\omega,k'}\\ &\quad \sum_{k'} F(k,k') v^*_{\omega,k'}\frac{1}{1+\pi^2 v^2_{\omega,\omega}}\end{aligned}$$

where we have defined F in Eq.(8.23) and evaluated $\sum_{k'} F(k,k') v^*_{\omega,k'}$ in Eq.(8.25).

Then, we can write

$$\begin{aligned}\sum_{kk'} G^<_{R\sigma kk'}\Sigma^a_{kk'} &= \sum_{kk'} G^<_{R\sigma kk'} i\pi v_{\omega,k} v^*_{\omega,k'} \\ &= \frac{i\pi}{1+\pi^2 v^2_{\omega,\omega}} \sum_{kk'} F(k,k') v^*_{\omega,k'} v_{\omega,k} \\ &= 2\pi^2 i f_R(\omega) v^2_{\omega,\omega} + 2\pi^2 \left(f_R(\omega) - f_L(\omega)\right) v^2_{\omega,\omega} \sum_k Z_k v_{\omega,k} + \\ &\quad 2\pi^2 t^*_{L\omega} \left(f_R(\omega) - f_L(\omega)\right) v^2_{\omega,\omega} \sum_k G^r_{R\sigma k} v_{\omega,k} + \\ &\quad 2\pi i f_R(\omega) v^*_{\omega,\omega} t^*_{R\omega} \sum_k G^r_{R\sigma k} v_{\omega,k} + i\pi v^*_{\omega,\omega} t^*_{R\omega} \sum_k G^<_{R\sigma k} v_{\omega,k} - \\ &\quad \pi^2 t^*_{L\omega} v^2_{\omega,\omega} \sum_k G^<_{R\sigma k} v_{\omega,k} \end{aligned} \tag{8.29}$$

In the above expression, all the summations have been evaluated in previous terms except $\sum_k Z_k v_{\omega,k}$ [see Eq.(8.22)] which is:

$$\begin{aligned}\sum_k Z_k v_{\omega,k} = \Big(& - i\pi v^2_{\omega,\omega} - i\pi t^*_{R\omega} v^*_{\omega,\omega} \sum_k G^r_{R\sigma k} v_{\omega,k} - \\ & \pi^2 t^*_{L\omega} v^2_{\omega,\omega} \sum_k G^r_{R\sigma k} v_{\omega,k}\Big) \frac{1}{1+\pi^2 v^2_{\omega,\omega}} \end{aligned} \tag{8.30}$$

This completes the evaluation of the fourth term.

The last term is $\sum_k G^<_{L\sigma k} t^*_{Lk}$. With identical method, we have

$$\begin{aligned}\sum_k G^<_{L\sigma k} t{*}_{Lk} &= 2\pi^2 G^r_\sigma t_{R\omega} t^*_{L\omega} v_{\omega,\omega} \left(f_L(\omega) - f_R(\omega)\right) - \pi^2 t_{R\omega} t^*_{L\omega} v_{\omega,\omega} G^<_\sigma + \\ &\quad 2\pi i f_L(\omega) t^2_{L\omega} G^r_\sigma + 2\pi^2 \left(f_L(\omega) - f_R(\omega)\right) v_{\omega,\omega} t^*_{L\omega} G^r_\sigma C + \\ &\quad i\pi t^2_{L\omega} G^<_\sigma + \pi^2 G^r_\sigma t_{R\omega} v^2_{\omega,\omega} \left(f_L(\omega) - f_R(\omega)\right) - \pi^2 t_{R\omega} v^2_{\omega,\omega} G^<_\sigma + \\ &\quad 2\pi i f_L(\omega) t_{L\omega} v^*_{\omega,\omega} G^r_\sigma + 2\pi^2 \left(f_L(\omega) - f_R(\omega)\right) v^2_{\omega,\omega} G^r_\sigma C + \\ &\quad i\pi t_{L\omega} v^*_{\omega,\omega} G^<_\sigma \end{aligned} \tag{8.31}$$

where we have defined

$$C \equiv \left(-\pi^2 t_{R\omega} v_{\omega,\omega}^2 - i\pi v_{\omega,\omega}^* t_{L\omega} + \frac{\pi^4 v_{\omega,\omega}^4 t_{R\omega}}{1+\pi^2 v_{\omega,\omega}^2} + \frac{i\pi^3 v_{\omega,\omega}^2 v_{\omega,\omega}^* t_{L\omega}}{1+\pi^2 v_{\omega,\omega}^2} \right)$$

With the above derivations, we have completely rewritten the current formula Eq.(8.13) in terms of the Green's function of the central dot (G_σ^r and $G_\sigma^<$) and parameters that are given in the Hamiltonian.

8.2 Appendix B: Retarded Green's Function of the Side-Coupled Double Quantum Dot

In this and the following sections of the appendix, we list the analytical formula of the Green's functions derived by SymGF for the DQD device and some detailed algorithm of SymGF.

For the DQD device model of Eq.(3.24) (Fig.3.3) and Rule (4.1-4.3), SymGF derived a total of 133 EOMs (for 133 Green's functions). In SymGF, all the Green's functions, self-energies and un-perturbed Green's functions (considered to be known) are automatically indexed with numerical subscripts, for example, G_{107} means the 107'th Green's function. SymGF did further mathematical manipulation to reduce the 133 EOMs to a four-equation set of G_1, G_6, G_7 and G_{107}. All the Green's functions are functions of energy but the energy subscript ω is omitted in the following for simplicity of notation. In particular, G_1 is the retarded Green's function G^r for the DQD device which is used in calculating the transport properties in Eq.(2.4). In general all the Green's functions are matrices of the same dimension as the corresponding sub-Hilbert space. In the present DQD problem, each QD is considered to have a single energy level, the dimension of the Hilbert spaces for the dots is one. G_1, G_6, G_7 and G_{107} are derived by SymGf to be the following:

$$G_1 = g_1\left(1 + G_1\left(\Gamma_{16} + \Sigma_{20} + \Sigma_{21}\right) + U\left(-G_6 + G_7\right)\Gamma_{17} g_2\right) \tag{8.32}$$

$$G_6 = g_1\left(-G_7\Gamma_{32} + G_6\left(\Gamma_{1178} + \Gamma_{32} + \Gamma_{605}\right) + G_1\Gamma_{31} g_5\right) \tag{8.33}$$

$$\begin{aligned} G_7 = g_1\Big(& -G_6(\Gamma_{32} + U\Gamma_{1231} g_2) + G_7(\Gamma_{1426} + \Gamma_{1606} + \Gamma_{32} + U\Gamma_{1231} g_2) + \\ & G_1(\Gamma_{1229} + \Gamma_{31} g_5)\Big) \end{aligned} \tag{8.34}$$

$$\begin{aligned} G_{107} = g_1\Big(& (1 - N^a_\uparrow) G_1\Gamma_{16} + G_{107}\left(\Gamma_{1827} + \Gamma_{2012}\right) - \\ & U\left(G_6 - G_7\right)\left(\Gamma_{16} - N^a_\uparrow\Gamma_{17}\right) g_2\Big) \end{aligned} \tag{8.35}$$

where variables beginning with Γ or Σ are self-energies defined by SymGF during the solution of the original set of EOM, the variables beginning with g are for Green's functions of QD-1, QD-2 (see Fig.3.3) and the leads when they are isolated from each other [see Eqs.(8.38-8.41)].

In Eqs.(8.32, 8.33, 8.34, 8.35), the self-energies are defined as:

$$
\begin{aligned}
\Gamma_{16} &= \Big(\Sigma_1\left(1-(\Gamma_3+\Gamma_7)g_6+g_5\left(U(\Gamma_2+\Gamma_6)g_6-\Sigma_3\right)\right)\Big)\Bigg/\Bigg(\Big(1-(\Gamma_3+ \\
&\qquad \Gamma_7)g_6+g_5\left(U(\Gamma_2+\Gamma_6)g_6-\Sigma_3\right)\Big)-Ug_2g_5\left((1-N_\downarrow^a)\Sigma_3+(\Gamma_1+\Gamma_5)g_6\right)\Bigg) \\
\Gamma_{17} &= \Sigma_2\Big/\Big(1-\Gamma_3g_6-\Gamma_7g_6-g_5\left(\Sigma_3-U(\Gamma_2+\Gamma_6)g_6\right)- \\
&\qquad (Ug_2g_5\Sigma_3-N_\downarrow^a\Sigma_3+\Gamma_1g_6+\Gamma_5g_6)\Big) \\
\Gamma_{31} &= \frac{\Sigma_1\left((N_\downarrow^a-1)\Sigma_3+(\Gamma_{20}+\Gamma_{24})g_6\right)}{\left((1-(\Gamma_{22}+\Gamma_{26})g_6)-g_5\left(\Sigma_3(1-N_\downarrow^a)U\Sigma_3g_2+U(\Gamma_{21}+\Gamma_{25})g_6\right)\right)} \\
\Gamma_{32} &= \frac{\Sigma_2}{1-\Gamma_{22}g_6-\Gamma_{26}g_6-g_5\left(\Sigma_3+U\Sigma_3g_2-N_\downarrow^aU\Sigma_3g_2+U\Gamma_{21}g_6+U\Gamma_{25}g_6\right)} \\
\Gamma_{1229} &= \frac{A}{1-C} \\
\Gamma_{1231} &= \frac{B}{1+C}
\end{aligned}
\tag{8.36}
$$

where variables $A-C$ are defined for a better readability:

$$
\begin{aligned}
A &= \frac{(1-N_\downarrow^a)\Sigma_1}{1-\frac{U(\Gamma_{1182}+\Gamma_{1187})g_2g_5g_6}{(1-\Gamma_{1184}g_6-\Gamma_{1189}g_6)+g_5(-\Sigma_3+U\Gamma_{1183}g_6+U\Gamma_{1188}g_6)}} \\
B &= \frac{(1-N_\downarrow^a)\Sigma_2}{1-\frac{U(\Gamma_{1182}+\Gamma_{1187})g_2g_5g_6}{1-\Gamma_{1184}g_6-\Gamma_{1189}g_6}+\frac{g_5(-\Sigma_3+U\Gamma_{1183}g_6+U\Gamma_{1188}g_6)}{1-\Gamma_{1184}g_6-\Gamma_{1189}g_6}} \\
C &= \frac{(1-N_\downarrow^a)Ug_2g_5\left(\Sigma_3+\Gamma_{1181}g_6+\Gamma_{1186}g_6\right)/\left(1-g_6(\Gamma_{1184}+\Gamma_{1189})\right)}{\left(1-\frac{g_5(\Sigma_3-Ug_6(\Gamma_{1183}+\Gamma_{1188}))}{1-\Gamma_{1184}g_6-\Gamma_{1189}g_6}\right)-U\left(\Gamma_{1182}+\Gamma_{1187}\right)g_2g_5g_6}
\end{aligned}
\tag{8.37}
$$

The un-perturbed Green's functions and self-energies in Eq.(8.36, 8.37) are defined in the following. g_i's are the un-perturbed Green's functions which are:

$$g_1 = \frac{1}{w - \epsilon_0} \tag{8.38}$$

$$g_2 = \frac{1}{-U + w - \epsilon_d} \tag{8.39}$$

$$g_5 = \frac{1}{w - \epsilon_d} \tag{8.40}$$

$$g_6 = \frac{1}{-U + w + \epsilon_a - 2\epsilon_d} \tag{8.41}$$

They are all functions of energy ω, and ω should be interpreted as $\omega + i0^+$ where 0^+ denotes a positive infinitesimal. The self-energies in Eq.(8.36, 8.37) are:

$$\Sigma_1 = \frac{t^2}{-U + w - \epsilon_d}$$

$$\Sigma_2 = \frac{t^2}{w - \epsilon_d}$$

$$\Sigma_3 = \frac{t^2}{-U + w + \epsilon_a - 2\epsilon_d}$$

$$\Gamma_1 = \left(t^2(N^a_\downarrow - f_{l\downarrow}(k))t_l(k)^2(w - \epsilon_a - \epsilon_d + \epsilon_{l\downarrow}(k))\right) \Bigg/ \Bigg(t^2((-2 + N^a_\uparrow + N^a_\downarrow)U + 2(w - \epsilon_a - \epsilon_d)) - (w - \epsilon_a - \epsilon_d)(U - w + \epsilon_a + \epsilon_d)(U - w + 2\epsilon_d) - \epsilon_{l\downarrow}(k)\Bigg(- 2t^2 + U^2 + (3w - \epsilon_a - 5\epsilon_d)(w - \epsilon_a - \epsilon_d) + U(-4w + 3\epsilon_a + 5\epsilon_d) + \epsilon_{l\downarrow}(k)(-2U + 3w - 2(\epsilon_a + 2\epsilon_d) + \epsilon_{l\downarrow}(k))\Bigg)\Bigg)$$

$$\begin{aligned}\Gamma_2 = \big(t^2(N^a_\downarrow - f_{l\downarrow}(k))t_l(k)^2\big) \Bigg/ \Big(&- t^2((-2 + N^a_\uparrow + N^a_\downarrow)U + 2(w - \epsilon_a - \epsilon_d)) + \\ &(w - \epsilon_a - \epsilon_d)(U - w + \epsilon_a + \epsilon_d)(U - w + 2\epsilon_d) + \big(- 2t^2 + U^2 - 4Uw + \\ &3w^2 + 3U\epsilon_a - 4w\epsilon_a + \epsilon_a^2 + 5U\epsilon_d - 8w\epsilon_d + 6\epsilon_a\epsilon_d + 5\epsilon_d^2\big)\epsilon_{l\downarrow}(k) - \\ &(2U - 3w + 2\epsilon_a + 4\epsilon_d)\epsilon_{l\downarrow}(k)^2 + \epsilon_{l\downarrow}(k)^3\Big)\end{aligned}$$

$$\begin{aligned}\Gamma_3 = -(t_l(k)^2(U - w + \epsilon_a + \epsilon_d - \epsilon_{l\downarrow}(k))(w - \epsilon_a - \epsilon_d + \epsilon_{l\downarrow}(k))) \Bigg/ \Big(&- t^2 \times \\ &\big((N^a_\uparrow + N^a_\downarrow - 2)U + 2(w - \epsilon_a - \epsilon_d)\big) + (w - \epsilon_a - \epsilon_d)(U - w + \epsilon_a + \epsilon_d) \times \\ &(U - w + 2\epsilon_d) + \big(U^2 - 2t^2 - 4Uw + 3w^2 + 3U\epsilon_a - 4w\epsilon_a + \epsilon_a^2 + 5U\epsilon_d - \\ &8w\epsilon_d + 6\epsilon_a\epsilon_d + 5\epsilon_d^2\big)\epsilon_{l\downarrow}(k) - (2U - 3w + 2\epsilon_a + 4\epsilon_d)\epsilon_{l\downarrow}(k)^2 + \epsilon_{l\downarrow}(k)^3\Big)\end{aligned}$$

$$\begin{aligned}\Gamma_{20} = \big(t^2(N^a_\downarrow - f_{l\downarrow}(k))t_l(k)^2(w - \epsilon_a - \epsilon_d + \epsilon_{l\downarrow}(k))\big) \Bigg/ \Big(&t^2\big((2 - N^a_\uparrow - N^a_\downarrow)U - \\ &2(w - \epsilon_a - \epsilon_d)\big) + (w - \epsilon_a - \epsilon_d)(U - w + \epsilon_a + \epsilon_d)(U - w + 2\epsilon_d) + \\ &\big(- 2t^2 + U^2 - 4Uw + 3w^2 + 3U\epsilon_a - 4w\epsilon_a + \epsilon_a^2 + 5U\epsilon_d - 8w\epsilon_d + \\ &6\epsilon_a\epsilon_d + 5\epsilon_d^2\big)\epsilon_{l\downarrow}(k) - (2U - 3w + 2\epsilon_a + 4\epsilon_d)\epsilon_{l\downarrow}(k)^2 + \epsilon_{l\downarrow}(k)^3\Big)\end{aligned}$$

$$\begin{aligned}\Gamma_{21} = -\big(t^2(N^a_\downarrow - f_{l\downarrow}(k))t_l(k)^2(U - 2w + \epsilon_a + 2\epsilon_d - \epsilon_{l\downarrow}(k))\big) \Bigg/ \Big(&(U - w + \epsilon_d) \\ &\big(- t^2((-2 + N^a_\uparrow + N^a_\downarrow)U + 2(w - \epsilon_a - \epsilon_d)) + (U - w + \epsilon_a + \epsilon_d) \times \\ &(w - \epsilon_a - \epsilon_d)(U - w + 2\epsilon_d) + \big(- 2t^2 + U^2 - 4Uw + 3w^2 + 3U\epsilon_a - \\ &4w\epsilon_a + \epsilon_a^2 + 5U\epsilon_d - 8w\epsilon_d + 6\epsilon_a\epsilon_d + 5\epsilon_d^2\big)\epsilon_{l\downarrow}(k) - (2U - 3w + 2\epsilon_a + \\ &4\epsilon_d)\epsilon_{l\downarrow}(k)^2 + \epsilon_{l\downarrow}(k)^3\big)\Big)\end{aligned}$$

$$\begin{aligned}\Gamma_{22} = {}& -(t_l(k)^2(U - w + \epsilon_a + \epsilon_d - \epsilon_{l\downarrow}(k))(w - \epsilon_a - \epsilon_d + \epsilon_{l\downarrow}(k)))\Bigg/\Big(t^2\Big((2 - \\ & N^a_\uparrow - N^a_\downarrow)U - 2(w - \epsilon_a - \epsilon_d)\Big) + (w - \epsilon_a - \epsilon_d)(U - w + \epsilon_a + \epsilon_d) \times \\ & (U - w + 2\epsilon_d) + \big(- 2t^2 + U^2 - 4Uw + 3w^2 + 3U\epsilon_a - 4w\epsilon_a + \epsilon_a^2 + \\ & 5U\epsilon_d - 8w\epsilon_d + 6\epsilon_a\epsilon_d + 5\epsilon_d^2\big)\epsilon_{l\downarrow}(k) - (2U - 3w + 2\epsilon_a + 4\epsilon_d)\epsilon_{l\downarrow}(k)^2 + \\ & \epsilon_{l\downarrow}(k)^3\Big)\end{aligned}$$

$$\begin{aligned}\Gamma_{605} = {}& t_l(k)^2\Bigg/\Bigg((w - \epsilon_{l\uparrow}(k))\Bigg(1 + 2t^2\Big((1 - N^d_\uparrow)U^2 - w^2 - 2(1 - N^d_\uparrow)U(\epsilon_a - \\ & \epsilon_d) + (\epsilon_a - \epsilon_d)^2 + 2w\epsilon_{l\uparrow}(k) - \epsilon_{l\uparrow}(k)^2\Big)\Big/\Big((w + \epsilon_a - \epsilon_d - \epsilon_{l\uparrow}(k))(w - U + \\ & \epsilon_a - \epsilon_d - \epsilon_{l\uparrow}(k))(w - \epsilon_a + \epsilon_d - \epsilon_{l\uparrow}(k))(U + w - \epsilon_a + \epsilon_d - \epsilon_{l\uparrow}(k))\Big) - \\ & \big(4(N^a_\downarrow - 1)(N^a_\uparrow - N^d_\uparrow)t^4U^2(U - 2\epsilon_a + 2\epsilon_d)^2\big)\Big/\Big((U + w - \epsilon_a + \epsilon_d - \\ & \epsilon_{l\uparrow}(k))(U - w - \epsilon_a + \epsilon_d + \epsilon_{l\uparrow}(k))\big(2t^2 + (U - w - \epsilon_a + \epsilon_d)(U + w - \\ & \epsilon_a + \epsilon_d) + 2w\epsilon_{l\uparrow}(k) - \epsilon_{l\uparrow}(k)^2\big)\big(w^2 - (\epsilon_a - \epsilon_d)^2 - 2w\epsilon_{l\uparrow}(k) + \\ & \epsilon_{l\uparrow}(k)^2\big)^2\Big)\Bigg)\Bigg)\end{aligned}$$

$$\begin{aligned}\Gamma_{1181} = {}& -\Big(t^2 t_l(k)^2(w - \epsilon_a - \epsilon_d + \epsilon_{l\downarrow}(k))\Big)\Bigg/\Big(t^2((-2 + N^a_\uparrow + N^a_\downarrow)U + 2(w - \\ & \epsilon_a - \epsilon_d)) - (w - \epsilon_a - \epsilon_d)(U - w + \epsilon_a + \epsilon_d)(U - w + 2\epsilon_d) + \big(2t^2 - U^2 + \\ & 4Uw - 3w^2 - 3U\epsilon_a + 4w\epsilon_a - \epsilon_a^2 - 5U\epsilon_d + 8w\epsilon_d - 6\epsilon_a\epsilon_d - 5\epsilon_d^2\big)\epsilon_{l\downarrow}(k) + \\ & (2U - 3w + 2\epsilon_a + 4\epsilon_d)\epsilon_{l\downarrow}(k)^2 - \epsilon_{l\downarrow}(k)^3\Big)\end{aligned}$$

$$\begin{aligned}\Gamma_{1182} = {} & \big(t^2(-1+f_{l\downarrow}(k))t_l(k)^2(w-\epsilon_a-\epsilon_d+\epsilon_{l\downarrow}(k))\big)\Big/\Big(t^2((2-N^a_\uparrow-N^a_\downarrow)U- \\ & 2(w-\epsilon_a-\epsilon_d))+(w-\epsilon_a-\epsilon_d)(U-w+\epsilon_a+\epsilon_d)(U-w+2\epsilon_d)+\big(U^2- \\ & 2t^2-4Uw+3w^2+3U\epsilon_a-4w\epsilon_a+\epsilon_a^2+5U\epsilon_d-8w\epsilon_d+6\epsilon_a\epsilon_d+5\epsilon_d^2\big)\times \\ & \epsilon_{l\downarrow}(k)-(2U-3w+2\epsilon_a+4\epsilon_d)\epsilon_{l\downarrow}(k)^2+\epsilon_{l\downarrow}(k)^3\Big)\end{aligned}$$

$$\begin{aligned}\Gamma_{1183} = {} & \big(t^2(N^a_\downarrow-f_{l\downarrow}(k))t_l(k)^2\big)\,/\Big(-t^2((-2+N^a_\uparrow+N^a_\downarrow)U+2(w-\epsilon_a-\epsilon_d))+ \\ & (w-\epsilon_a-\epsilon_d)(U-w+\epsilon_a+\epsilon_d)(U-w+2\epsilon_d)+\big(-2t^2+U^2-4Uw+ \\ & 3w^2+3U\epsilon_a-4w\epsilon_a+\epsilon_a^2+5U\epsilon_d-8w\epsilon_d+6\epsilon_a\epsilon_d+5\epsilon_d^2\big)\epsilon_{l\downarrow}(k)- \\ & (2U-3w+2\epsilon_a+4\epsilon_d)\epsilon_{l\downarrow}(k)^2+\epsilon_{l\downarrow}(k)^3\Big)\end{aligned}$$

$$\begin{aligned}\Gamma_{1184} = {} & -(t_l(k)^2(U-w+\epsilon_a+\epsilon_d-\epsilon_{l\downarrow}(k))(w-\epsilon_a-\epsilon_d+\epsilon_{l\downarrow}(k)))\Big/\Big(t^2((2- \\ & N^a_\uparrow-N^a_\downarrow)U-2(w-\epsilon_a-\epsilon_d))+(w-\epsilon_a-\epsilon_d)(U-w+\epsilon_a+\epsilon_d)\times \\ & (U-w+2\epsilon_d)+\big(-2t^2+U^2-4Uw+3w^2+3U\epsilon_a-4w\epsilon_a+\epsilon_a^2+ \\ & 5U\epsilon_d-8w\epsilon_d+6\epsilon_a\epsilon_d+5\epsilon_d^2\big)\epsilon_{l\downarrow}(k)-(2U-3w+2\epsilon_a+4\epsilon_d)\epsilon_{l\downarrow}(k)^2+ \\ & \epsilon_{l\downarrow}(k)^3\Big)\end{aligned}$$

$$\begin{aligned}\Gamma_{1205} = {} & -(t^2t_l(k)^2(w-\epsilon_a-\epsilon_d+\epsilon_{l\downarrow}(k)))\Big/\Big(t^2((-2+N^a_\uparrow+N^a_\downarrow)U+2(w- \\ & \epsilon_a-\epsilon_d))-(w-\epsilon_a-\epsilon_d)(U-w+\epsilon_a+\epsilon_d)(U-w+2\epsilon_d)+\big(2t^2-U^2+ \\ & 4Uw-3w^2-3U\epsilon_a+4w\epsilon_a-\epsilon_a^2-5U\epsilon_d+8w\epsilon_d-6\epsilon_a\epsilon_d-5\epsilon_d^2\big)\epsilon_{l\downarrow}(k)+ \\ & (2U-3w+2\epsilon_a+4\epsilon_d)\epsilon_{l\downarrow}(k)^2-\epsilon_{l\downarrow}(k)^3\Big)\end{aligned}$$

$$\begin{aligned}\Gamma_{1206} = {}& -(t^2(-1+f_{l\downarrow}(k))t_l(k)^2(w-\epsilon_a-\epsilon_d+\epsilon_{l\downarrow}(k)))\Bigg/\Big(t^2((2-N^a_\uparrow-N^a_\downarrow)U-\\ & 2(w-\epsilon_a-\epsilon_d))+(w-\epsilon_a-\epsilon_d)(U-w+\epsilon_a+\epsilon_d)(U-w+2\epsilon_d)+\\ & \big(-2t^2+U^2-4Uw+3w^2+3U\epsilon_a-4w\epsilon_a+\epsilon_a^2+5U\epsilon_d-8w\epsilon_d+6\epsilon_a\epsilon_d+\\ & 5\epsilon_d^2\big)\epsilon_{l\downarrow}(k)-(2U-3w+2\epsilon_a+4\epsilon_d)\epsilon_{l\downarrow}(k)^2+\epsilon_{l\downarrow}(k)^3\Big)\end{aligned}$$

$$\begin{aligned}\Gamma_{1207} = {}& (t^2(-N^a_\downarrow+f_{l\downarrow}(k))t_l(k)^2)\Bigg/\Big(-t^2((-2+N^a_\uparrow+N^a_\downarrow)U+2(w-\epsilon_a-\epsilon_d))+\\ & (w-\epsilon_a-\epsilon_d)(U-w+\epsilon_a+\epsilon_d)(U-w+2\epsilon_d)+\big(-2t^2+U^2-\\ & 4Uw+3w^2+3U\epsilon_a-4w\epsilon_a+\epsilon_a^2+5U\epsilon_d-8w\epsilon_d+6\epsilon_a\epsilon_d+5\epsilon_d^2\big)\epsilon_{l\downarrow}(k)-\\ & (2U-3w+2\epsilon_a+4\epsilon_d)\epsilon_{l\downarrow}(k)^2+\epsilon_{l\downarrow}(k)^3\Big)\end{aligned}$$

$$\begin{aligned}\Gamma_{1208} = {}& -(t_l(k)^2(U-w+\epsilon_a+\epsilon_d-\epsilon_{l\downarrow}(k))(w-\epsilon_a-\epsilon_d+\epsilon_{l\downarrow}(k)))\Bigg/\Big(t^2((2-\\ & N^a_\uparrow-N^a_\downarrow)U-2(w-\epsilon_a-\epsilon_d))+(w-\epsilon_a-\epsilon_d)(U-w+\epsilon_a+\epsilon_d)(U-\\ & w+2\epsilon_d)+\big(-2t^2+U^2-4Uw+3w^2+3U\epsilon_a-4w\epsilon_a+\epsilon_a^2+5U\epsilon_d-\\ & 8w\epsilon_d+6\epsilon_a\epsilon_d+5\epsilon_d^2\big)\epsilon_{l\downarrow}(k)-\\ & (2U-3w+2\epsilon_a+4\epsilon_d)\epsilon_{l\downarrow}(k)^2+\epsilon_{l\downarrow}(k)^3\Big)\end{aligned}$$

$$\begin{aligned}\Gamma_{1426} = {}& t_l(k)^2\Bigg/\Bigg(w-\epsilon_{l\downarrow}(k)+t^2\bigg(\frac{-1+N^a_\downarrow}{w+\epsilon_a-\epsilon_d-\epsilon_{l\downarrow}(k)}+\\ & \frac{-1+N^a_\uparrow}{w-\epsilon_a+\epsilon_d-\epsilon_{l\downarrow}(k)}-\frac{N^a_\uparrow}{U+w-\epsilon_a+\epsilon_d-\epsilon_{l\downarrow}(k)}+\\ & \frac{N^a_\downarrow}{U-w-\epsilon_a+\epsilon_d+\epsilon_{l\downarrow}(k)}\bigg)\Bigg)\end{aligned}$$

$$\begin{aligned}
\Gamma_{1827} = {} & \frac{t_l(k)^2}{w-\epsilon_{l\uparrow}(k)} \Bigg/ \Bigg(1 + \frac{2t^2}{(U-\epsilon_a+\epsilon_d)^2 - (w-\epsilon_{l\uparrow}(k))^2} - \\
& \big(4(-1+N^a_\downarrow)(N^a_\uparrow - N^d_\uparrow) t^4 U^2 (U-2\epsilon_a+2\epsilon_d)^2\big) \Big/ \\
& \Big(\big(U^2 - w^2 - 2U\epsilon_a + \epsilon_a^2 + 2U\epsilon_d - 2\epsilon_a\epsilon_d + \epsilon_d^2 + 2w\epsilon_{l\uparrow}(k) - \epsilon_{l\uparrow}(k)^2\big) \\
& \big(w^2 - (\epsilon_a-\epsilon_d)^2 - 2w\epsilon_{l\uparrow}(k) + \epsilon_{l\uparrow}(k)^2\big) \Big(2t^2\Big((-1+N^d_\uparrow)U^2 + w^2 - \\
& 2(-1+N^d_\uparrow)U(\epsilon_a-\epsilon_d) - (\epsilon_a-\epsilon_d)^2\Big) + \big(w^2-(\epsilon_a-\epsilon_d)^2\big) \times \\
& \big(U^2 - w^2 - 2U(\epsilon_a-\epsilon_d) + (\epsilon_a-\epsilon_d)^2\big) - \\
& 2w\big(2t^2+U^2-2U(\epsilon_a-\epsilon_d)+2\big(-w^2+\epsilon_a^2-2\epsilon_a\epsilon_d+\epsilon_d^2\big)\big)\epsilon_{l\uparrow}(k) + \\
& \big(2t^2+U^2-2U(\epsilon_a-\epsilon_d)+2\big(-3w^2+\epsilon_a^2-2\epsilon_a\epsilon_d+\epsilon_d^2\big)\big)\epsilon_{l\uparrow}(k)^2 + \\
& 4w\epsilon_{l\uparrow}(k)^3 - \epsilon_{l\uparrow}(k)^4\Big)\Big)\Bigg)
\end{aligned}$$

There are more self-energies in Eq.(8.36, 8.37), they can be obtained by replacing the $\epsilon_{l\sigma}$ with $\epsilon_{r\sigma}$ in their corresponding counterparts. For instance, Γ_5 is obtained from Γ_1 by replacing $\epsilon_{l\sigma}$ with $\epsilon_{r\sigma}$; Γ_6 is obtained from Γ_2; Γ_7 from Γ_3; Γ_{24} from Γ_{20}; Γ_{25} from Γ_{21}; Γ_{26} from Γ_{22}; Γ_{1178} from Γ_{605}; Γ_{1186} from Γ_{1181}; Γ_{1187} from Γ_{1182}; Γ_{1188} from Γ_{1183}; and finally Γ_{1189} from Γ_{1184}. This way, all the quantities in Eqs.(8.32, 8.33, 8.34, 8.35) can be obtained.

8.3 Appendix C: Solution of $G^<$

In the main text we have used the formula $G^< = G^r\Sigma^<G^a$ and this ansatz[51] for calculating $\Sigma^<$

$$\Sigma^< = \frac{\Sigma_0^<}{\Sigma_0^r - \Sigma_0^a}\left[(G^a)^{-1} - (G^r)^{-1}\right] \tag{8.42}$$

to obtain the occupation number as Eq.(3.22). This ansatz was obtained by assuming $\Sigma^{<,>}$ has the form $\Sigma^{<} = \Sigma_0^{<} A$ and $\Sigma^{>} = \Sigma_0^{>} A$, and A is determined by the condition

$$\Sigma^{<} - \Sigma^{>} = \Sigma^{r} - \Sigma^{a}.$$

This ansatz has the advantage of preserving the conservation of current[51].

To have a clearer picture of this ansatz, let's consider an energy-dependent Green's function in Hartree's approximation:

$$G^{r}(\omega) = \frac{1}{\omega - H - \Sigma^{r}(\omega)}.$$

In this way, Eq.(3.23) [or Eq.(8.42)] can be further written as the average of the $G^{<}$'s obtained at each of the leads' chemical potential,

$$G^{<}(\omega) = -i \sum_i w_i f(\omega - \mu_i) G^{r}(\omega) \equiv \sum_i w_i G_i^{<}(\omega),$$

where i enumerates the leads, μ_i is the chemical potential of lead-i, f is the Fermi distribution function and the normalized weight w_i is from each lead's linewidth function Γ_i. This expression suggests that the ansatz works best for not too large bias potential (where μ_i's are not too far from each other) or smooth spectrum (where $G^{r}(\omega)$ doesn't change rapidly with respect to ω). Therefore, caution should be taken when applying the current version of SymGF for situations of large bias or spiky DOS spectrum[87]. For wide range of practical systems where the leads are made of good metals and the central device region is well coupled to the leads, the ansatz can be applied.

8.4 Appendix D: Self-Energies of the Leads

When we solve for the Green's function of QD-1 in Fig.3.3, the influences from the leads are represented by a self-energy function, thus eliminating the degrees of freedom from the leads. SymGF always assumes that the leads have a continuous spectrum, therefore the summation over the lead's quantum numbers becomes integration. During the solution of the desired Green's functions, SymGF automatically recognizes the self-energies contributed from the leads and other parts of the device system. In this appendix we discuss how SymGF calculates the self-energies of the leads. To make the discussion more general, we do not adopt the wide-band limit (WBL) approximation here.

The simplest self-energies are in the following form:

$$\Sigma_\alpha(\omega) \equiv \sum_k \frac{t_{\alpha k} t^*_{\alpha k}}{\omega - \epsilon_{\alpha k}}, \tag{8.43}$$

where summation over k should be understood as integration and ω as $\omega + i0^+$. By applying Plemelj formula[50], Eq.(8.43) becomes:

$$\Sigma_\alpha(\omega) = P \sum_k \frac{t_{\alpha k} t^*_{\alpha k}}{\omega - \epsilon_{\alpha k}} - i\pi \sum_k \delta(\omega - \epsilon_{\alpha K}) t_{\alpha k} t^*_{\alpha k}, \tag{8.44}$$

where P denotes principal value. The first term of Eq.(8.44) is a real number and represents an energy shift. If we adopt WBL, the real principal value is strictly zero and in SymGF this real number is abandoned. The second term is purely imaginary. It represents the transition rate of the electrons to and from the leads, and therefore affects transport properties. SymGF only keeps this imaginary part for the self-energies. In this way, the infinite degrees of freedom of the leads (denoted by the subscript k) is reduced to a function of ω that has the same sub-Hilbert space dimension of the Green's function of the QD-1 (which is one for single level).

One of the more complicated self-energies looks like:

$$\sum_k \frac{\left(f(\epsilon_{Lk}) - N^a_\downarrow\right)\Sigma_1(k)}{\omega - U - \epsilon_a - \epsilon_d + \epsilon_{Lk} - 2\Sigma_2(k) + \frac{(2 - N^a_\uparrow - N^a_\downarrow)U\Sigma_2(k)}{\epsilon_a - \epsilon_d - \epsilon_{Lk}}} \tag{8.45}$$

where f is the Fermi distribution function and $\Sigma_1(k)$ and $\Sigma_2(k)$ are:

$$\begin{aligned}\Sigma_1(k) &\equiv \frac{1}{2\pi}\Sigma_2(k) t_{\alpha k} t^*_{\alpha k} \\ \Sigma_2(k) &\equiv \frac{t^2}{\omega - U - 2\epsilon_d + \epsilon_{Lk}} \ .\end{aligned}$$

It represents the self-energy from the left lead to the QD-1 that has already been affected by the self-energy from the dangling dot QD-2. To carry out the integration, we have to choose a contour so that the poles of ϵ_{Lk} which are infinitesimally close to the real axis (offset by $i0^+$) be surrounded by a semi-circle in the half plane that doesn't contain the poles. This self-energy Eq.(8.45) has three poles. If we have just one such pole, then we end up with the Plemelj formula. After applying the residue theorem, the integrand becomes the product of a Dirac delta function and another part, so that this self-energy is still a function of energy ω. If we further go to even higher orders in the equation of motion iteration, this "self-energy to self-energy" loop will go on. But eventually, all the degrees of freedom of the leads (and of QD-2 as well) are eliminated. Some of this more complicated self-energies are energy-dependent even when we adopt the WBL approximation.

8.5 Appendix E: Superconducting Leads

In recent years, quantum transport in devices having one or more superconducting leads has received tremendous attention[88, 89, 90, 91, 92, 93]. It is not difficult to extend the SymGF method to these systems.

So far in this thesis, the Hamiltonian for a non-interacting normal lead is given as:

$$H = \sum_{k\sigma} \epsilon_{k\sigma} c_{k\sigma}^{\dagger} c_{k\sigma} \tag{8.46}$$

where σ is the spin index. For a superconductor lead, its Hamiltonian is[94, 95, 96]:

$$H = \sum_{k\sigma} \epsilon_k c_{k\sigma}^{\dagger} c_{k\sigma} + \sum_{k} \left[\Delta c_{-k\uparrow}^{\dagger} c_{k\downarrow}^{\dagger} + \Delta^* c_{k\downarrow} c_{-k\uparrow} \right] \tag{8.47}$$

where the extra parameter Δ represents the energy gap of the superconductor.

To investigate transport properties of systems with superconducting leads described by Eq.(8.47), we can proceed with the same equation of motion method implemented in SymGF; there is no essential difference between the treatment of normal leads and superconducting leads as far as the mathematical procedure is concerned.

BIBLIOGRAPHY

[1] M. Sato, H. Aikawa, K. Kobayashi, S. Katsumoto, and Y. Iye. Observation of the fano-kondo antiresonance in a quantum wire with a side-coupled quantum dot. *Phys. Rev. Lett.*, 95:066801, Aug 2005.

[2] K. G. Wilson. The renormalization group: Critical phenomena and the kondo problem. *Rev. Mod. Phys.*, 47:773–840, Oct 1975.

[3] F. D. M. Haldane. Scaling theory of the asymmetric anderson model. *Phys. Rev. Lett.*, 40:416–419, Feb 1978.

[4] W. G. van der Wiel, S. de Franceschi, T. Fujisawa, J. M. Elzerman, S. Tarucha, and L. P. Kouwenhoven. *Science*, 289:2105, 2000.

[5] S. Sasaki, H. Tamura, T. Akazaki, and T. Fujisawa. Fano-kondo interplay in a side-coupled double quantum dot. *Phys. Rev. Lett.*, 103:266806, Dec 2009.

[6] Z. Feng, J. Maciejko, J. Wang, and H. Guo. Current fluctuations in the transient regime: An exact formulation for mesoscopic systems. *Phys. Rev. B*, 77:075302, Feb 2008.

[7] Z. Feng, Q.-F. Sun, L. Wan, and H. Guo. Symgf: a symbolic tool for quantum transport analysis and its application to a double quantum dot system. *Journal of Physics: Condensed Matter*, 23(41):415301, 2011.

[8] For details of Mathematica, see www.wolfram.com.

[9] *International Technology Roadmap for Semiconductors 2010 Update*. ITRS, 2010.

[10] L. Gaudreau K. Eber L. C. L. Hollenberg J. P. Kotthaus D. Schröer, A. D. Greentree and S. Ludwig. Electrostatically defined serial triple quantum dot charged with few electrons. *Phys. Rev. B*, 76:075306, 2007.

[11] M. C. Rogge and R. J. Haug. Two-path transport measurements on a triple quantum dot. *Phys. Rev. B*, 77:193306, 2008.

[12] T. Kubo S. Teraoka Y. Tokura S. Tarucha S. Amaha, T. Hatano and D. G. Austing. Stability diagrams of laterally coupled triple vertical quantum dots in triangular arrangement. *Appl. Phys. Lett.*, 94:092103, 2009.

[13] K. Ensslin W. Wegscheider T. Ihn, M. Sigrist and M. Reinwald. Interference in a quantum dot molecule embedded in a ring interferometer. *New J. Phys.*, 9:111, 2007.

[14] W. Izumida S. Teraoka K. Ono K. Kono S. Tarucha G. Aers J. Gupta S. Amaha, T. Hatano and G. Austing. Series-coupled triple quantum dot molecules. *Jpn. J. Appl. Phys.*, 51:02BJ06, 2012.

[15] P. Hawrylak C. Gould P. Zawadzki S. Jullian Y. Feng M. Ciorga, A. S. Sachrajda and Z. Wasilewski. Addition spectrum of a lateral dot from coulomb and spin-blockade spectroscopy. *Phys. Rev. B*, 61:R16315, 2000.

[16] M. Heiblum D. Mahalu D. Sprinzak, Y. Ji and H. Shtrikman. Charge distribution in a kondo-correlated quantum dot. *Phys. Rev. Lett.*, 88:176805, 2002.

[17] J. S. Greidanus L. H. Willems van Beveren S. De Franceschi L. M. K. Vandersypen S. Tarucha J. M. Elzerman, R. Hanson and L. P. Kouwenhoven. Few-electron quantum dot circuit with integrated charge read out. *Phys. Rev. B*, 67:R161308, 2003.

[18] J. Kondo. Resistance minimum in dilute magnetic alloys. *Prog. Theor. Phys.*, 32:37, 1964.

[19] S. Datta. *Electronic Transport in Mesoscopic Systems.* Cambridge, 1997.

[20] L. Arrachea and M. Moskalets. Relation between scattering-matrix and keldysh formalisms for quantum transport driven by time-periodic fields. *Phys. Rev. B*, 74:245322, Dec 2006.

[21] D. S. Fisher and P. A. Lee. Relation between conductivity and transmission matrix. *Phys. Rev. B*, 23:6851–6854, Jun 1981.

[22] L. V. Keldysh. Diagram technique for nonequilibrium processes. *Zh. Eksp. Teor. Fiz.*, 47:1515–1527, 1964.

[23] H. Haug and A. P. Jauho. *Quantum Kinetics in Transport and Optics of Semiconductors*. Springer-Verlag, 1996.

[24] J. Taylor, H. Guo, and J. Wang. *Ab initio* modeling of quantum transport properties of molecular electronic devices. *Phys. Rev. B*, 63:245407, Jun 2001.

[25] J. Taylor, H. Guo, and J. Wang. *Ab initio* modeling of open systems: Charge transfer, electron conduction, and molecular switching of a c_{60} device. *Phys. Rev. B*, 63:121104, Mar 2001.

[26] D. Waldron, P. Haney, B. Larade, A. MacDonald, and H. Guo. Nonlinear spin current and magnetoresistance of molecular tunnel junctions. *Phys. Rev. Lett.*, 96:166804, Apr 2006.

[27] For details of the NanoDcal package, see www.nanoacademic.ca.

[28] T. Hahn. Generating feynman diagrams and amplitudes with feynarts 3. *Computer Physics Communications*, 140(3):418 – 431, 2001.

[29] C. P. Enz. *A Course on Many-Body Theory Applied to Solid-State Physics*. World Scientific, Singapore, 1992.

[30] L. P. Kadanoff and G. Baym. *Quantum Statistical Mechanics*. Benjamin, New York, 1962.

[31] R. F. Wallis and M. Balkanski. *Many-body Aspects of Solid State Spectroscopy*. North Holland, Amsterdam, 1986.

[32] G. D. Mahan. *Many-particle Physics*. Plenum, New York, 1990.

[33] N. Sergueev, Q. Sun, H. Guo, B. G. Wang, and J. Wang. Spin-polarized transport through a quantum dot: anderson model with on-site coulomb repulsion. *Phys. Rev. B*, 65:165303, Apr 2002.

[34] Y. Meir, N. S. Wingreen, and P. A. Lee. Transport through a strongly interacting electron system: Theory of periodic conductance oscillations. *Phys. Rev. Lett.*, 66:3048–3051, Jun 1991.

[35] P. Trocha and J. Barnaś. Quantum interference and coulomb correlation effects in spin-polarized transport through two coupled quantum dots. *Phys. Rev. B*, 76:165432, Oct 2007.

[36] M. Crisan K. Brown and I. Tifrea. Transport and current noise characteristics of a t-shape double-quantum-dot system. *Journal of Physics: Condensed Matter*, 21(21):215604, 2009.

[37] P. Trocha and J. Barnaś. Kondo-dicke resonances in electronic transport through triple quantum dots. *Phys. Rev. B*, 78:075424, Aug 2008.

[38] A.-P. Jauho, N. S. Wingreen, and Y. Meir. Time-dependent transport in interacting and noninteracting resonant-tunneling systems. *Phys. Rev. B*, 50:5528–5544, Aug 1994.

[39] J. Li, W.-D. Schneider, R. Berndt, and B. Delley. Kondo scattering observed at a single magnetic impurity. *Phys. Rev. Lett.*, 80:2893–2896, Mar 1998.

[40] V. Madhavan, W. Chen, T. Jamneala, M. F. Crommie, and N. S. Wingreen. Tunneling into a single magnetic atom: Spectroscopic evidence of the kondo resonance. *Science*, 280:567, 1998.

[41] B. R. Bułka and P. Stefański. Fano and kondo resonance in electronic current through nanodevices. *Phys. Rev. Lett.*, 86:5128–5131, May 2001.

[42] T. Fujisawa, T. H. Oosterkamp, W. G. van der Wiel, B. W. Broer, R. Aguado, S. Tarucha, and L. P. Kouwenhoven. *Science*, 282:932, 1998.

[43] K. Ono and S. Tarucha. Nuclear-spin-induced oscillatory current in spin-blockaded quantum dots. *Phys. Rev. Lett.*, 92:256803, Jun 2004.

[44] A. Hübel, J. Weis, and K. von Klitzing. Precise experimental characterization of a double quantum dot system with strong capacitive interdot coupling. *Physica E: Low-dimensional Systems and Nanostructures*, 40(5):1573 – 1575, 2008.

[45] J. R. Petta, A. C. Johnson, J. M. Taylor, E. A. Laird, A. Yacoby, M. D. Lukin, C. M. Marcus, M. P. Hanson, and A. C. Gossard. Coherent manipulation of coupled electron spins in semiconductor quantum dots.

[46] F. R. Waugh, M. J. Berry, D. J. Mar, R. M. Westervelt, K. L. Campman, and A. C. Gossard. Single-electron charging in double and triple quantum dots with tunable coupling. *Phys. Rev. Lett.*, 75:705–708, Jul 1995.

[47] K. Grove-Rasmussen, H. I. Jørgensen, T. Hayashi, P. E. Lindelof, and T. Fujisawa. A triple quantum dot in a single-wall carbon nanotube. *Nano Lett.*, 8:1055, 2008.

[48] L. Gaudreau, A. Kam, G. Granger, S. A. Studenikin, P. Zawadzki, and A. S. Sachrajda. A tunable few electron triple quantum dot. *Appl. Phys. Lett.*, 95:193101, 2009.

[49] G. Strang. *Introduction to Linear Algebra.* Wellesley-Cambridge Press, Wellesley, MA, 2003.

[50] J. A. Cima, A. L. Matheson, and W. T. Ross. *The Cauchy Transform.* American Mathematical Society, 2006.

[51] T. K. Ng. Nonlinear resonant tunneling through an anderson impurity at low temperature. *Phys. Rev. Lett.*, 70:3635–3638, Jun 1993.

[52] D. C. Ralph and R. A. Buhrman. Kondo-assisted and resonant tunneling via a single charge trap: A realization of the anderson model out of equilibrium. *Phys. Rev. Lett.*, 72:3401–3404, May 1994.

[53] Y. S. Liu, X. F. Yang, X. H. Fan, and Y. J. Xia. Transport properties of a kondo dot with a larger side-coupled noninteracting quantum dot. *Journal of Physics: Condensed Matter*, 20(13):135226, 2008.

[54] P. A. Orellana, F. Domínguez-Adame, I. Gómez, and M. L. Ladrón de Guevara. Transport through a quantum wire with a side quantum-dot array. *Phys. Rev. B*, 67:085321, Feb 2003.

[55] J.-R. Shi and B.-Y. Gu. Quantum waveguide transport with side-branch structures: A recursive algorithm. *Phys. Rev. B*, 55:4703–4709, Feb 1997.

[56] B. H. Wu, J. C. Cao, and K.-H. Ahn. Transport through a strongly correlated quantum dot with fano interference. *Phys. Rev. B*, 72:165313, Oct 2005.

[57] A. M. Chang and J. C. Chen. The kondo effect in coupled-quantum dots. *Reports on Progress in Physics*, 72(9):096501, 2009.

[58] Y. Oreg and D. Goldhaber-Gordon. Two-channel kondo effect in a modified single electron transistor. *Phys. Rev. Lett.*, 90:136602, Apr 2003.

[59] M. Pustilnik, L. Borda, L. I. Glazman, and J. von Delft. Quantum phase transition in a two-channel-kondo quantum dot device. *Phys. Rev. B*, 69:115316, Mar 2004.

[60] L. G. G. V. Dias da Silva, N. P. Sandler, K. Ingersent, and S. E. Ulloa. Zero-field kondo splitting and quantum-critical transition in double quantum dots. *Phys. Rev. Lett.*, 97:096603, Aug 2006.

[61] R. Žitko. Fano-kondo effect in side-coupled double quantum dots at finite temperatures and the importance of two-stage kondo screening. *Phys. Rev. B*, 81:115316, Mar 2010.

[62] C.-H. Chung and T.-H. Lee. Tunable fano-kondo resonance in side-coupled double quantum dot systems. *Phys. Rev. B*, 82:085325, Aug 2010.

[63] B.H. Wu and K.-H. Ahn. Transport through a t-shaped double quantum dot with fano-kondo interaction. *Physica E: Low-dimensional Systems and Nanostructures*, 34(1-2):464 – 467, 2006.

[64] Y. Tanaka and N. Kawakami. Interference effects on kondo-assisted transport through double quantum dots. *Phys. Rev. B*, 72:085304, Aug 2005.

[65] F.-B. Yang, S.-Q. Wu, and W.-L. Sun. Spin-polarized transport through the t-shaped double quantum dots with fano-kondo interaction. *Chinese Physics Letters*, 24(7):2056, 2007.

[66] A.D. Güclü, Q.-F. Sun, and H. Guo. Kondo resonance in a quantum dot molecule. *Phys. Rev. B*, 68:245323, Dec 2003.

[67] H. Tamura and S. Sasaki. Fano-kondo effect in side-couple double quantum dot. *Physica E: Low-dimensional Systems and Nanostructures*, 42(4):864 – 867, 2010.

[68] R. Bulla, T. A. Costi, and T. Pruschke. Numerical renormalization group method for quantum impurity systems. *Rev. Mod. Phys.*, 80:395–450, Apr 2008.

[69] T. K. Ng and P. A. Lee. On-site coulomb repulsion and resonant tunneling. *Phys. Rev. Lett.*, 61:1768–1771, Oct 1988.

[70] Y. Meir, N. S. Wingreen, and P. A. Lee. Low-temperature transport through a quantum dot: The anderson model out of equilibrium. *Phys. Rev. Lett.*, 70:2601–2604, Apr 1993.

[71] N. S. Wingreen and Y. Meir. Anderson model out of equilibrium: Noncrossing-approximation approach to transport through a quantum dot. *Phys. Rev. B*, 49:11040–11052, Apr 1994.

[72] L. P. Kouwenhoven and L. Glazman. *Physics World*, Janurary:33–38, 2001.

[73] U. Fano. Effects of configuration interaction on intensities and phase shifts. *Phys. Rev.*, 124:1866–1878, Dec 1961.

[74] A. Schiller and S. Hershfield. Theory of scanning tunneling spectroscopy of a magnetic adatom on a metallic surface. *Phys. Rev. B*, 61:9036–9046, Apr 2000.

[75] O. Újsághy, J. Kroha, L. Szunyogh, and A. Zawadowski. Theory of the fano resonance in the stm tunneling density of states due to a single kondo impurity. *Phys. Rev. Lett.*, 85:2557–2560, Sep 2000.

[76] J. Göres, D. Goldhaber-Gordon, S. Heemeyer, M. A. Kastner, H. Shtrikman, D. Mahalu, and U. Meirav. Fano resonances in electronic transport through a single-electron transistor. *Phys. Rev. B*, 62:2188–2194, Jul 2000.

[77] M. Plihal and J. W. Gadzuk. Nonequilibrium theory of scanning tunneling spectroscopy via adsorbate resonances: Nonmagnetic and kondo impurities. *Phys. Rev. B*, 63:085404, Feb 2001.

[78] R. Taranko, T. Kwapiński, and E. Taranko. Influence of microwave fields on electron transport through a quantum dot in the presence of direct tunneling between leads. *Phys. Rev. B*, 69:165306, Apr 2004.

[79] J. Jaylor. *Ab-initio modelling of transport in atomic scale devices.* PhD thesis, McGill University, Department of Physics, 2000.

[80] D. Waldron. *Ab-initio simulation of spintronic devices.* PhD thesis, McGill University, Department of Physics, 2007.

[81] G. Kresse and J. Hafner. *Ab initio* molecular dynamics for liquid metals. *Phys. Rev. B*, 47:558–561, Jan 1993.

[82] G. Kresse and J. Hafner. *Ab initio* molecular-dynamics simulation of the liquid-metal amorphous-semiconductor transition in germanium. *Phys. Rev. B*, 49:14251–14269, May 1994.

[83] G. Kresse and J. Furthmüller. Efficiency of ab-initio total energy calculations for metals and semiconductors using a plane-wave basis set. *Comput. Mat. Sci.*, 6:15, 1996.

[84] G. Kresse and J. Furthmüller. Efficient iterative schemes for *ab initio* total-energy calculations using a plane-wave basis set. *Phys. Rev. B*, 54:11169–11186, Oct 1996.

[85] P. Ordejón, E. Artacho, and J. M. Soler. Self-consistent order-n density-functional calculations for very large systems. *Phys. Rev. B*, 53:R10441–R10444, Apr 1996.

[86] J. M. Soler, E. Artacho, J. D. Gale, A. García, J. Junquera, P. Ordejón, and D. Sánchez-Portal. The siesta method for ab initio order-n materials simulation. *Journal of Physics: Condensed Matter*, 14(11):2745, 2002.

[87] G. Stefanucci. Bound states in *ab initio* approaches to quantum transport: A time-dependent formulation. *Phys. Rev. B*, 75:195115, May 2007.

[88] H. Wang R. Wang H. Pan, Y. Cui. Spin-polarized andreev reflection and spin accumulation in a quantum-dot aharonov-bohm interferometer with spin-orbit interaction effects. *Journal of Applied Physics*, 110:033706, 2011.

[89] H. Pan and R. Lü. Effects of the spin-orbit interaction on the spin polarization of quantum dots in the presence of andreev reflection. *Journal of Physics Condensed Matter*, 20:195220, 2008.

[90] Y. Wei L. Wan and J. Wang. Shot noise in a superconducting hybrid molecular device. *Nanotechnology*, 17:489, 2006.

[91] A. Pfund G. Fagas, G. Tkachov and K. Richter. Geometrical enhancement of the proximity effect in quantum wires with extended superconducting tunnel contacts. *Phys. Rev. B*, 71:224510, 2005.

[92] Yadong Wei, Jian Wang, Hong Guo, Hatem Mehrez, and Christopher Roland. Resonant andreev reflections in superconductor˘carbon-nanotube devices. *Phys. Rev. B*, 63:195412, Apr 2001.

[93] C. M. Marcus A. F. Morpurgo, J. Kong and H. Dai. Gate-controlled superconducting proximity effect in carbon nanotubes. *Science*, 286:263, 1999.

[94] Q. Sun, J. Wang, and T. Lin. Resonant andreev reflection in a normal-metal-quantum-dot-superconductor system. *Phys. Rev. B*, 59:3831–3840, Feb 1999.

[95] J. C. Cuevas, A. Martin-Rodero, and A. L. Yeyati. Hamiltonian approach to the transport properties of superconducting quantum point contacts. *Phys. Rev. B*, 54:7366–7379, Sep 1996.

[96] S. Ishizaka, J. Sone, and T. Ando. dc josephson current through a quantum dot coupled with superconducting leads. *Phys. Rev. B*, 52:8358–8362, Sep 1995.